Self-assembly of Carbohydrate Esters

Dissertation
to attain the degree Doctor of Philosophy (Ph. D.)
of the Faculty of Forest Sciences and Forest Ecology/Agricultural Sciences
Georg-August-Universität Göttingen

Submitted by

Yawen Yao
Born on the 29th March in 1991

Göttingen, November 2021

1st Referee: Prof. Dr. Kai Zhang

2nd Referee: Prof. Dr. Carsten Mai

Additional Referee: Prof. Dr. Marcus Müller

Date of the oral examination: 28. 09. 2021

Acknowledgement

This dissertation is the output of not only my own effort during these 4 years but also the tremendous supports I obtained from all the professors, scientific workers, families and friends that I met. First and foremost, I would like to delicate my deepest gratitude to my supervisor Prof. Kai Zhang. Thanks for giving me the opportunity to pursue my Ph.D. study in Germany, which is a precious experience in my life. During my 4 years study, what I have gained is beyond my expectation. My knowledge has been extended, experiences have been accumulated and most importantly, I've learnt how to be a person with integrity, motivation and ambition. After my Ph.D. study, I'm 100% confident about my future work and life, due to the skills I handled. Besides, his guidance helped me in all the time of scientific research and writing of papers. I could not have imagined having a better advisor and mentor for my Ph.D. study.

Besides my advisor, I would like to thank the rest of my thesis committee, Prof. Carsten Mai and Prof. Holger Militz, not only for their insightful comments and encouragement, but also for the hard questions which incented me to widen my research from various perspectives. My sincere thanks also go to Prof. Marcus Müller for being my examiner during my oral defense. Moreover, I would like to thank Prof. Matthias Karg, Prof. Dr. Qiyun Tang and Dr. Sabine Rosenfeldt who coordinated with me during my study for measuring diverse tests for me. They also provided me many ideas and knowledge from different perspectives. Without their precious support it would not be possible for me to conduct the research and finish my dissertation.

I also want to thank the China Scholarship Council (CSC) for the financial support, which allows me to swim in the ocean of knowledge without worrying about the reality. Besides, I also want to delicate my great thanks to my fellow labmates for the stimulating discussions, for the sleepless nights we were working together before deadlines and for all the jokes and fun we have had in the last four years. Especially, my gratitude to my officemates in Büsgenweg 3, Bo Pang, Hua Zhang and Kui Zeng for the delicious food they gave, crazy laughter I got and boast we made.

I would also like to express my sincere gratitude to the members of the project I'm doing in Maastricht University: Prof. Katrien Bernaerts, Dr. Peter Quaedflieg, Dr. Dannie van Osch and

Monika Jedrzejczyk. Thanks for your warm welcome, kind help and allowing me to arrange my time freely in finishing my Ph.D. dissertation and project study.

Last but not the least, I would like to thank my friends not only in China, also in Germany for supporting me spiritually throughout writing this thesis and my life in general. Especially, I would like to thank Lianghao Dao, Yu Qiu, Chou Wu, Qianqian Qin, Boyang Liu for giving me a good time in Göttingen (considering how we met). Also, my gratitude to Bert Pickert, Yuan Hou and Anna-Lián LI for making me feel like a member of your family. Besides, my two roommates Huiyuan Pang and Xiaowei Jin for the happy moment and wonderful cooking. I cannot list all the people, so here I want to express my deepest thanks to all the people I met. Thank you for fulfilling my life.

Abstract

Superstructures fabricated from carbohydrates and their derivatives hold an immense promise for the application in diverse fields. However, still many understudied problems challenge us, such as the roles of backbones and side chains during the formation of superstructures, precise control of their morphologies and the application of these unique structures.

In this thesis, I first fabricated hydrophobic and superhydrophobic surfaces on wood by using cellulose stearoyl ester (CSE) and glycerol stearoyl ester (GSE). CSE was used for dip-coating (1st layer) the wood, leading to a hydrophobic surface and GSE was used for brush-coating (2nd layer) the wood, leading to a hierarchical superhydrophobic surface. Both hydrophobic and superhydrophobic woods exhibit better anti-fungal properties comparing with non-treated wood. Furthermore, superhydrophobic wood could thoroughly prevent fungal attachment to treated wood, while fungi could still be found inside hydrophobic wood after anti-fungal test. This study shows that both CSE and GSE can form hydrophobicity due to the full substitution of the hydroxyl groups by fatty side chains with 18 carbons. However, the backbone of cellulose and the monomer structure of glycerol result in the formation of membrane by CSE and hierarchical porous structure by GSE, respectively.

The most commonly introduced microparticles from carbohydrates all hold conventional filled morphology. Nevertheless, microparticles with chiral and porous morphology are rarely mentioned from carbohydrates. Moreover, the formation of tunable chiral and porous flower-like microparticles using the same materials, especially monosaccharides without applying external stimuli, is still highly understudied. In this study, the formation of chiral, solid, and flower-like microparticles by only using monosaccharide stearoyl esters (MSSEs) were reported for the first time. Chiral, hierarchical superstructures can be obtained from D/L-glucose stearoyl esters (D/L-GlcSE). Chiral 'left-handed' (counterclockwise) spiralling morphology can be obtained by D-GlcSE, while 'right-handed' (clockwise) morphology can be induced by L-GlcSE. The formation of microparticles with chirality can only be achieved when the α/β ratio of anomer in D/L-GlcSE is 20/80, the concentration is 1 mg/mL from 60°C to 25°C with the aging time of 20 min. The α configuration leads to irregular aggregates, which show worse thermal and crystallization properties, while mature round smooth microparticles with better thermal and crystallization

properties are beneficial from β configuration. Axially stretched α configuration improves the difficulties of stacking of MSSE molecules during self-assembly, while better stacking is beneficial from equatorially stretched β configuration. These results can be explained by the displacement during molecular stacking via self-assembly and chirality amplification in the hierarchical superstructures.

In addition to the effects of configurations as D/L-configuration and α/β-anomers, the effect of the monosaccharides that contain more structural difference was further studied by using four different D-monosaccharide stearoyl esters (D-MSSEs), which are D-glucose stearoyl esters (D-GlcSE), D-xylose stearoyl esters (D-XylSE), D-galactose stearoyl esters (D-GalSE) and D-mannose stearoyl ester (D-ManSE). Based on the ^{1}H NMR spectra, the α/β ratios at C1 for D-GlcSE, D-XylSE, D-GalSE and D-ManSE are 20/80, 15/85, 27/73 and 35/65, respectively. Besides, they also have diverse number of side chains and the bonds stretching axially/equatorially at C2, C4 and C6. By adjusting the number of side chains and the bonds stretching axially/equatorially, diverse microparticles with solid and porous flower-like morphologies can be adapted. More sidechains lead to lower precipitation temperature, worse thermal and crystallization properties. With the same side chains, axially instead of equatorially stretched bond configuration results in lower precipitation temperature, worse thermal and crystallization properties. This conclusion can be explained by the increased obstacles during the stacking of molecules from more side chains and more bonds stretched axially. Thus, both the number of side chains and the number of bonds stretching axially/equatorially play the pivotal rules when tuning the sugar-based superstructures from solid to chiral and porous morphology.

This thesis is a cumulative work including 3 publications. One of them was already published and two are under submission. The background, the objective of the study, results and discussion of these three publications and the conclusion are presented in Sections 1-4.

Zusammenfassung

Aus Kohlenhydraten und ihren Derivaten hergestellte Superstrukturen sind für die Anwendung in verschiedenen Bereichen immens vielversprechend. Es stellen uns jedoch immer noch viele Probleme in Frage, wie die Rolle der Grundgerüsten und Seitenketten bei der Bildung der Superstrukturen, die genaue Kontrolle ihrer Morphologien und die Anwendung dieser einzigartigen Strukturen.

In dieser Arbeit haben wir zunächst hydrophobe und superhydrophobe Oberflächen auf Holz durch Cellulosestearoylester (CSE) und Glycerinstearoylester (GSE) hergestellt. CSE wurde zum Tauchbeschichten (1. Schicht) des Holzes verwendet, die zu einer hydrophoben Oberfläche führte; GSE wurde zum Bürstenbeschichten (2. Schicht) des Holzes verwendet, die zu einer hierarchischen superhydrophoben Oberfläche führte. Sowohl hydrophobe als auch superhydrophobe Hölzer zeigten sich im Vergleich zu unbehandeltem Holz bessere antimykotische Eigenschaften. Darüber hinaus könnte superhydrophobes Holz die Anhaftung von Pilzen an behandeltes Holz gründlich verhindern, während Pilze nach einem Antimykotiktest noch in hydrophobem Holz gefunden werden könnten. Diese Forschung zeigt sich, dass sowohl CSE als auch GSE aufgrund des vollständigen Ersatzes der Hydroxylgruppen durch C18-Seitenketten Hydrophobizität bilden können. Das vielfältige Rückgrat von Cellulose und Glycerin führt jedoch zur Bildung einer Membran und einer hierarchischen Struktur durch CSE bzw. GSE.

Die am häufigsten eingeführten Mikropartikel aus Kohlenhydraten weisen alle eine konventionelle gefüllte Morphologie auf. Trotzdem werden Mikropartikel mit chiraler und poröser Morphologie aus Kohlenhydraten selten erwähnt. Darüber hinaus ist die Bildung von abstimmbaren chiralen und porösen blütenartigen Mikropartikeln unter Verwendung der gleichen Materialien, insbesondere Monosaccharide ohne Anwendung äußerer Reize, noch stark unterbesprochen. In dieser Forschung berichteten wir erstmals über die Bildung chiraler, fester und blütenartiger Mikropartikel nur unter Verwendung von Monosaccharid-Stearoylestern (MSSEs). Es zeigt sich, dass chirale, hierarchische Überstrukturen mit Händigkeit aus D/L-Glucosestearoylestern (D/L-GlcSE) erhalten werden können. Die chirale Spiralmorphologie für Linkshänder (gegen den Uhrzeigersinn) kann durch D-GlcSE erhalten werden, während die

Morphologie für Rechtshänder (im Uhrzeigersinn) durch L-GlcSE induziert werden kann. Die Bildung von Mikropartikeln mit Chiralität kann nur erreicht werden, wenn das α/β-Verhältnis bei C1 in D/L-GlcSE 20/80 beträgt, die Konzentration 1 mg/ml von 60 °C bis 25 °C mit einer Alterungszeit von 20 Minuten beträgt. Die α-Konfiguration führt zu unregelmäßigen Aggregaten, die sich schlechtere Wärme- und Kristallisationseigenschaften zeigen, während reife runde glatte Mikropartikel mit besseren Wärme- und Kristallisationseigenschaften von der β-Konfiguration profitieren. Die axial gestreckte α-Konfiguration verbessert die Schwierigkeiten beim Stapeln von MSSE-Molekülen während der Selbstorganisation, während ein besseres Stapeln von der äquatorial gestreckten β-Konfiguration profitiert. Diese Ergebnisse können durch die Verschiebung während des molekularen Stapelns durch Selbstorganisation und Chiralitätsverstärkung in den hierarchischen Überstrukturen erklärt werden.

Zusätzlich zu den Wirkungen von Konfigurationen als D/L-Konfiguration und α/β-Anomeren wurde die Wirkung der Monosaccharide, die mehr strukturelle Unterschiede enthalten, unter Verwendung von 4 D-Monosaccharid-Stearoylestern (D-MSSEs), die D sind, weiter untersucht - Glucose-Stearoylester (D-GlcSE), D-Xylose-Stearoylester (D-XylSE), D-Galactose-Stearoylester (D-GalSE) und D-Mannose-Stearoylester (D-ManSE). Basierend auf den 1H-NMR-Spektren betragen die α/β-Verhältnisse bei C1 für D-GlcSE, D-XylSE, D-GalSE und D-ManSE 20/80, 15/85, 27/73 bzw. 35/65. Außerdem haben sie auch eine unterschiedliche Anzahl von Seitenketten und die Bindungen erstrecken sich axial/äquatorial an C2, C4 und C6. Durch Einstellung der Anzahl der Seitenketten und der axial/äquatorial dehnenden Bindungen können verschiedene Mikropartikel mit festen und porösen blütenartigen Morphologien angepasst werden. Mehr Seitenketten führen zu einer niedrigeren Fällungstemperatur, schlechteren Wärme- und Kristallisationseigenschaften. Bei gleichen Seitenketten führt eine axial statt äquatorial gestreckte Bindungskonfiguration zu einer niedrigeren Fällungstemperatur, schlechteren thermischen und Kristallisationseigenschaften. Diese Schlussfolgerung kann durch die erhöhten Hindernisse beim Stapeln von Molekülen aus mehr Seitenketten und mehr axial gestreckten Bindungen erklärt werden. Somit spielen sowohl die Anzahl der Seitenketten als auch die Anzahl der Bindungen, die sich axial/äquatorial dehnen, die entscheidenden Regeln, wenn die auf Zucker basierenden Superstrukturen von fester zu chiraler und poröser Morphologie eingestellt werden.

Diese Arbeit ist eine kumulative Arbeit mit 3 Publikationen. Einer von ihnen ist bereits veröffentlicht und zwei werden eingereicht. Der Hintergrund, das Ziel der Forschung, die Ergebnisse und die Diskussion der drei Publikationen sowie die Schlussfolgerung sind in den Abschnitten 1 bis 4 dargestellt.

Table of Contents

List of Publications

Publication 1

Differential anti-fungal effects from hydrophobic and superhydrophobic wood based on cellulose and glycerol stearoyl esters

Yawen Yao, Antje Gellerich, Michaela Zauner, Xiaoxu Wang, Kai Zhang*

Cellulose **2018**, 25, 1329-1338.

Publication 2

Chiral hierarchical structure in glucose stearoyl esters and the role of bond configuration

Yawen Yao, Qiyun Tang, Sabine Rosenfeldt, Marcel Krüsmann, Matthias Karg, Kai Zhang*

Submitted

Publication 3

Single bond bending on monosaccharide rings enables flower-like particles via liquid-liquid phase separation

Yawen Yao, Qiyun Tang, Sabine Rosenfeldt, Kai Zhang*

Submitted

Abbreviations

DS	Degree of substitution
N	Number of carbons
T_g	Glass transition temperature
E’	Storage bending modulus
tan δ	Damping
T_m	Melting temperature
LiCl	Lithium chloride
DMAc	Dimethylacetamide
CDPi	Curdlan pivalate
DP	Degree of polymerization
PET	Polyethylene terephthalate
PBS	Poly (butylene succinate)
PLA	Poly (lactic acid)
CMC	Critical micelle concentration
CA	Cellulose acetate
CAB	Cellulose acetate butyrate
CAP	Cellulose acetate propionate
C-A-P	Cellulose acetate phthalate
C-A-T	Cellulose acetate trimellitate
C-A-S	Cellulose acetate succinate
$scCO_2$	Supercritical carbon dioxide
SEM	Scanning electron microscope
CSE	Cellulose stearoyl esters
Fe_3O_4-NPs	Iron (II,III) oxide nanoparticles
RhB	rhodamine B
C18-RhB	stearoylaminoethyl rhodamine B

1. Introduction

1.1 Carbohydrate esters

The typical structure of esters can be concluded as a general formula RCOOR', where R and R' are organic groups or moieties. Carbohydrate esters are the compounds where R or/and R' have carbohydrate structures and can be categorized into monoesters, diesters and polyesters, according to the number of ester bonds.

Carbohydrate can also be named as saccharide and their molecular formula can be generally concluded as $C_m (H_2O)_n$ (where m may be different from n). The carbohydrate is consisting of four groups: monosaccharides, disaccharides, oligosaccharides and polysaccharides. Among all, monosaccharides and disaccharides can also be named as sugar. Monosaccharides, which are also called simple sugars, are the most basic units of forming carbohydrates. Their structures can be described in three ways: Fischer projection, Haworth projection and chair conformation.[1] To set glucose as an example as shown in **Figure 1a**, even though we can clearly see the arrangement of the structures in Fischer projection, it was found that monosaccharide structures are mainly shown in circle format. The cyclization of glucose starts from the nucleophilic substitution of position C5 to position C1 and then hemiacetal formed. Due to the unique structure of glucose, the nucleophilic substitution can happen from two directions and thus lead to two new structures, which are called α and β configuration as shown in Haworth projection and chair conformation. Disaccharides are the saccharides consisting of two monosaccharides. According to the connecting position, disaccharides can be divided into non-reducing disaccharides and reducing disaccharides as shown in **Figure 1b**. Oligosaccharides and polysaccharides are the saccharides with more than two repeating sugar units in the molecules. Some examples of oligosaccharides and polysaccharides are listed in **Figure 1c** and **1d**.

Carbohydrate esters are biodegradable, biocompatible and environmentally friendly materials, which have a huge potential use to replace fossil fuel derived materials.[2-5] Research showed that carbohydrate esters can be used in food industry such as surfactant[6-9] and softening agent[10,11]. Recently, more research showed that carbohydrate esters also exhibit antitumor activity[12-16],

plant growth inhibition[17-19] and antibiotic activities[20-23]. Thus, they can be used as antibacterial and antifungal agents in clinic fields. Furthermore, carbohydrate esters also have a variety of applications in the fields of enhanced oil recovery[24] and environmental detoxification processes[25].

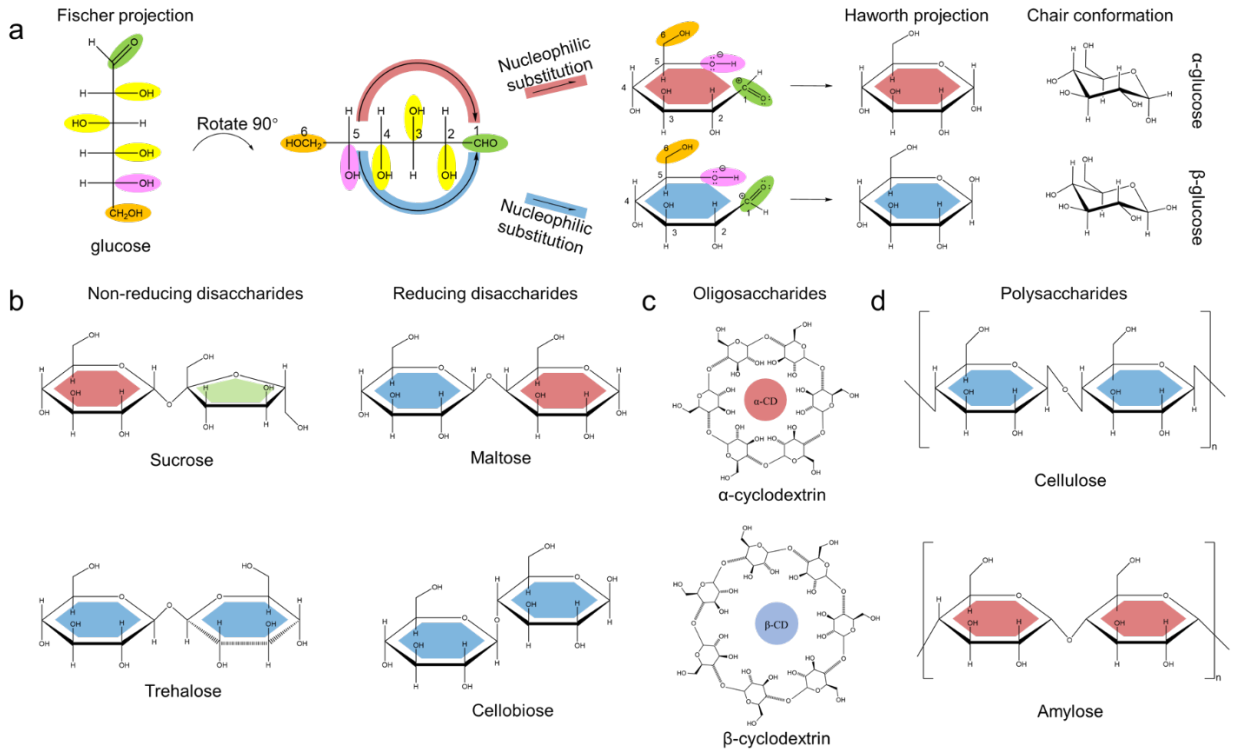

Figure 1. a) The cyclization of glucose introduced by Fischer projection, Haworth projection and chair conformation and examples of b) disaccharides, c) oligosaccharides and d) polysaccharides.

1.2 Synthesis of carbohydrate esters

The synthesis of carbohydrate esters can be divided in two methods: chemical[26-28] and enzymatic method[29-31]. Chemical method for the synthesis of carbohydrate esters is efficient and easy regardless the used substrate carbohydrates. Normally acid or alkaline are involved at elevated temperature and also chemical solvents are combined in this process. When applying this method to scale-up production, it still maintains its advantages. The shortcomings of this method include no regioselectivity and usage of toxic solvents. The chemical acylation with acid chlorides has

been successfully and widely applied in chemical industry. Among all the chemical methods, acyl chloride-pyridine system has been proved to be efficient and fast. For example, Adkins and Thompson reported the synthesis of solid additives by benzoyl chloride, furoyl chloride, propionyl chloride and other acyl chlorides with pyridine.[32] They found that acyl chlorides with pyridine are powerful acylating agents at low temperatures and the procedure has excellent yields. Pyridine not only works as medium, also as catalyst. Wang and Tao reported the synthesis of cellulose esters with soybean fatty acids.[33,34] They modified soybean fatty acid into soybean fatty acid chloride and then synthesized the ester in pyridine. Garcia et al. synthesized cellulose fatty esters with diverse degree of substitution (DS) via acid chloride/pyridine method.[35] They found that the thermomechanical properties of the esters depend on the length of the side chain and DS. Otey and Mehltretter reported the synthesis of 3-stearoyl-D-glucose as a bread-softening agent.[36] The hydroxyl group at C3 in glucose was modified by the esterification reaction of stearoyl chloride with 1,2,5,6-diisopropylidene-D-glucose in chloroform and pyridine.

In order to avoid the shortcomings from chemical method, a more environmentally friendly biosynthesis method was introduced. Enzyme-catalyzed method usually happens in organic solvents via esterification or transesterification and sometimes is combined with the assistant of microwave[37-39], supercritical carbon dioxide[20,40-42] and/or ionic liquids[43-48], et al. Biosynthesis method is under mild reaction conditions with high selectivity and low toxicity. During the reaction, the regioselectivity starts at primary hydroxyl groups and then secondary hydroxyl groups.[49-51] Even though it has so many advantages comparing to chemical method, biosynthesis method normally has to employ vinyl ester (with organic solvent) during its reaction, which is not real green. Besides, the biosynthesis has a significant degree of substrate specificity and the yields or conversion vary among substrates and chain length. This is due to the enzymatic activity varies according to the carbohydrate substrates. Furthermore, the hydroxyl groups in the sugar ring exhibit diverse activities during enzymatic synthesis. For example, both papers from Patil et al.[52] and Riva et al.[53] reported the regioselectivity of hydroxyl groups in the sugar ring. It was found that the tendency of the reactivities are: 1'-OH = 6-OH > secondary-OH >> 6'-OH. Synthesis of carbohydrate esters via enzymes has been well introduced during the past decades. To set glucose as an example, Chang and Shaw published the earliest paper introducing the synthesis of regioselective glucose penta-acetate by lipase catalyzed production.[54] They found

that esterase-catalyzed deacetylations afforded significant accumulation of intermediate glucose esters at different degree of substrate conversion. Then, more publications and reviews introduced a wide variety of enzyme sources with high catalytic efficiency properties to obtain glucose ester such as Porcine pancreatic lipase II, Subtilisin, Lipozyme TM 20 (Mucor miehei), Optimase M-440 (Bacillus licheniformis), Alkaline protease (Streptomyces sp.), Novozym SP435 (Candida antarctica), Lipozyme IM20 (Rhizomucor miehei, RML) and Rhizopus oryzae lipase.[20,22,55-58] In comparison to tradition way of chemical methods, biosynthesis by enzymes is greener and excellent at regioselective properties even though this method cost more. **Figure 2** exhibit an example of the synthesis of regioselective carbohydrate esters by lipase.

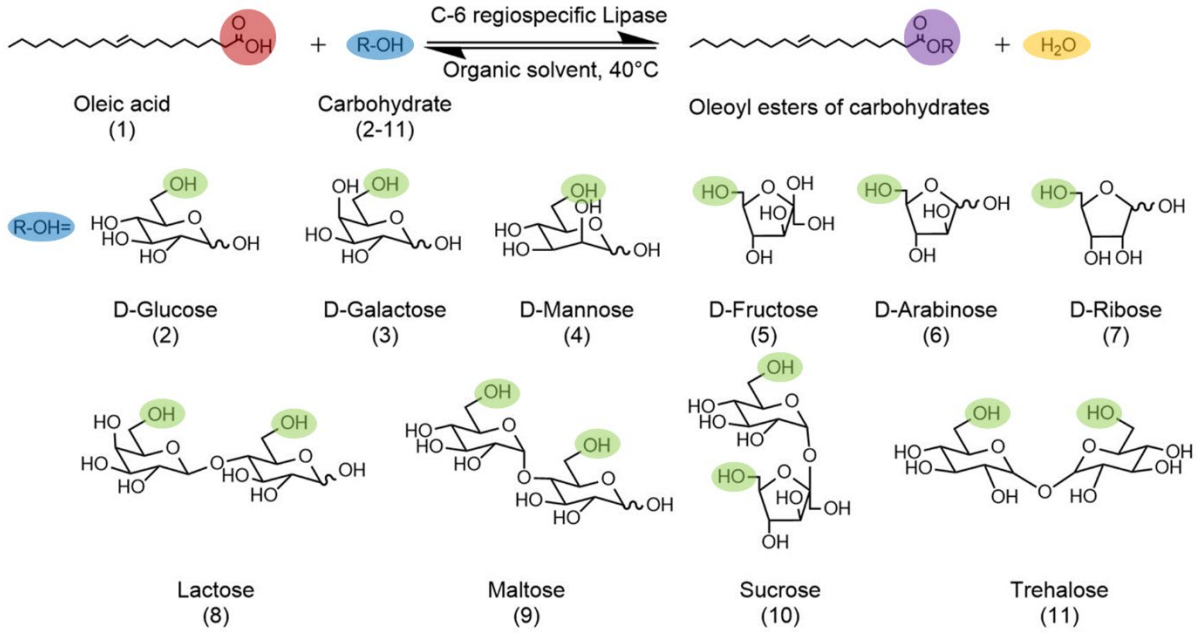

Figure 2. Schematics of the process for converting oleic acid and carbohydrates to oleoyl carbohydrate esters by using C-6 regiospecific lipase as biocatalyst. (Reproduced from CHANG et al. [54] Copyright from ELSEVIER 2009)

1.3 Role of side chain during crystallization and application of carbohydrate esters

In carbohydrates, many compounds such as cellulose and amylose have a clear linear backbone with hydroxyl groups attached to the side and then side chains can be grafted onto the backbone of carbohydrates via esterification. The obtained carbohydrate esters have a unique crystallization property and thus have a wide variety of applications, such as plasticizer[59-64]. During crystallization, the two mostly essential factors are side chain length and degree of substitutions (DS). The side chain length is decided by the number of carbons (N), while the DS is dependent on the number of substituted hydroxyl groups.

To set cellulose as an example, quite a lot of publications have introduced how N and DS affect the crystallization of cellulose alkyl esters. Vaca-Garcia et al. compared the glass transition temperature (T_g), storage bending modulus (E') and damping (tan δ) from films of cellulose alkyl esters with diverse DS and N.[35] It was found that for fully substituted cellulose alkyl esters, N has no influence on T_g and E', while tan δ decreases with the increasing of N. For partially substituted cellulose alkyl esters, they have more E' and tan δ than fully substituted cellulose alkyl esters. Furthermore, N has no influence on tan δ, while with the increasing of N, T_g and E' decreases. It was inferred that increasing of N can reduce the cohesion between backbones and thus it takes less energy to move the molecular chains. Besides, hydroxy groups in partially substituted cellulose esters should be responsible for the increasing of E' and tan δ. Crépy et al. reported the cellulose alkyl esters with N of 8-18 in side chains.[65] It was found that increasing of N can lead to the increasing of the melting temperature (T_m). Moreover, two T_g were found in DSC. The higher one represents the T_g from backbones, where the lower one is from side chains. When the N is over 11, side chains can crystallize into hexagonal lattice. The structures are shown in layered types, where backbones are arranged in a plane and the flexible side chains being fully extended and perpendicular to the backbone. They also reported a series of cellulose alkyl esters with various DS between 1.7 and 3 in a homogeneous LiCl/DMAc medium.[66] It was found that as long as the DS is lower enough, the crystallization properties of cellulose esters are improved. However, the mechanical behavior mainly depends on N instead of DS.

Instead of direct grafting of side chains to the hydroxyl groups in cellulose, side chains can also be grafted to the modified hydroxy groups. Chen synthesized cellulose alkyl esters and

hydroxypropyl cellulose alkyl esters with N ranging from 8 to 20.[67] The hydroxypropyl cellulose esters showed higher enthalpy and crystallinity than cellulose esters of the same side chain length. This can be explained by the adding hydroxypropyl parts, which results in more $-CH_2-$ groups arrange into the crystal lattice. Furthermore, the side chains are perpendicular to the backbone in cellulose ester, while they tilt to backbone in the hydroxypropyl cellulose esters due to the steric hindrance and thus facilitate the overall crystalline packing.

Beside the mentioned linear alkyl side chains, the branched alkyl side chains also exhibit unique characteristics. Danjo and Iwata studied and compared a series of cellulose alkyl esters with linear and branched side chains including cellulose isobutyrate, cellulose butyrate and cellulose propionate.[68] Cellulose isobutyrate with branch side chains of 4 carbons exhibited especially the highest T_m in comparison of those cellulose esters with only linear side chains such as cellulose butyrate (4 carbons) and cellulose propionate (3 carbons). With the increasing of N, T_m and T_g decreases. After fabricating the cellulose esters into films by solvent-casting, cellulose esters with branched side chains exhibited higher Young's moduli and Yield stress, lower tensile strength and elongation at break due to the helix molecular chain conformation packed by the terminally branched structures.

Even though the above-mentioned cellulose esters with some certain side chain length and DS showed some advantages, the application of cellulose esters in the reality is still constrained by the conditions of high price and the use of large quantity of chemicals. In order to maintain the quality of cellulose esters and reduce the chemical consumption, Willberg-Keyrilaeinen et al. synthesized cellulose alkyl esters with N between 6 and 18 in a homogeneous system using ozone molar mass-controlled cellulose.[69] They prepared the films via solvent casting by using cellulose esters with the DS as low as possible and found that under similar conditions, the DS decreases with the increasing of N. Furthermore, the side chains can crystallize only when N is over 10. The obtained cellulose esters have the lowest DS between 0.8-1.3 and the formed films exhibit comparable mechanical properties to other generally used plastics.

Cellulose esters can not only self-crystallize, they can also be applied to other polymers for blending. Nishio reported the miscibility of blends of polycaprolactone with a series of cellulose alkyl esters whose N in side chains are ranging from 2 to 7.[70] Results showed that when N is 4

and DS is 2, the blends exhibit the best miscibility. However, when DS is lower than 2, all cellulose esters are immiscible. Cellulose esters with N of 3 can only show miscibility when the DS is extremely high.

Beside the widely studied cellulose esters, some other carbohydrate esters with diverse side chains and DS have also been reported. Samuel et al. synthesized two dextran alkyl esters whose side chains have 14 and 16 carbons, separately.[71] They used Raman spectroscopy and MCRALS statistical analysis to analyze the crystallinity of the obtained dextran esters. It was found that dextran alkyl esters with 14 carbons in side chains showed considerably less crystallinity in comparison of the esters with 16 carbons, which have only 2 more carbons in side chains.

Vanmarcke et al. synthesized three types of fully substituted starch alkyl esters with different N (8, 12 and 16) and amylose/amylopectin ratio.[72] It was found that structural, thermal and mechanical properties are depending on both N and the composition ratio. When the N are 8 and 12, the prepared esters are totally amorphous, while the side chains can crystallize into hexagonal-like crystal structures when N is 16 regardless of the composition ratio. A more ductile behavior can be observed when the esters have more amylose content and less N (8 and 12).

Zhai et al. reported the synthesis of curdlan esters with linear and branched side chains by using high-molecular-weight linear β-1,3-glucan and diverse carboxylic acids (isobutyric, isovaleric, isohexanoic, and isoheptanoic acids) as shown in **Figure 3**.[73] In comparison of curdlan and its esters, the grafting side chains can improve the thermal stabilities of curdlan. With the increasing of N, T_m and T_g decrease regardless of linear or branched side chains. However, to compare linear and branched side chains, curdlan esters with branched side chains result in more regular and rigid structures than those with linear ones. Among all, CDPi is the most stable products. After the fabrication of films from curdlan esters with diverse side chains, it was found that with the increasing of N, the films became rubberier and softer. Furthermore, the films from the esters with branched side chains were more robust than those with linear ones. Besides, the tensile strength and Young's modulus decreased and elongation at break increased when the N was increasing.

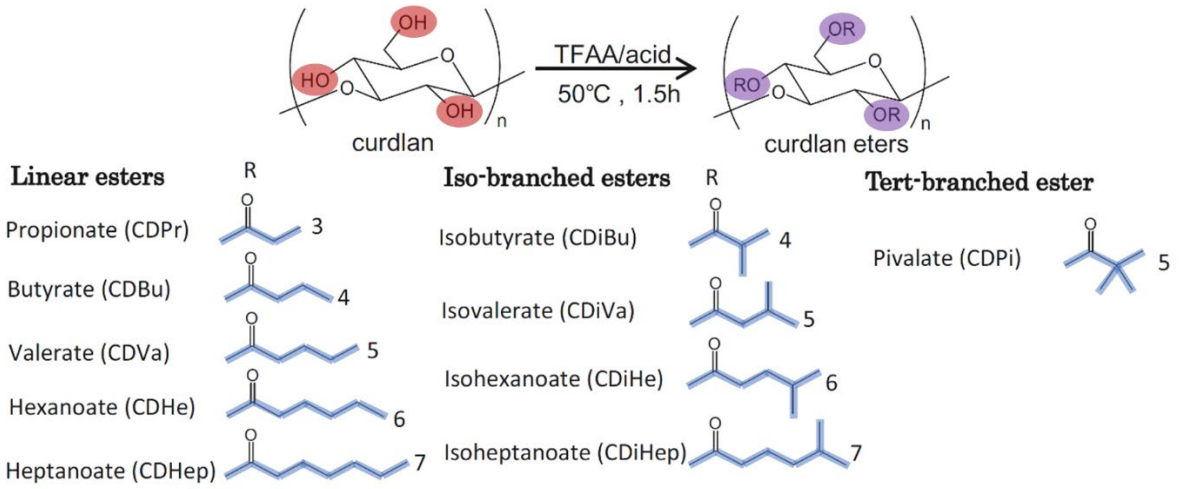

Figure 3. Synthesis and the structures of curdlan branched and linear esters. (Reproduced from ZHAI et al. [73] Copy from SPRINGER 2017)

Gan et al. used paramylon, which is a β-1,3-(D)-glucan to synthesize paramylon alkyl esters with the N in side chain from 2-12.[74] Compared the neat paramylon with its esters, the thermal stability can be improved by the esterification process. The esters can crystallize when N is between 2 and 6, while they are amorphous when N is between 8 and 12. Thus, the softness and hardness of the films fabricated from paramylon esters can be controlled by N. Shibakami and Sohma also studied the thermal properties of paramylon monoesters with N of 14, 16 and 18.[75] It was found that the obtained esters with N of 14 and 16 exhibit less ordered lateral acyl chain structures than those with N of 18. Puanglek et al. reported the fully substituted α-1,3-(D)-glucan esters with N of 2, 3, 4, 5, 6 and 8.[76] It also verified the conclusion that esterification can improve the thermal stability of α-1,3-(D)-glucan. Crystals can be detected from esters with N of 2, 3, 4, 5, 6 while not the one of 8. Furthermore, T_m of α-1,3-(D)-glucan esters are higher than other normal plastics. Besides, it was found that T_g and T_m decrease with the increasing of N. The longer side chain length leads to lower tensile strength and higher elongation at break.

1.4 Role of backbone during crystallization and application of carbohydrate esters

The crystallization of carbohydrate esters is not mainly depending on side chains, backbone also plays a pivotal role and exhibits mutual functions with side chains. The structure of backbone and degree of polymerization (DP) are the two most essential factors affecting the crystallization of carbohydrate esters. A huge variety of backbones can be found in the commonly used polymers, especially aromatic backbone, aliphatic backbone and sugar-ring backbone.

Regarding to the polymers with aromatic backbones, for example PET, the benzene rings in the aromatic repeating units result in the backbone of PET with all carbon atoms in the same plain. Thus, π-π stacking endows polymer chains (backbones) of PET more possibilities to interact with each other and then lead to the excellent mechanical stability, thermal and chemical resistance.[77,78] Compounds with aliphatic backbones such as poly (butylene succinate) (PBS) and poly (lactic acid) (PLA) show excellent bio-degradability and can crystallize by the interaction of Van der Wall force due to the flexible molecular chains. [79-81]

Beside the most commonly studied aromatic and aliphatic backbones, backbones with sugar-rings exhibit unique characters during application. The most common sugar-ring in nature is (D)-glucopyranose consisting of 5 carbons and 1 oxygen. As mentioned in **Figure 1a**, two stretching directions of the hydroxy groups at C1 in glucose can lead to the formation of α- and β-glucose. When similar situation happens to the hydroxy groups at C2 and C4 in glucose, mannose and galactose are formed instead of glucose. These monosaccharides with diverse configurations exhibit significant diversities in properties.

As the most important compound in human body and food industry, glucose can be used in pharmaceutical and chemical industries. Glucose can be easily obtained from hydrolysis of starch, which can be found in corn and potato et al.[82] Thus, glucose has been known by its low-cost and huge amount in nature. Under the ambient conditions, glucose exists as glucose monohydrate. Crystallization of glucose monohydrate is processed by dissolving glucose in water and evaporating the water molecules to produce supersaturate solution at lower temperature. It was verified that α-glucose is the key component used to produce crystals due to its stability instead of β-glucose as shown in **Figure 4**.[83]

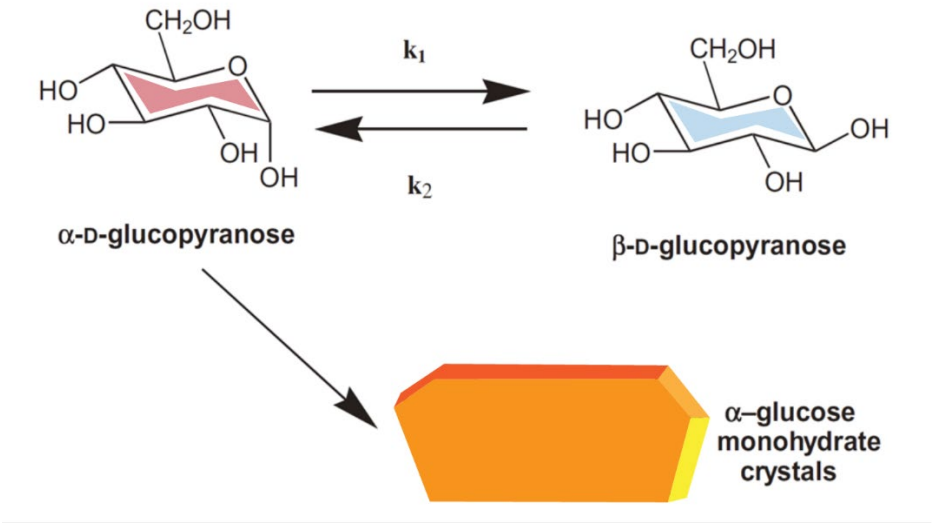

Figure 4. Simplified reaction scheme for the crystallization of α-glucose monohydrate under conditions where this is the stable form. Only the glucopyranose anomers have significant concentrations in solution at the conditions considered. (Reproduced from FLOOD et al. [83] Copyright from ELSEVIER 2012)

Schmidt-Lassen and Lindhorst reported the formation of micelles in water by using a series of octyl α- and β-glycosides of the manno- galacto- and gluco-series.[84] Anomeric configuration and epimerization at the sugar ring were found to play an essential role to the supramolecular features of the respective glycoside as shown in **Figure 5**. The tendency of forming micelles in water increases from galactose over glucose to mannose. To be precise, α-Man ≈ α-Glc > α-Gal, β-Man > β-Glc > β-Gal. Besides, it was found that α form is more easily to be employed to fabricate micelles than β form. Overall, octyl α-mannoside exhibit the lowest critical micelle concentration (CMC) for the formation of micelles in water.

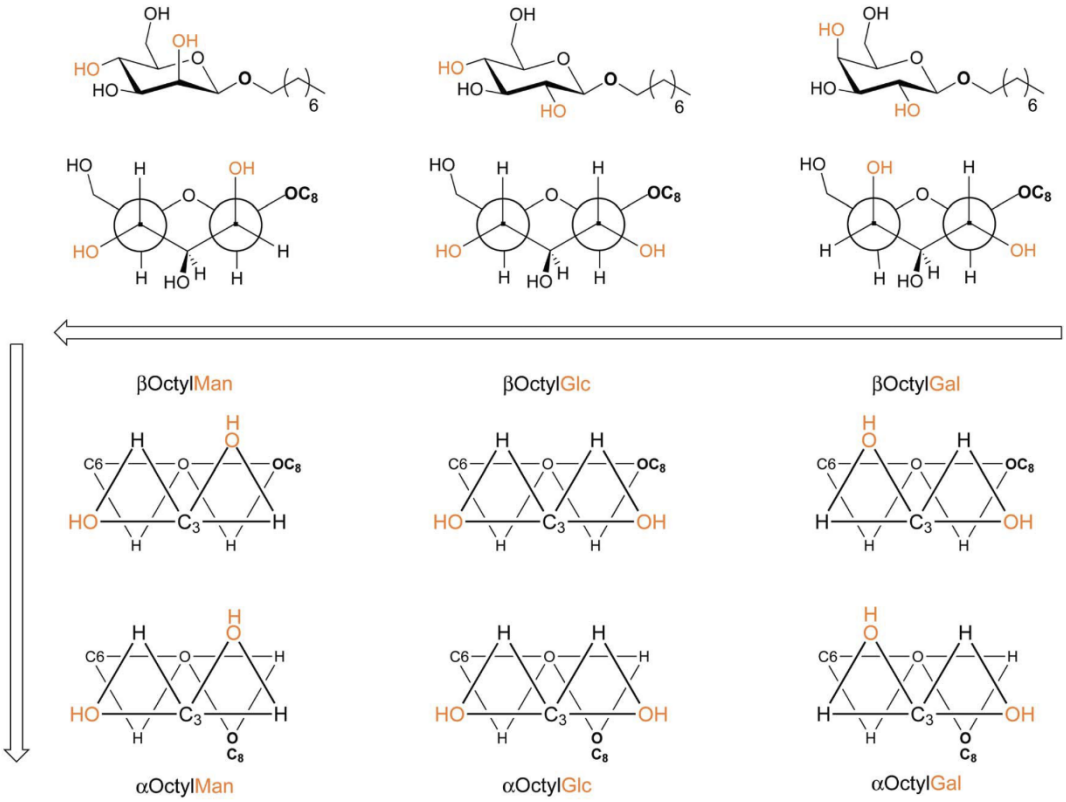

Figure 5. A new view on structural characteristics of the investigated α- and β-octyl glycosides is suggested and related to classical chair conformations and Newman projections, respectively. This structure representation highlights the variable hydroxyl groups at C-2 and C-4 of the sugar ring at respective edges of two fused front face triangles, in relation to another two triangles representing the far end of the glycoside. The relative positioning of the octyl aglycone to the front face triangles depends on whether the depicted glycoside is a- or b-configured. Increasing ease of micelle formation is indicated by arrows with αOctylMan requiring the least concentrated solution for micelle formation in water. (Reproduced from SCHMIDT et al. [84] Copyright from Royal Society of Chemistry 2014)

Furthermore, if the sugar-ring in glucose is connected as a repeating unit by connection at C1 and C4, two most common polysaccharides, cellulose and amylose are obtained. Cellulose and amylose are both linear polysaccharides with the repeating unit of glucose connected by β (1→4)

glycosidic bonds and α (1→4) glycosidic bonds, separately. Even though they exhibit similar chemical structures, their crystallization properties differ significantly. In cellulose, the repeating glucose units follow a 2-fold helicoidal path, whereas a 3-fold helical conformation is formed in amylose. Thus, amylose molecules are more flexible and have more degree of freedom than those from cellulose, whereas cellulose has more crystalline than amylose.[85,86]

1.5 How backbone and side chain affect the fabrication of microparticles/nanoparticles from carbohydrate esters.

The obtained carbohydrate esters mentioned in 1.3 can not only be utilized as plasticizers and films during application, but also as microparticles and nanoparticles. Since the preparation of microparticles/nanoparticles has been studied for decades, quite a lot of sophisticated methods have been reported including solvent evaporation[87], salting-out[88], nanoprecipitation[89] and dialysis[90].

Solvent evaporation method is the first and widely applied method to fabricate microparticles/nanoparticles. During the fabrication process, the compounds are first dissolved into volatile solvents. With the evaporation of the solvents, emulsions are formed. The commonly used volatile solvents are dichloromethane and chloroform. However, recently, ethyl acetate is more widely appointed due to its lower toxicity.[91] Even though the solvent evaporation method has been profoundly used in lab, the requirement of organic solvents constrains its further application because of the hazardous properties to the environment. Thus, a more environmental-friendly method called salting-out with the usage of water and salts is brought up. First, make sure the compound solvents are miscible to water. Then, salts such as magnesium chloride[92], calcium chloride[93] and magnesium acetate[94] are added to provide a strong salting-out effect. Nanoprecipitation is a method requiring two miscible solvents: a volatile solvent and a nonsolvent to the compound. The compound is dissolved into the solvent and then the solution is added into the nonsolvent. The diffusion process leads to the decrease of the interfacial tension and increase the surface area. Thus, small droplets of the compounds formed. Dialysis is a method similar to nanoprecipitation with two miscible solvents combined in the process. The

main difference between nanoprecipitation and dialysis is that a dialysis tube is involved in the dialysis process instead of directly mixing the two solvents together in nanoprecipitation.

To date, quite a few publications have studied the fabrication of microparticles from carbohydrate esters and how backbone and side chain work during the formation of microparticles. Edgar et al. published a review comprehensively introducing the diverse cellulose acetate-based system of preparation of microparticles, including cellulose acetate (CA) and its derivatives including cellulose acetate butyrate (CAB), cellulose acetate propionate (CAP) cellulose acetate phthalate (C-A-P), cellulose acetate trimellitate (C-A-T) and cellulose acetate succinate (C-A-S), which exhibit promising application in enteric coating.[95] The above-mentioned cellulose esters cannot only be solely used for application, but also applied as the addition of non-toxic plasticizers or the component in blends with other polymers.

Pastor et al. reported the preparation of microparticles from the combination of C-A-P and alginate to encapsulate heat-killed Vibrio cholerae, which can be used as Oral cholera vaccine.[96] The obtained microparticles had the size of 6 μm and the loading drug content around 8.5%. Not like poly (methacrylic acid-co-ethyl acrylate) polymer can only form irregular microparticles, microparticles from C-A-P exhibited regular morphology under the similar conditions. This proves the important role of backbones with sugar-rings and ester side chains.

Hadef et al. reported the synthesis of alkyl and hydroxyalkyl alginate esters and comparison of their capsulation efficiency to human serum albumin.[97] It was found that during the formation of microparticles, hydrophobic microdomains were firstly formed by the association of side chains of alkyl alginate esters at lower polymer concentrations compared to those of hydroxyalkyl alginate esters with the same DS and N. Furthermore, with the increasing of DS and N, critical aggregation concentration decreases.

Cardea and Marco's newly published paper introduced how microparticles were formed from CA by using ternary diagrams via two supercritical carbon dioxide ($scCO_2$) based techniques, to be precise, semi-continuous supercritical antisolvent process and supercritical fluid phase inversion process.[98] By adjusting the pressure, temperature, concentration and parameters of $scCO_2$, microparticles and nanoparticles with diverse morphologies and properties in application

can be obtained. As shown in **Figure 6**, the paths of the formation of micro- and nanostructures were depicted in ternary diagrams. When the concentration is high, the path goes in the curve of A. With lower concentration, it goes in path B, while it goes in path C when the concentration is the lowest. When the pressure is set at 10 MPa, the path goes in the curve of D, whereas the process goes in E with higher pressure of 20MPa.

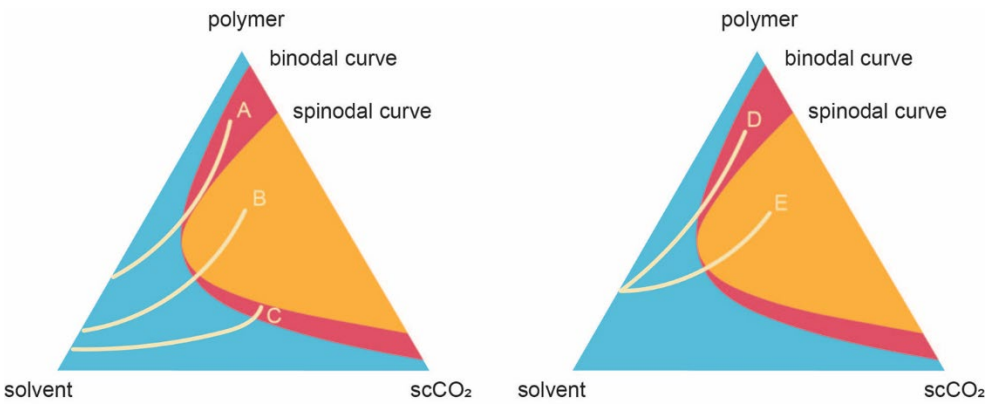

Figure 6. Qualitative ternary diagrams; (a) paths at different starting polymer concentrations at 8 MPa and 45°C; (b) paths at different operating pressures at 160 mg/mL and 45°C. (Reproduced from CARDEA et al. [98] Copyright from MDPI 2020)

To date, the most commonly reported microparticles from carbohydrate esters have the solid morphology. However, porous flower-like microparticles (FLPs) with unique hierarchical superstructures are still rare and understudied. Zhang[99] first reported the formation of FLPs from cellulose stearoyl esters by solvent-induced self-assembly. It shows that the molecular weight, concentration and solvent ratio are essential for the solvent-induced FLPs. Then, Wang[100] systematically studied the conditions of the formation of FLPs via temperature-induced self-assembly. It turns out that the molecular weight, concentration and the cooling rate are the key factors. Furthermore, Wang[101] compared the self-assembled superstructures from cellulose stearoyl esters and polyvinyl stearoyl esters. Due to the difference in backbones, cellulose esters

can form well-organized flower-like microparticles, while polyvinyl esters can only form non-ordered superstructures.

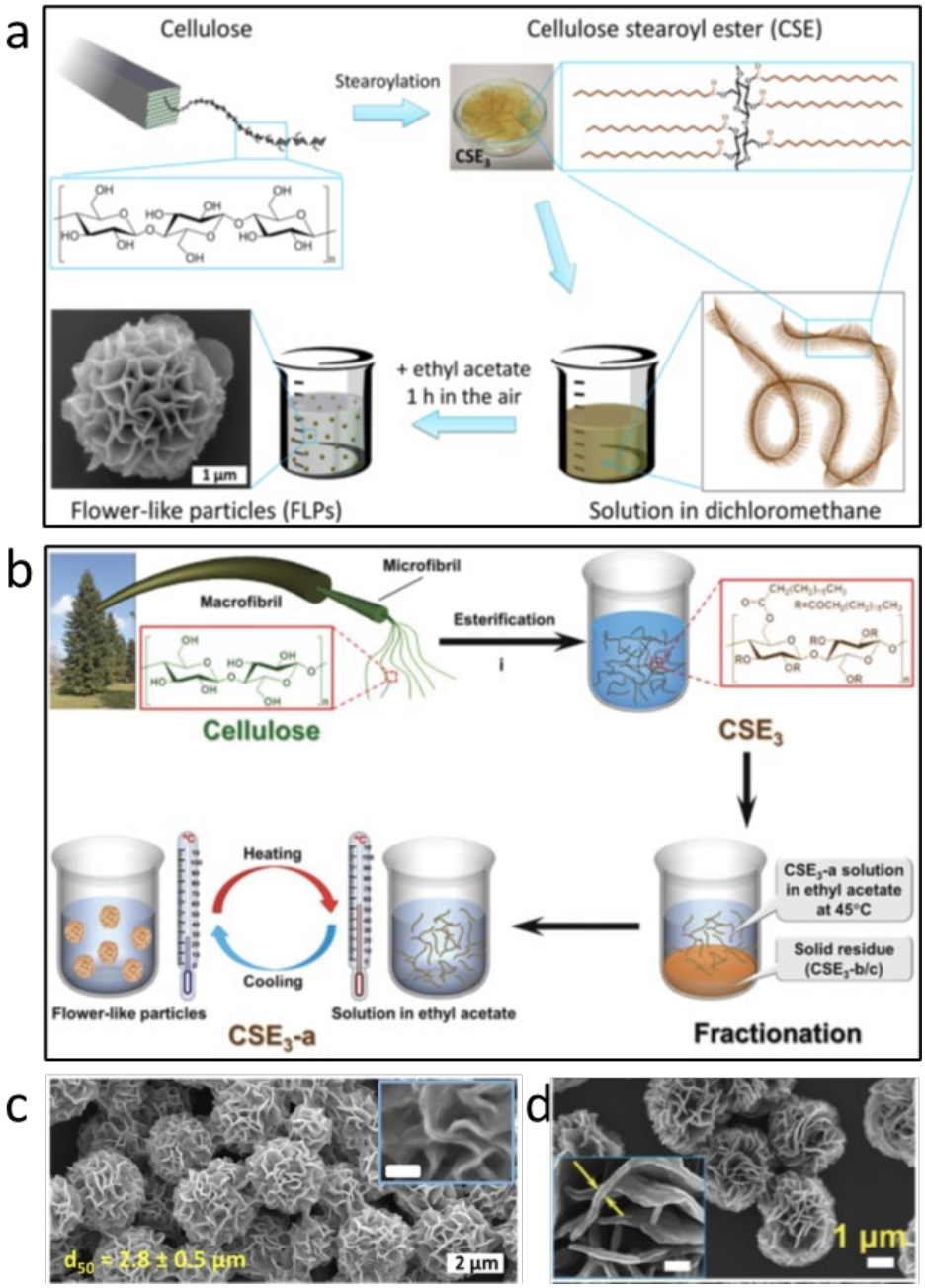

Figure 7. Schematic illustration of the formation of self-assembled flower-like microparticles via a) solvent-induced and b) temperature-induced methods; SEM images of the prepared FLPs from

c) solvent-induced and d) temperature-induced methods. (a and c: reproduced from Zhang et al. [99] Copyright from ACS Publications 2015; b and d: reproduced from Wang et al. [100] Copyright from Wiley 2016)

Beside the particles in microscale, smaller particles in nanoscale also exhibit promising properties. The most widely studied carbohydrate esters are also cellulose acetate (CA) and its derivatives. Hornig and Heinze et al. reported the fabrication of nanoparticles from CA by nanoprecipitation and dialysis with the solvents of DMAc and acetone.[102,103] They studied the formation of nanoparticles from the fully substituted CA and partially substituted CA, it turns out that the fully substituted CA can only form undefined aggregates, while the CA with lower DS of 1.6 can form nanoparticles after dialysis. This can be explained by the attractions and repulsions of the side chains. In fully substituted CA, the repulsions from side chains lead to the stretching of the molecules and then to rigid rods. However, in partially substituted CA, the existed hydroxy groups and the distribution pattern of the side chains play an important role during the formation of nanoparticles. Furthermore, CA compounds with the same DS prepared from different methods also lead to the diversities in forming of nanoparticles. CA with the DS of 2.05 prepared from the hydrolysis of cellulose triacetate can form nanoparticles via dialysis. On the contrary, CA with a comparable DS from direct synthesis path can only form aggregates. This can be explained by a huge amount of existed hydroxy groups at C3 in CA, which lead to the formation of intermolecular hydrogen bonds and thus to the undefined aggregates. Moreover, the morphology of the nanoparticles can also be controlled by the fabrication methods and conditions. As shown in **Figure 8**, nanoparticles prepared by dialysis with DMAc (**Figure 8a**) exhibited normal nanospheres, while the particles fabricated via directly adding of water into acetone exhibit bean-shaped nanospheres.

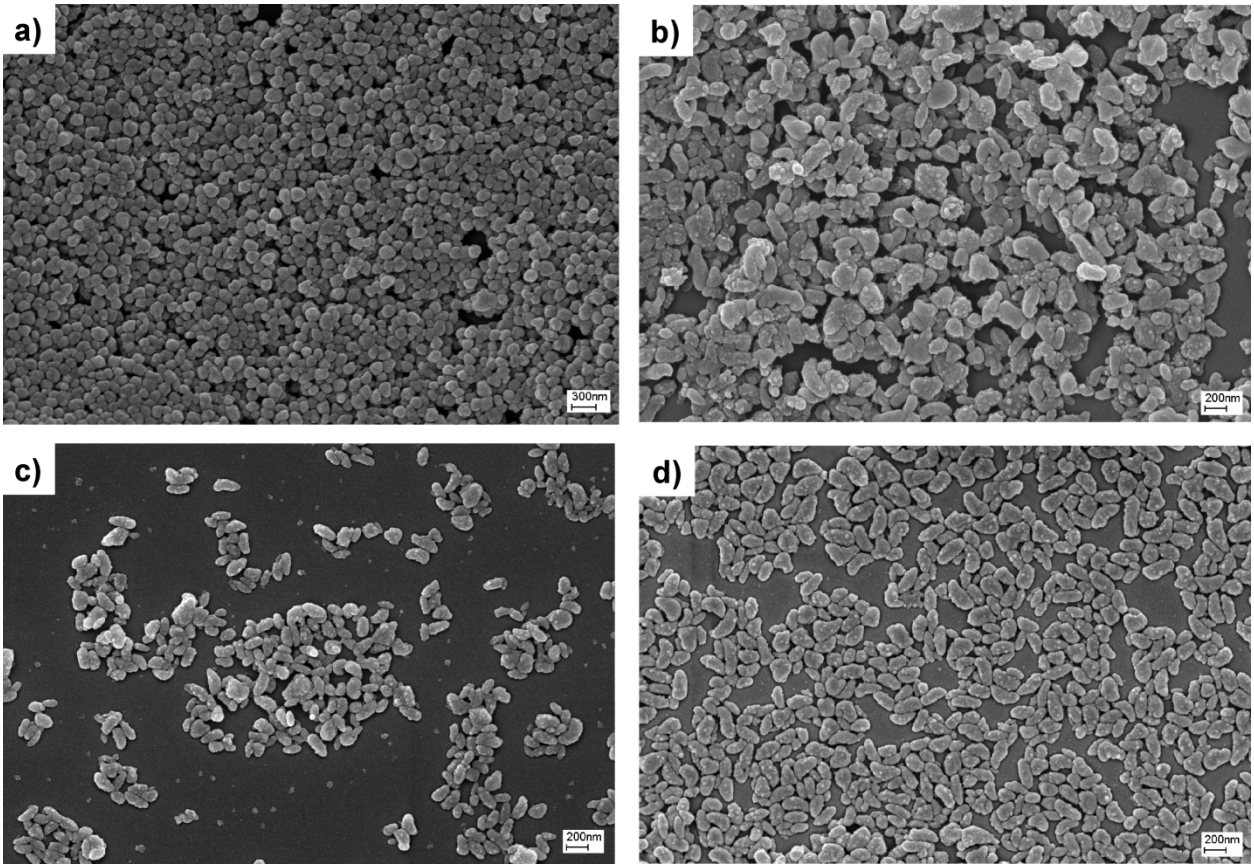

Figure 8. SEM images of nanoparticles of cellulose acetate (CA, DS_{Ac} 2.46) on a mica surface prepared by dialysis of (a) polymer dissolved in DMAc (c=4 mg CA/mL) and (b) polymer dissolved in acetone (c = 4 mg CA/mL) against water and by the dropwise adding of water into an acetone solution of the polymer containing (c) 1 mg CA/mL and (d) 4 mg CA/mL. (Reproduced from HORNIG et al. [102] Copyright from ACS Publication 2008)

Mazumder et al. reported the preparation of nanoparticles from CA based polymers including carboxymethyl cellulose acetate butyrate (CMCAB), cellulose acetate propionate 504-0.2 adipate 0.33 (CAP Adp 0.33), cellulose acetate propionate adipate 0.85 (CAP Adp 0.85) and cellulose acetate 320S Sebacate (CA 320S Seb) to encapsulate poorly soluble antiviral drugs via rapid precipitation process.[104] It was found that the increasing of DS can lead to the increasing of more effective inhibition of crystallization. This can be explained by the more existed ionized carboxylic acids.

Beside the cellulose acetate and its derivatives as mentioned above, cellulose esters with longer alkyl side chains have also a huge potential use in the fabrication of nanoparticles.

Nau et al. reported the synthesis of hydroxypropyl cellulose ester by using hydroxypropyl cellulose and fatty acid chlorides including lauric, myristic, palmitic and stearic acid.[105] It was found that the reaction rate of the hydroxypropyl cellulose esters is mainly depending on the length of the side chains. Longer side chains lead to higher reaction rate. During the reaction, the backbone of the polymer coils can unwind to a wider degree when synthesizing with stearic acid, while the degree is smaller when synthesizing with shorter side chains. Wider degree results in more reaction sites. Then, the formed esters were used to fabricate hydrophobic nanoparticles via nanoprecipitation.

More functions can be added to nanoparticles obtained from cellulose esters with longer side chains by adding additions. Geissler et al. fabricated stimuli-responsive, fluorescent and magnetic nanoparticles by using cellulose stearoyl esters (CSE) and additions including Fe_3O_4-NPs, rhodamine B (RhB) and stearoylaminoethyl rhodamine B (C18-RhB) via nanoprecipitation.[106] In comparison of CSE-RhB and CSE-C18-RhB nanoparticles, C18-RhB can be perfectly encapsulated into the nanoparticles, while RhB cannot. This can be explained by the polarity of RhB. Due to the long aliphatic C18 chains, C18-RhB can interact with CSE via hydrophobic-hydrophobic interactions, which enhanced the encapsulation.

Apart from solely using cellulose esters, nanoparticles can also be obtained by coprecipitation of cellulose esters and hydrophilic polysaccharides. Kulterer et al. fabricated the composite nanoparticles based on CA and hydrophilic polysaccharides including hydroxyethyl cellulose, carboxymethyl cellulose, low molecular weight chitosan, and amino cellulose via nanoprecipitation.[107] It was found that the hydrophilic polysaccharides can diffuse into the surface of CA-rich domains via hydrophobic interactions, which are from the sugar-ring backbones and act as dispersing agents due to electrosteric interactions, which are from the hydrophilic hydroxy groups. Finally, the hydrophilic polysaccharides can be entrapped into the CA matrix during the phase separation. Thus, the morphology and size can be controlled by adjusting the pH of the solution.

Beside the widely studied cellulose based polymers, other carbohydrate esters including dextran-based esters and xylan esters have also been investigated. Liebert and Heinze et al. synthesized the highly functionalized amphiphilic dextran propionate pyroglutamate with biocompatible propionate and pyroglutamate moieties via a two-step esterification.[108] Afterwards, nanoparticles were obtained by dialysis with distilled water. The high DS avoids the partial restoration of the hydrogen-bond-based superstructure of the backbone and thus leads to the metastable nanostructures of the formed nanoparticles. Hornig and Heinze et al. reported the synthesis of dextran furoate pyroglutamate and then used this compound to fabricate nanoparticles.[109] The size of the nanoparticles can be controlled by the molecular weight and DS of the dextran esters. Hornig and Heinze et al. also synthesized multifunctional dextran esters with side chains of furoyl-, pyroglutamyl-, propyl-, and acetyl moieties and diverse DS as shown in **Figure 9**.[110] The nanoparticles were fabricated by the obtained compounds via dialysis using DMAc and distill water. It was found that nanoparticles with regular morphology can only be successfully formed when the DS is higher than 2. Besides, the size of the nanoparticles can be increased with the decreasing of molecular weight. Furthermore, they also reported the synthesis of xylan furoate pyroglutamate to form nanoparticles by similar process as used to prepare nanoparticles from dextran esters.[111] Based on the unique functional groups, all nanoparticles from dextran esters and xylan esters have a promising application in encapsulation of hydrophobic core materials.

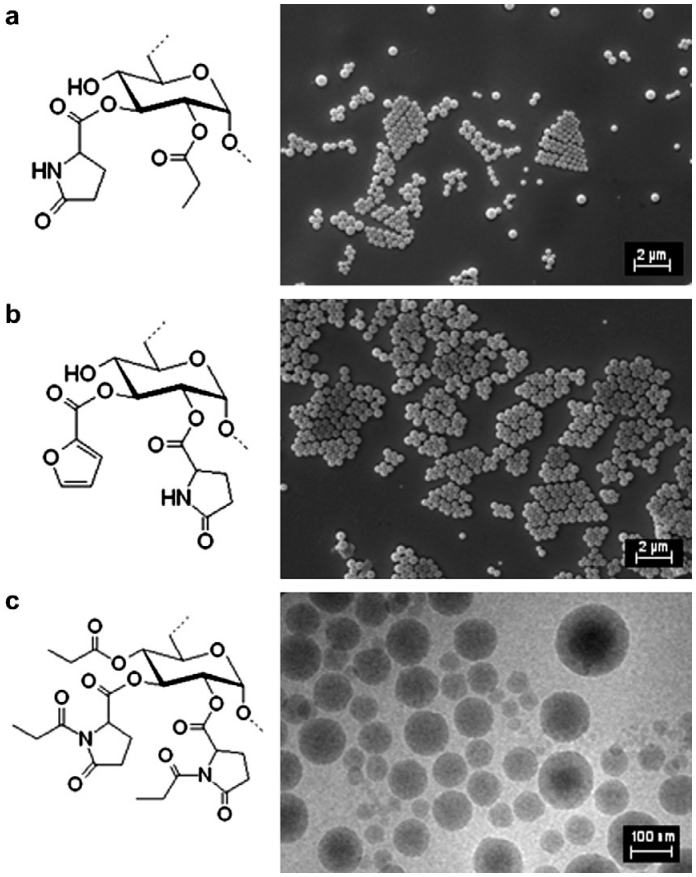

Figure 9. Schematic structures of dextran derivatives and corresponding images (SEM for a and b, cryo-TEM for c) of the nanoparticles formed by dialysis (DMAc/H_2O); (a) dextran propionate pyroglutamate; (b) dextran furoate pyroglutamate; (c) perpropionylated dextran pyroglutamate. (Reproduced from HORNIG et al. [110] Copyright from ELSEVIER 2007)

2. Object of the study

Superstructures derived from carbohydrates and their derivatives via self-assembly have attracted abiding interests due to their potential applications in distinct fields, such as biomedicine, nanotechnology, hydrophobicity and catalysis. This is primarily due to their low-cost, abundance, and environmental friendliness in comparison to other raw materials. However, still some problems challenge us including the roles of backbones and side chains during the formation of superstructures, precise control of their morphologies and the application of these unique structures. In order to solve these problems, we came up with three strategies:

1. To synthesize cellulose stearoyl ester (CSE) and glycerol stearoyl ester (GSE); to prepare hydrophobic and superhydrophobic coatings on wood surface by dip-coating of CSE and brush-coating of GSE; to study the anti-fungal properties of the coating and to elucidate the role of the backbones of cellulose, the monomer structure of glycerol and the fatty side chains with 18 carbons.

2. To synthesize D/L-glucose stearoyl esters (D/L-GlcSE) with diverse α/β-configurations; to form chiral microparticles by D/L-GlcSE and to demonstrate the role of D/L- and α/β-configurations during the formation of chirality.

3. To synthesize D-monosaccharide stearoyl esters (D-MSSEs) with diverse bond configurations including D-glucose stearoyl ester (D-GlcSE), D-xylose stearoyl ester (D-XylSE), D-galactose stearoyl ester (D-GalSE) and D-mannose stearoyl ester (D-ManSE); to prepare flower-like microparticles by D-MSSEs and to illustrate the role of bond configuration at C1, C2, C4 and C6 during the formation of self-assembled flower-like microparticles.

3. Results and discussion

3.1 The role of backbones and aliphatic side chains in hydrophobicity and superhydrophobicity for anti-fungal effects

As reported in **Publication 1**, cellulose stearoyl ester (CSE) and glycerol stearoyl ester (GSE) were synthesized and applied for the preparation of hydrophobic and superhydrophobic surfaces on wood substrates as anti-fungal effects, as shown in Scheme 1.

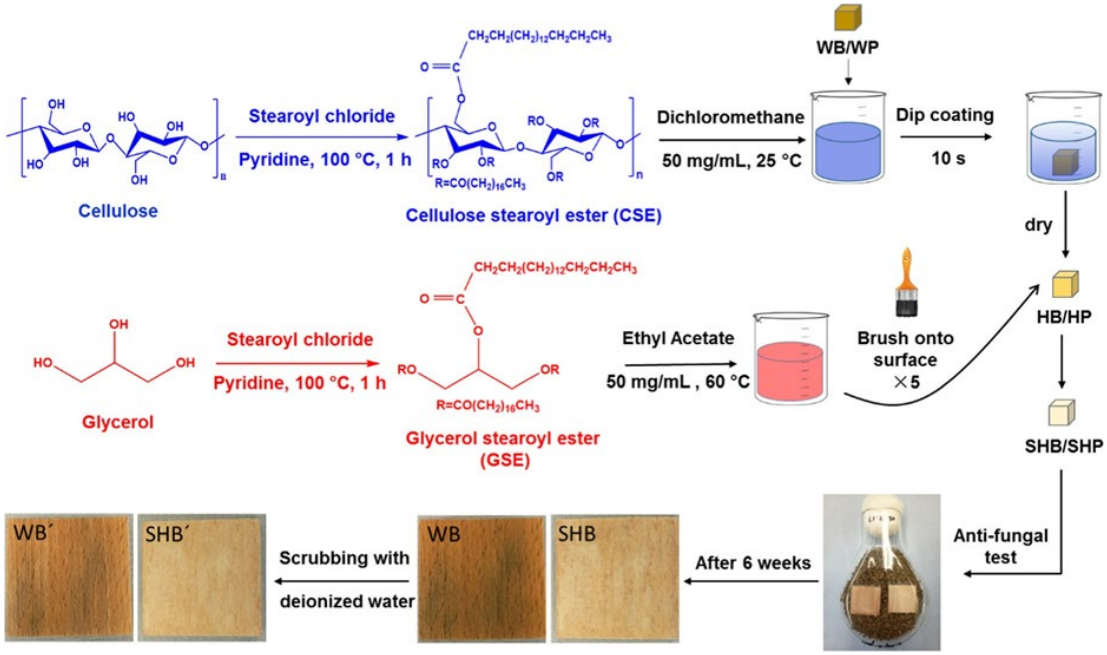

Scheme 1. Schematic overview for the synthesis of cellulose stearoyl ester (CSE) and glycerol stearoyl ester (GSE) as well as the fabrication of hydrophobic beech/pine (HB/HP) and superhydrophobic beech/pine (SHB/SHP) by using washed beech/pine (WB/WP) and anti-fungal test.

As shown in **Figure 10**, it is obvious that these coating treatments didn't lead to a notable change of the appearance of both beech and pine samples. However, their surface wettability was significantly modified, as represented by static water contact angle (SWCA). SWCAs of water

droplets on WB and WP are 64° and 80° after 5 s, respectively. After the dip-coating in CSE solution and drying, the SWCAs on HB and HP increased to 122° and 118°, showing enhanced hydrophobic properties. After further brush-coating with GSE solution, the SWCAs of SHB and SHP increased to 159° and 155°, respectively. These results confirmed the successful formation of hydrophobic and superhydrophobic wood surfaces using the two coating steps. In addition, the insensitivity of the method to substrates further shows the applicability of these methods and the coating materials to increase the surface hydrophobicity of diverse other substrates.

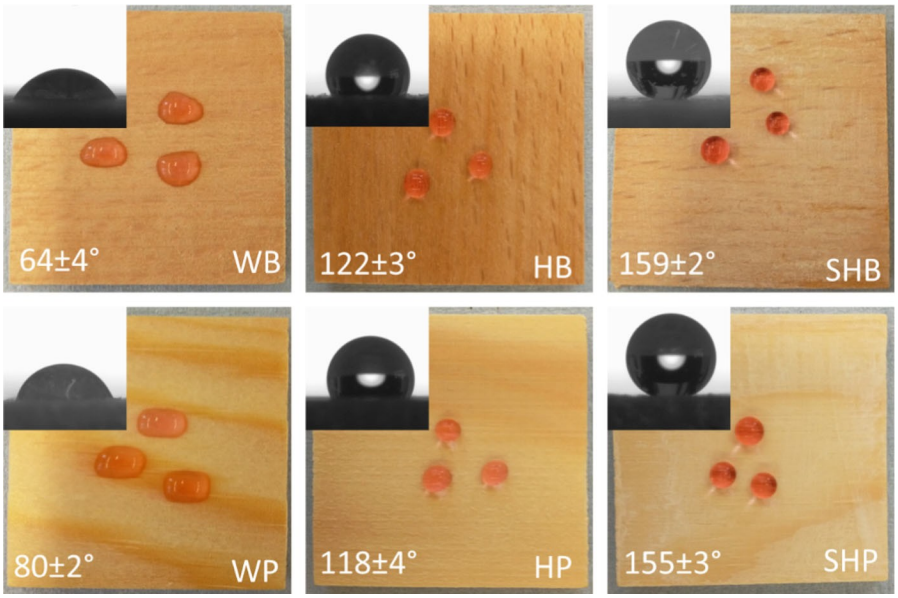

Figure 10. Appearance and SWCA (in insets) of non-treated and treated wood from beech (WB, HB and SHB) and pine (WP, HP and SHP). The water droplets were dyed with tee and the photos were taken after the droplets put onto wood for 5 s.

Comparing the SEM images of WB/WP with those of HB/HP in **Figure 11**, a relatively smooth and continuous membrane with cracks could be observed under higher magnification on HB/HP. This should be due to the formation of the continuous CSE layer on the rough wood surface, which partially fills the cavities at the surface during the fast evaporation of DCM. Thus, the low surface roughness of this thin CSE layer can only contribute to the formation of hydrophobic surfaces. The evaluated thickness of the hydrophobic coating on wood surface should be slightly

less than 53 nm. In comparison to HB/HP, subsequent brush-coating of GSE for the fabrication of SHB/SHP led to extremely coarse surfaces with a highly-textured cellular structure. This structure is based on the crystallized GSE at the surface, which enhanced the surface roughness at microscale. This structure should contribute to the formation of superhydrophobic surfaces by trapping air between wood surfaces and water droplets. According to the SEM measurements, we can estimate that the thickness of 2nd layer on wood surfaces should be between 20 and 30 μm.

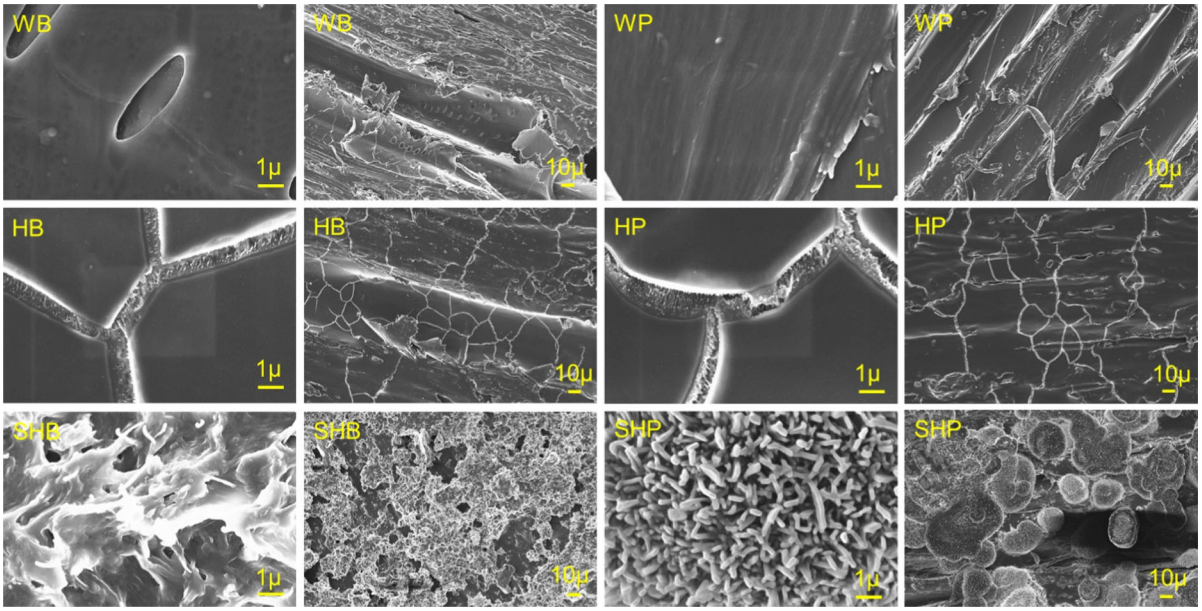

Figure 11. Representative SEM images of wood surfaces of beech (WB, HB and SHB) and pine (WP, HP and SHP) at diverse magnifications.

Figure 12 exhibits the appearances of treated and untreated wood samples after fungal cultivation and comparison of wood appearance before and after scrubbing with deionized water. Grey and black dots belonging to the spores of fungi were present on WB/WP surfaces after fungal cultivation. After scrubbing with deionized water, significant amounts of grey and black dots still existed on WB'/WP' surfaces, which can be explained by the intrusion of fungi inside the wood samples. However, HB/HP samples exhibited fewer spores on the surface after the

cultivation of fungi, which illustrated better anti-fungal properties compared with WB/WP. After scrubbing with deionized water, fewer grey and black dots can be found on HB'/HP' wood surfaces. In comparison, much fewer spores are notable on the SHB/SHP surfaces after fungal cultivation. These spores could be easily removed by scrubbing with deionized water, leading to SHB'/ SHP' with clean surfaces again.

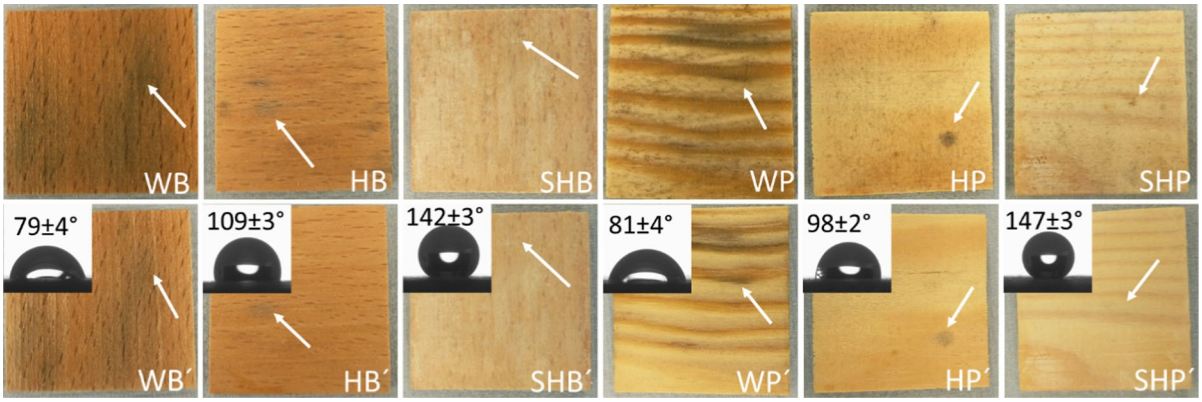

Figure 12. Representative photo images of wood samples after anti-fungal test for 6 weeks and SWCAs on wood surfaces after further scrubbing with deionized water: WB/WP, HB/HP, SHB/SHP were the wood samples after 6 weeks anti-fungal test. WB'/WP', HB'/HP', SHB'/SHP' were the same samples after further scrubbing with deionized water.

3.2 Role of D/L and α/β configurations in the glucose ring during the formation of chiral microparticles via self-assembly

According to the **Publication 2**, D/L-glucose stearoyl esters (D/L-GlcSE) were obtained by synthesizing glucose with stearoyl chloride in pyridine at 100°C for 1 h under N_2 atmosphere. After the synthesis, both obtained D- and L-GlcSE exhibited the ratios of α/β anomers of 20/80. Thus, the involved D/L-GlcSE are named as D-GlcSE20/80 and L-GlcSE20/80. By decreasing the temperature of D/L-GlcSE20/80 solutions in ethyl acetate with the concentration of 1 mg/ml from 60°C to 25°C and aged for 20 min at 25°C, chiral microscaled precipitates with flaky nanostructures were formed instantly (**Figure 13b** and **d**). As shown in **Figure 13e-l**, different aging time at 25°C of 0, 10, 20 and 40 min led to petal shapes, cookie shapes

and microparticles, respectively. Based on the results, the chiral, mirror-imaged, cookie-shaped microparticles can only be obtained from D/L-GlcSE20/80 by controlling the aging time for 20 min at 25°C due to the mirror-imaged D/L-configuration and proper α/β ratio in GlcSE. The D- and L-configurations of the GlcSE molecules lead to the opposite directions of the displacement during self-assembly and thus mirror-imaged chirality formed. According to the DSC measurement of the microparticles from L/D-GlcSE20/80, they exhibit absolutely the same thermal properties. To be precise, both L/D-GlcSE20/80 have the same melting temperature (T_m) of 81°C and two crystallization temperature (T_c) of 46°C and 56°C.

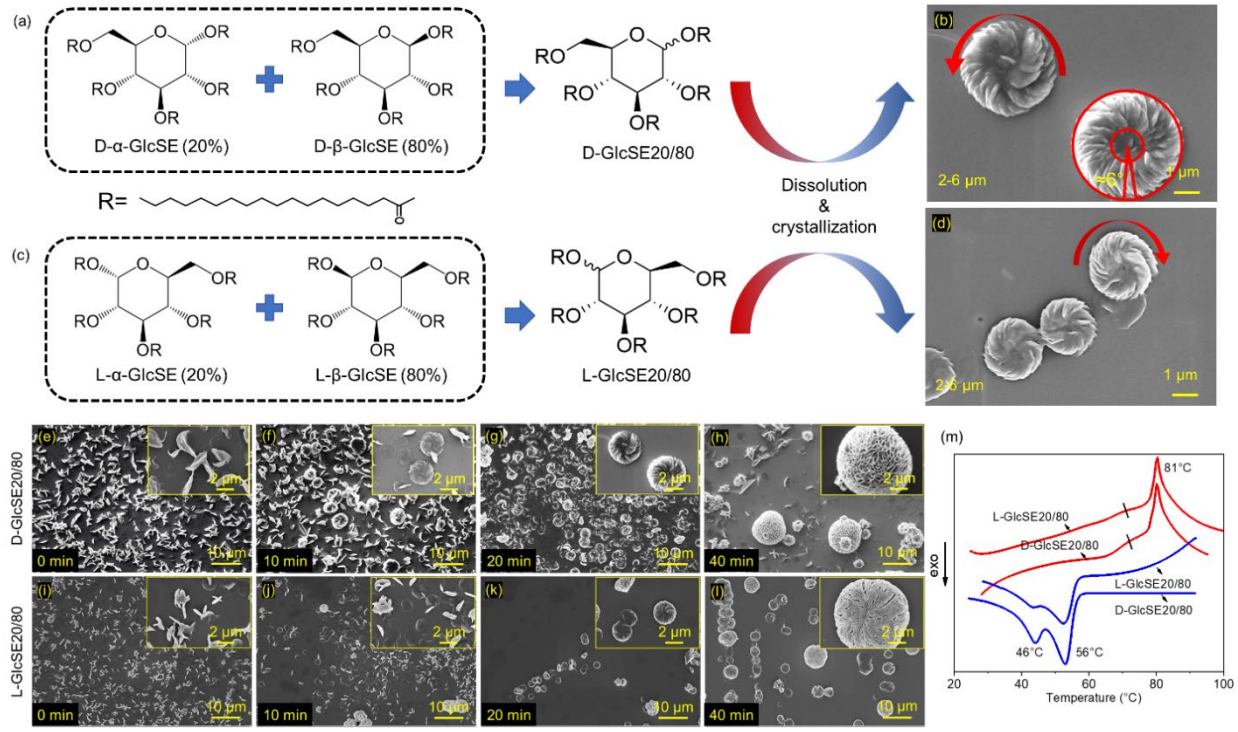

Figure 13. Chiral microparticles from D/L-GlcSE20/80 and the formation process. a and **c)** Haworth structures of D/L and α/β configuration of GlcSE; SEM images of **b)** left-handed and **d)** right-handed microparticles; SEM images of self-assembled aggregates from **e-h)** D-GlcSE20/80 and **i-l)** L-GlcSE20/80 prepared with their solutions in ethyl acetate at the concentration of 1 mg/mL from 60°C to 25°C with the cooling rate of 1 °C/min and aged at 25°C for 0, 10, 20 and 40 min, respectively. **m)** DSC heating and cooling curves of L/D-GlcSE20/80.

The aging processes at other temperatures including 30°C (**Figure 14a-c**) and 20°C (**Figure 14d-f**) were also studied with different aging times. When aging at 30°C for 0 min, the precipitates tend to form a

ring-shape prototype of microparticles. With the increase of aging time, round-shape microparticles were obtained. On the contrary, aging at 20°C can easily promote the formation of irregular aggregates, which can be seen as the overgrown petals. However, neither of them can form chirality.

During the experiment, it was found that the solubility of D-β-GlcSE in THF is slightly lower than D-α-GlcSE. Thus, the preparation of D-GlcSE with diverse α/β ratios can be achieved by dissolving D-GlcSE20/80 in THF and filtration. Four different α/β ratios of 70/30, 40/60, 20/80 and 03/97 were determined and are named as D-GlcSE70/30, D-GlcSE40/60, D-GlcSE20/80 and D-GlcSE03/97, respectively. When prepared under the same conditions, at the α/β ratio of 70/30, the self-assembled D-GlcSE exhibits irregular aggregates (**Figure 14g**), whereas by increasing the fraction of β configuration, petal shapes (**Figure 14h**), cookie shapes (**Figure 14i**) and microparticles (**Figure 14j**) were obtained. We note that only cookie shapes prepared from D-GlcSE20/80 show chirality.

D-GlcSE with diverse α/β ratios were further measured by DSC and SAXS. According to the DSC heating curves (**Figure 14k**), D-GlcSE03/97 with 97% β-configuration exhibits the highest melting temperature (T_m=84°C), while GlcSE70/30 with 70% α-configuration shows the T_m of 65°C. Similarly, D-GlcSE03/97 with 97% β-configuration exhibits the highest T_c of 62°C, while D-GlcSE70/30 with 30% β-configuration has the lowest T_c of 34°C, see **Figure 14l**. Interestingly, two peaks emerge in the DSC cooling curves of D-GlcSE40/60 and D-GlcSE 20/80. This can be explained by the discrepant crystallization properties of α/β configurations. SAXS measurement was also employed to understand the crystallization properties of the D-GlcSE with diverse α/β ratios. As shown in **Figure 14m**, all samples exhibit similar SAXS patterns of 4 Bragg peaks, which show the semi-crystalline nature of the samples in two-dimensional substructures. The ratio of the Bragg reflexes of q1/q2/q3 is 1:2:3, which results in a lamellar packing. The sharpness of the peaks is most pronounced for D-GlcSE03/97, compared to D-GlcSE with other α/β ratios. Besides, with more α-configuration inside, the 3rd peak in SAXS (marked in **Figure 14m**) exhibit an obvious shoulder, which represents the different crystallization properties from α/β-configuration. We can conclude that α configuration leads to irregular aggregates, which show worse thermal and crystallization properties, while mature round smooth microparticles with better thermal and crystallization properties are beneficial from β configuration. This is because axially stretched α configuration increases the difficulties of stacking of molecules during self-assembly, while better stacking is beneficial from equatorially stretched β configuration. However, only when appropriate number of bonds stretching axially/equatorially (α/β of 20/80) can result in chirality in microparticles.

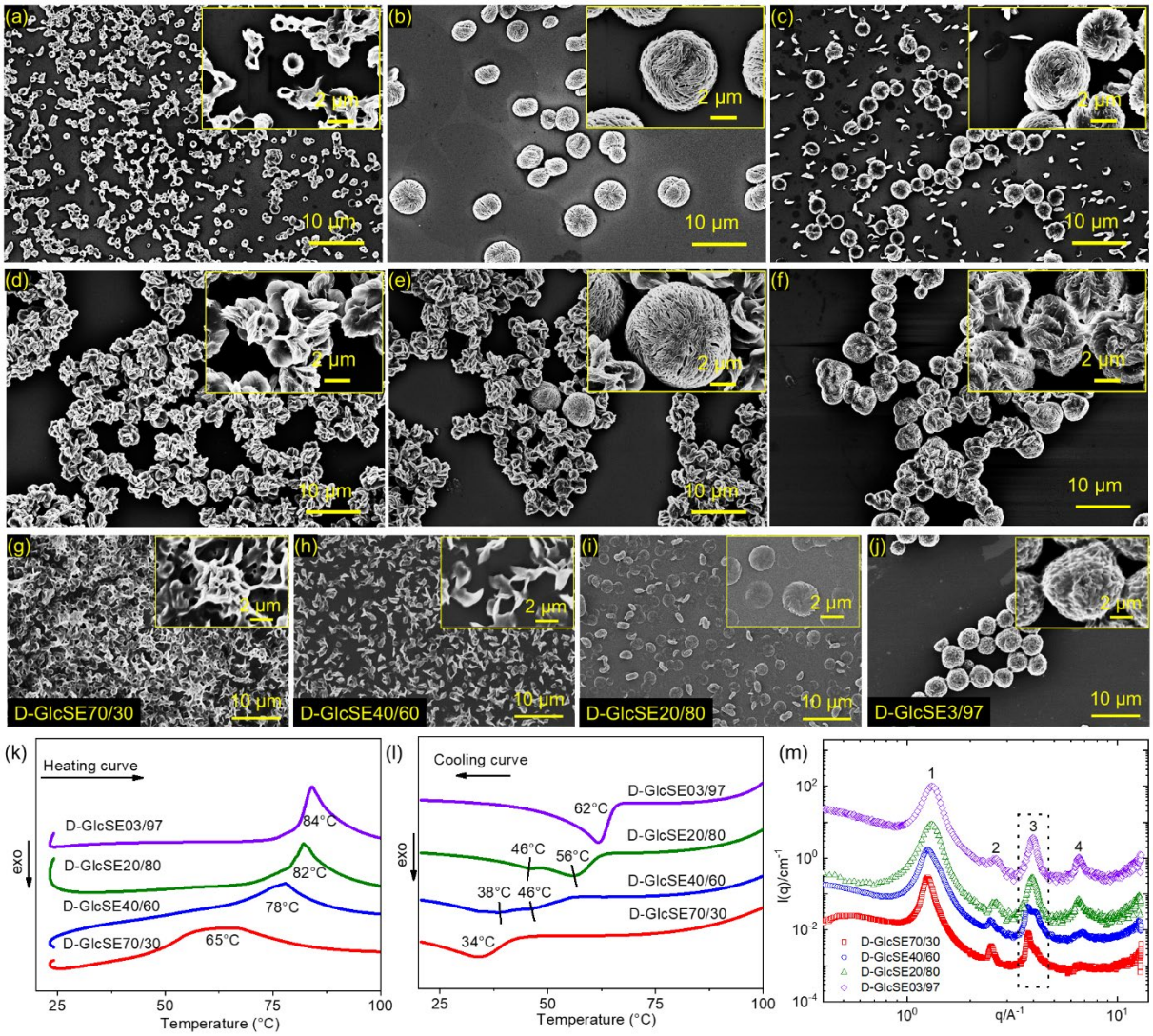

Figure 14. Superstructures from D-GlcSE with diverse ratios of α/β configurations under different conditions and their thermal and crystallization properties. D-GlcSE20/80 prepared with their solutions in ethyl acetate at the concentration of 1 mg/mL. **a-c)** from 60°C to 30°C and **d-f)** from 60°C to 20°C with the cooling rate of 1 °C/min and aged for **a, d)** 0 min, **b, e)** 10 min and **c, f)** 20 min, respectively. **g-j)** SEM images of self-assembled aggregates prepared from D-GlcSE with diverse α/β ratios with the concentration of 1 mg/mL after cooling from 60°C to 25°C with the cooling rate of 1 °C/min and aged at 25°C for 20 min. DSC curves as **k)** heating, and **l)** cooling as well as **m)** SAXS curves of the D-GlcSE with different α/β ratios.

3.3 Role of bond configurations at C2, C4 and C6 in the monosaccharide ring during the formation of porous flower-like microparticles via self-assembly

In addition to the effects of configurations as D/L-configuration and α/β-anomers, the effect of the monosaccharides that contain more structural differences were further studied, as shown in **Publication 3**. In this part, 4 D-monosaccharide stearoyl esters (D-MSSEs), which are D-glucose stearoyl esters (D-GlcSE), D-xylose stearoyl esters (D-XylSE), D-galactose stearoyl esters (D-GalSE) and D-mannose stearoyl ester (D-ManSE), were synthesized and compared (**Figure 15**). Based on the ^{1}H NMR spectra, the α/β ratios at C1 for D-GlcSE, D-XylSE, D-GalSE and D-ManSE are 20/80, 15/85, 27/73 and 35/65, respectively. Thus, these 4 MSSE are named as D-GlcSE20/80, D-XylSE15/85, D-GalSE27/73 and D-ManSE35/65.

All D-MSSE solutions in ethyl acetate of 10 mg/ml were analyzed using dynamic light scattering (DLS) by recording the results with 5°C interval during the temperature decrease from 80°C to 10°C to detect the initial particle formation of each D-MSSE. Between 80 and 60°C, the DLS measurements of the solutions showed no signals, indicating the full dissolution of D-MSSE molecules. DLS signals emerged at 55°C for the solutions of all four D-MSSEs (**Figure 15**) and one can clearly see the peaks representing a length scale of around 100 nm. These peaks indicate the formation of initial, dense liquid droplets, which are metastable with respect to the low-concentration solutions and also the crystalline solids. With steady temperature decrease before the precipitation temperature, these droplets maintained their sizes for all D-MSSEs in their solutions. Once the temperature is lower than the precipitation temperature, e.g., at 25°C for D-GlcSE solution (**Figure 15a**), DLS curves show the formation of structures of a few microns. Such precipitation temperatures vary and lie at 15°C for D-GalSE (**Figure 15c**) and D-ManSE (**Figure 15d**). In comparison, D-XylSE microparticles exhibited solid properties by precipitating at around 31°C, instead of forming flakes and thus cloudy suspension according to their photo images in solutions (**Figure 15b**). These different precipitation temperatures can be attributed to the different solubility of D-MSSE molecules in solutions, distinct densities of dense droplets and growth rates of the crystalline nuclei within the droplets, which are chiefly dictated by their molecular configurations.

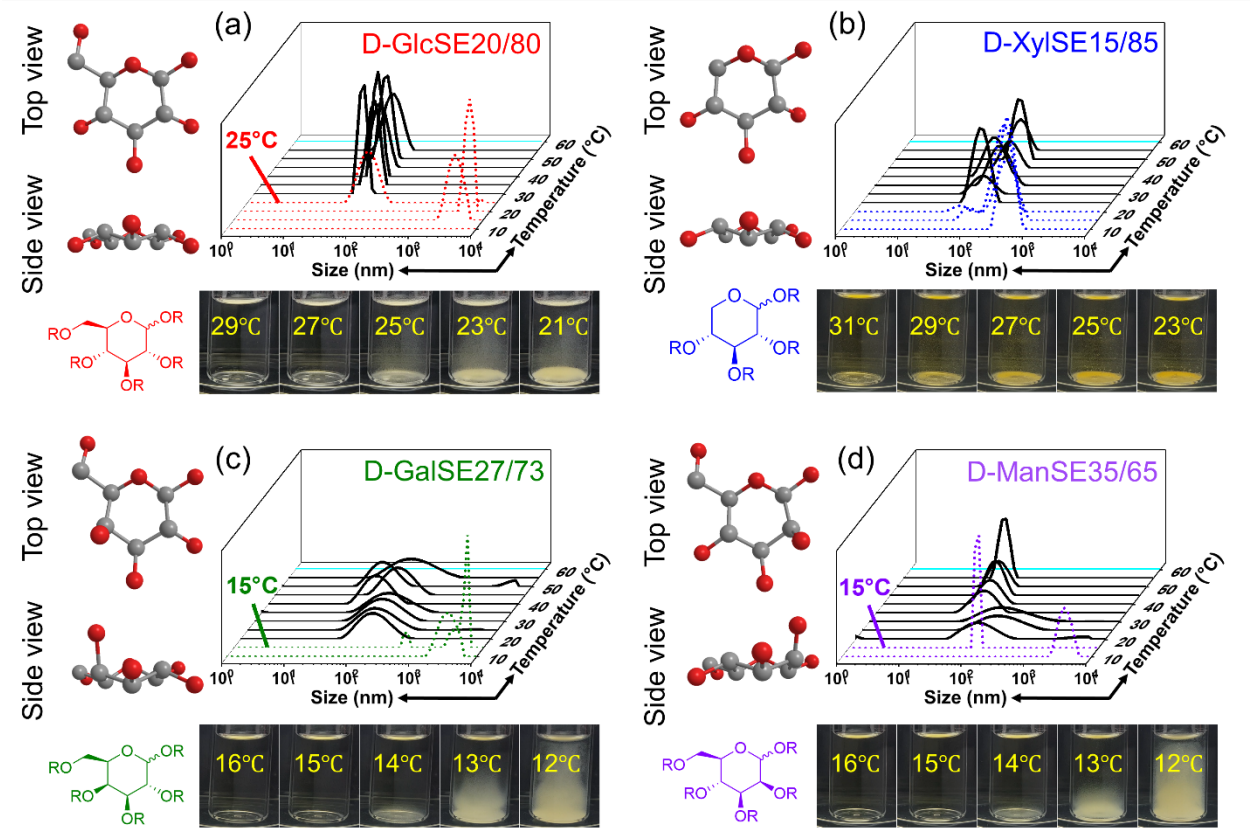

Figure 15. Structural information, DLS and photos during precipitation of stearoyl esters of diverse D-monosaccharides: a) D-GlcSE20/80, b) D-XylSE15/85, c) D-GalSE27/73 and d) D-ManSE35/65. Stereo-structures of D-β-glucose, D-β-xylose, D-β-galactose and D-β-mannose are shown in the top and side views; Structural formula of D-GlcSE20/80, D-XylSE15/85, D-GalSE27/73 and D-ManSE35/65 are shown in Haworth projection; DLS curves were recorded every 5°C in ethyl acetate at 10 mg/mL during the cooling process of 1 °C/min. The bottom images in each panel show the photos of the solutions at various temperatures.

Figure 16 shows the SEM images of the 4 types of microparticles prepared from D-GlcSE20/80, D-XylSE15/85, D-GalSE27/73 and D-ManSE35/65. All D-XylSE15/85, D-GalSE27/73 and D-ManSE35/65 cannot form chiral microparticles under the same condition as preparing chiral microparticles by D-GlcSE20/80. However, all of these 4 types of microparticles show complete round shapes with morphological differences, when prepared with the concentration of 10 mg/mL and cooling rate of 1 °C/min from 60°C to 10°C and aged the solutions at 10°C for 2 h.

D-GlcSE20/80 microparticles show plump particles with draped connections among microparticles, while D-XylSE15/85 microparticles exhibit independent plump and coarse microparticles, as shown in **Figure 16**. Moreover, D-GalSE27/73 and D-ManSE35/65 show similar flower-like microparticles like dahlia. Petal structures with the thickness of 170±100 nm can be calculated for all flower-like microparticles. The diameters of D-GlcSE20/80 microparticles are between 5 and 20 μm, while D-XylSE15/85 microparticles show bigger sizes between 18 and 40 μm. The particle sizes of D-GalSE27/73 (10~40 μm) and D-ManSE35/65 (8~40 μm) are similar in a wider range. Furthermore, the other faster cooling rate of 30 °C/min and the other longer aging time of 24 h were studied to compare the formation differences and understand the formation process. In particular, the microparticles formed from D-GalSE27/73 and D-ManSE35/65 show flower-like superstructures at both low and high cooling rates and both aging time of 2 h and 24 h. In contrast, D-GlcSE20/80 and D-XylSE15/85 molecules only form filled microparticles at low cooling rate for 2 h or high cooling rate for 24 h, while flower-like and draped morphology can be obtained at higher cooling rates for 2 h from D-GlcSE20/80 and D-XylSE15/85, respectively. In addition, higher cooling rate can result in smaller microparticle size, while bigger microparticle size is beneficial from longer aging time.

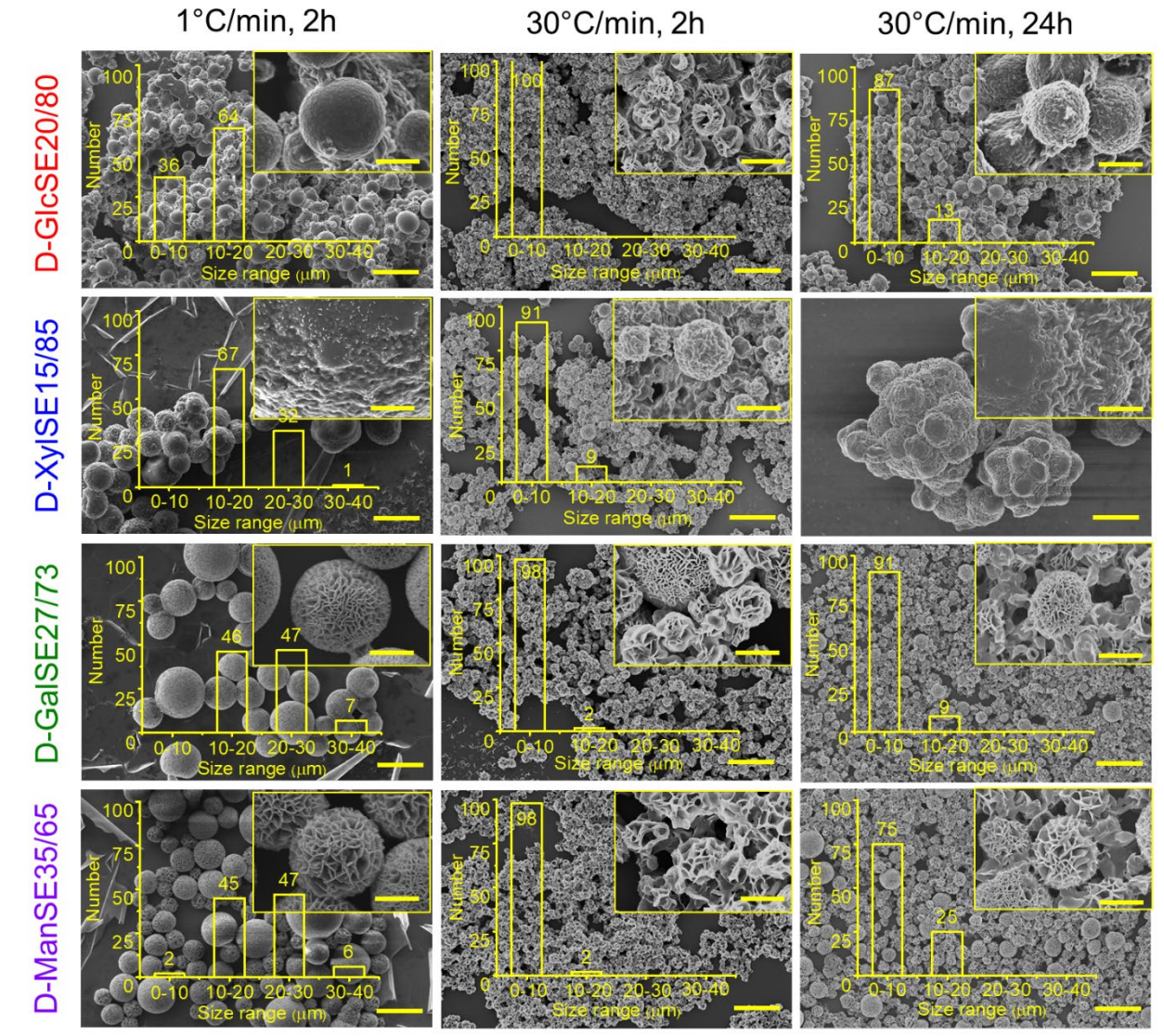

Figure 16. Morphology and size distribution of microparticles prepared from 4 D-MSSEs. SEM images of D-GlcSE20/80, D-XylSE15/85, D-GalSE27/73 and D-ManSE35/65 microparticles obtained from 60°C to 10°C in ethyl acetate with the concentration of 10 g/ml. The cooling rates of 1 °C/min, aged for 2 h; 30 °C/min, aged for 2 h and 30 °C/min, aged for 24 h were compared. The inset SEM images show the enlarged microparticles. The yellow figures show the size distributions of microparticles, with each measured from 100 independent samples. The scale bars in main panels represent 30 μm, while scale bars in the insets are 5 μm.

These distinct D-MSSE microparticles were further analyzed by employing DSC, SAXS, XRD, as well as molecular simulations, to understand their thermal, crystallization and structural properties. **Figure 17a**

illustrates the DSC curves of D-MSSE microparticles, where the heating curve of D-XylSE15/85 microparticles demonstrates a melting temperature T_m of 93°C, which is the largest among 81°C for D-GlcSE20/80, 60°C for D-GalSE27/73, and 63°C for D-ManSE35/65 microparticles. The cooling curves exhibit the crystallization temperatures T_c of the D-MSSE samples and show a similar trend: D-XylSE15/85 exhibit the highest T_c of 63°C, followed by the 55°C for D-GlcSE20/80, 47°C for D-GalSE27/73, and 49°C for D-ManSE35/65 microparticles.

To clearly demonstrate the relationship between molecular structures of D-MSSE molecules and their crystallization properties, we employed computer simulations to calculate the average crystallinity of distinct D-MSSE molecules (**Figure 17b**). It is clear that the average crystallinity of the D-XylSE is larger than that of the D-GlcSE and D-GalSE, indicating that D-XylSE is easier to crystallize than other D-MSSE molecules at the same conditions. This is consistent with the DSC results in **Figure 17a**, where the D-XylSE15/85 takes the highest melting and crystallization temperatures. However, given the obvious differences of thermal properties between microparticles of D-GlcSE20/80 and D-GalSE27/73 (**Figure 17a**), their crystallinities calculated from simulations are closer to each other. To explore the origins of the discrepancies, we measured the crystallinities of the core monomers for sugar rings (see the bottom panel in **Figure 17b**). Results show that the core monomers of D-GlcSE molecules are easier to crystallize than that of D-GalSE molecules.

To further explore the crystallization properties of D-MSSE microparticles, we employed SAXS and XRD methods to measure the powder samples of D-MSSE microparticles. As shown in **Figure 17c**, all D-MSSE microparticles exhibit similar SAXS patterns, showing a q^{-4} scaling law for $q<0.1$ Å^{-1} as expected due to the large dimension of the micrometersized particles (Porod's law). The q^{-2} behavior for $q>0.1$ Å^{-1} hints to the existence of a two-dimensional substructure inside the object. The corresponding Bragg peaks show the semi-crystalline nature of the samples in the two-dimensional substructure. The sharpness of the peaks is most pronounced for D-XylSE15/85, compared to other D-MSSEs. XRD data for the D-MSSEs is given in **Figure 17d**. The packing of neighboring aliphatic chains forming crystallites reflects in the range of 2Θ=18-26°, where the D-MSSEs exhibit differences in the number of distinct peaks: D-XylSE15/85 (4 well defined peaks, 4.5-3.8 Å), D-GlcSE20/80 (broad peak with a shoulder, 4.2-3.8 Å) and D-GalSE27/73 and D-ManSE35/65 (both with 1 peak, 4.1-4.2 Å). The largest peak area of D-XylSE15/85 indicates the best crystalline ability, which is consistent with the DSC measurements and simulation calculations. It can be calculated that in the total 5 side chains in D-GlcSE20/80, 4.8 side chains stretch equatorially and only 0.2 side chains stretch axially (96% equatorially from C1). For D-XylSE15/85 (4 side chains), 3.85 equatorially, 0.15 axially (96.25% equatorially from C1); for D-GalSE27/73 (5 side chains), 3.73 equatorially, 1.27 axially (74.6% equatorially from C1 and C4) and for

D-ManSE35/65 (5 side chains), 3.65 equatorially, 1.35 axially (73% equatorially from C1 and C2). In comparison of D-GlcSE20/80 and D-XylSE15/85, the ratio of the bonds stretching axially/equatorially is similar. The only difference locates at the number of side chains. To compare D-GlcSE20/80, D-GalSE27/73 and D-ManSE35/65, all of them stretch 5 bonds to the side with the only difference in the ratio of bonds stretching axially/equatorially. D-GalSE27/73 (25.4%) and D-ManSE35/65 (27%) have similar and the most number of side chains stretched axially, while D-GlcSE20/80 has only 4% side chains stretched axially. The thermal and crystallization properties are the best for D-XylSE, while worse for D-GlcSE prove fewer side chains working positively for microparticles with better thermal and crystallization properties. The analogous heating and cooling curves with the lowest T_m and T_c of the D-GalSE and D-ManSE microparticles indicate that the position of the axially protruding bonds (whether at C2 or C4) on sugar rings of D-mannose or D-galactose do not strongly influence their thermal and crystalline properties. However, more bonds stretching axially significantly reduces their feasibility to crystallize and thus leads to their lowest T_m and T_c, compared to D-GlcSE and D-XylSE.

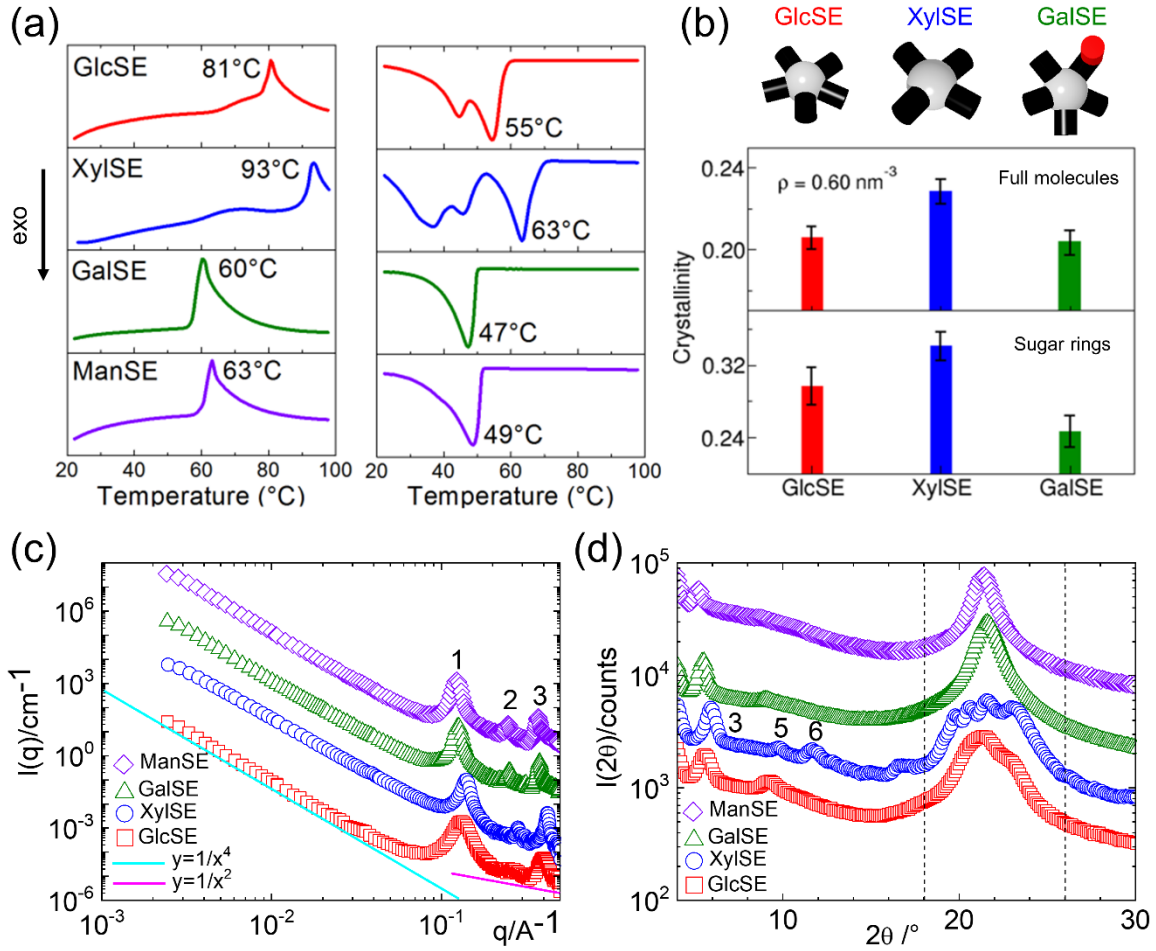

Figure 17. Characterization of the microparticles from various MSSEs and simulations. a) Heating (left) and cooling (right) DSC curves of D-GlcSE20/80, D-XylSE15/85, D-GalSE27/73 and D-ManSE35/65 microparticles obtained from ethyl acetate at the concentration of 1 mg/mL from 60°C to 10°C with the cooling rate of 1 °C/min and aged at 10°C for 2 h. **b)** Top panel: The coarse-grained structures of D-GlcSE, D-XylSE and D-GalSE molecules in simulation, where the stearoyl chains are not shown. Bottom panel: average crystallinity of melts of 3 MSSE molecules and sugar-rings from simulations. **c)** SAXS and **d)** XRD measurements of D-GlcSE20/80, D-XylSE15/85, D-GalSE27/73 and D-ManSE35/65 microparticles.

4. General conclusion and perspectives

As mentioned all along this study, I systematically introduced the different roles of backbones and side chains during the self-assembly and application of carbohydrate stearoyl esters.

Firstly, in **Publication 1**, I studied the anti-fungal effects of hydrophobic and superhydrophobic coatings on wood by using cellulose stearoyl ester (CSE) and glycerol stearoyl ester (GSE). After dip-coating, CSE can form a hydrophobic membrane on the surface of wood due to the high degree of polymerization (DP) in the backbone and the fully esterified long aliphatic side chains. After brush-coating, GSE can form coarse and highly-textured cellular structure, which leads to the ability to extensively trap air between water droplets and wood surfaces. This can be explained by the monomer of glycerol and the fully esterified long aliphatic side chains. Anti-fungal tests further showed the beneficial properties of the hydrophobic and superhydrophobic treatment for the anti-fungal properties. Untreated wood was attacked by fungi severely, both at the surface and in the interior, while hydrophobic and superhydrophobic wood showed better anti-fungal properties. Comparing hydrophobic with superhydrophobic wood, significant anti-fungal properties by maintaining their clean and clear wood structures could only be maintained by SHB/SHP. This could be explained by the synergistic effect of hydrophobic membrane formed by CSE and hierarchical structure on wood surface caused by GSE. Thus, I provided here an efficient method containing two coating steps with pure organic compounds for the surface coating, wood protection, and construction of nanostructures on wood substrates.

Then, in **Publication 2**, I demonstrated the formation of left- and right-handed chiral microparticles induced by D- and L-GlcSE, respectively. The formation of microparticles with chirality can only be achieved when the α/β ratio at C1 in D/L-GlcSE is 20/80, the concentration is 1 mg/mL from 60°C to 25°C with the aging time of 20 min. The α configuration leads to irregular aggregates, which show worse thermal and crystallization properties, while mature round smooth microparticles with better thermal and crystallization properties are beneficial from β configuration. Axially stretched α configuration improves the difficulties of stacking of D-MSSE molecules during self-assembly, while better stacking is beneficial from equatorially stretched β configuration. Furthermore, longer aging time can promote the formation of complete

and mature microparticles. Besides, aging at 30°C facilitates the nucleation of the ring-shaped growing center, while aging at 20°C may lead to the extra degree of super-cooing and dominate the formation of petal-shaped units.

Finally, in **Publication 3**, I introduced the formation of porous flower-like microparticles (FLP) using D-MSSEs and the function of the bond configurations in the monosaccharide ring during the formation of these microparticles. I demonstrated via experiments and simulations that the configurational difference of the bonds connecting the side chains to monosaccharide rings strongly affected the formation of FLP, the surface morphologies of the obtained microparticles and their thermal and structural properties. By choosing monosaccharides including D-glucose, D-xylose, D-galactose and D-mannose, 4 types of microparticles with different precipitation temperatures, morphologies, thermal and crystallization properties can be obtained. The difference regarding these properties should be primarily due to two different origins: number of sidechains and number of bonds stretched axially. More sidechains lead to lower precipitation temperature, worse thermal and crystallization properties. With the same side chains, axially instead of equatorially stretched bond configuration results in lower precipitation temperature, worse thermal and crystallization properties. This conclusion can be explained by the increased obstacles during the stacking of molecules from more side chains and more bonds stretched axially.

Thus, combine **Publication 2 and 3**, both the number of side chains and the number of bonds stretching axially/equatorially at C1, C2 and C4 play the pivotal rules when tuning the sugar-based superstructures from solid to chiral and porous morphology. Microparticles with solid morphology can be easily obtained from D-XylSE15/85 due to the only 4 side chains. In D-GlcSE20/80, the 5 side chains, proper aging time and proper amount of axially stretched bonds endow with the rearrangement of the molecules during self-assembly. Then, this rearrangement leads to the bending of petals and later results in the formation of chiral microparticles. Besides, when with 5 side chains and more bonds stretching axially like D-GalSE27/73 and D-ManSE35/65, porous flower-like microparticles with worse thermal and crystallization properties can be easily obtained because of the more obstacles during self-assembly induced by the bond configuration.

In conclusion, to the best of my knowledge, this is the first time that chiral and porous flower-like microparticles are reported from monosaccharide-based materials and also the first report of tuning the superstructures with solid, chiral or porous flower-like morphologies by only adapting the bond configuration without using external stimuli. Besides, I also provide a method for the preparation of anti-fungal wood induced by hydrophobicity and superhydrophobicity as an application of carbohydrate esters. Thus, my results provide new ideas and methods to design and control the superstructures with diverse morphologies. These findings can facilitate the future study and application of superstructures from carbohydrate esters, especially those with solid, chiral and flower-like morphology under certain needs.

5. References

1 Suhail, M. A novel projection for anomers of glucose. *Chemistry International* **6**, 301-304 (2020).

2 Allen, D. K. & Tao, B. Y. Carbohydrate-alkyl ester derivatives as biosurfactants. *Journal of Surfactants and Detergents* **2**, 383-390 (1999).

3 Lichtenthaler, F. W. Carbohydrates as organic raw materials. *Ullmann's Encyclopedia of Industrial Chemistry* (2000).

4 Lichtenthaler, F. W. & Peters, S. Carbohydrates as green raw materials for the chemical industry. *Comptes Rendus Chimie* **7**, 65-90, doi:https://doi.org/10.1016/j.crci.2004.02.002 (2004).

5 Bezbradica, D. *et al.* Enzymatic syntheses of esters-Green chemistry for valuable food, fuel and fine chemicals. *Current Organic Chemistry* **21**, 104-138 (2017).

6 Neta, N. S., Teixeira, J. A. & Rodrigues, L. R. Sugar ester surfactants: Enzymatic synthesis and applications in food industry. *Critical reviews in food science and nutrition* **55**, 595-610 (2015).

7 Ferrer, M. *et al.* Comparative surface activities of di-and trisaccharide fatty acid esters. *Langmuir* **18**, 667-673 (2002).

8 Kjellin, M. & Johansson, I. *Surfactants from renewable resources*. (John Wiley & Sons, 2010).

9 Fouda, A., Abd El-Maksoud, S. A., El-Habab, A. & Ibrahim, A. R. Synthesis and characterization of new ethoxylated carbohydrate based surfactants for corrosion inhibition of low LCS steel in aqueous solutions. *Biointerface Res Appl Chem* **119**, 9382-9404 (2021).

10 Tharanathan, R. N. Food-derived carbohydrates—structural complexity and functional diversity. *Critical reviews in biotechnology* **22**, 65-84 (2002).

11 Onyango, C., Unbehend, G. & Lindhauer, M. G. Effect of cellulose-derivatives and emulsifiers on creep-recovery and crumb properties of gluten-free bread prepared from sorghum and gelatinised cassava starch. *Food Research International* **42**, 949-955 (2009).

12 Cao, Y. & Ikeda, I. Antioxidant activity and antitumor activity (in vitro) of xyloglucan selenious ester and surfated xyloglucan. *International Journal of Biological Macromolecules* **45**, 231-235 (2009).

13 NISHIKAWA, Y., OKABE, M., YOSHIMOTO, K., KURONO, G. & FUKUOKA, F. Chemical and biochemical studies on carbohydrate esters. II. Antitumor activity of saturated fatty acids and their ester derivatives against Ehrlich ascites carcinoma. *Chemical and Pharmaceutical Bulletin* **24**, 387-393 (1976).

14 NISHIKAWA, Y., YOSHIMOTO, K., OKABE, M. & FUKUOKA, F. Chemical and biochemical studies on carbohydrate esters. III. Antitumor activity of unsaturated fatty acids and their ester derivatives against Ehrlich ascites carcinoma. *Chemical and Pharmaceutical Bulletin* **24**, 756-762 (1976).

15 NISHIKAWA, Y., YOSHIMOTO, K., NISHIJIMA, M., FUKUOKA, F. & IKEKAWA, T. Chemical and biochemical studies on carbohydrate esters. IX. Antitumor effects of selectively fatty acylated products of maltose. *Chemical and Pharmaceutical Bulletin* **29**, 505-513 (1981).

16 IKEKAWA, T., UMEJI, M., YANOMA, S., YOSHIMOTO, K. & NISHIKAWA, Y. Chemical and biochemical studies on carbohydrate esters. VIII. Antitumor activity of sucrose fatty acid esters. *Chemical and Pharmaceutical Bulletin* **27**, 2016-2020 (1979).

17 Watanabe, T., Katayama, S., Matsubara, M., Honda, Y. & Kuwahara, M. Antibacterial carbohydrate monoesters suppressing cell growth of Streptococcus mutans in the presence of sucrose. *Current microbiology* **41**, 210-213 (2000).

18 NISHIKAWA, Y., YOSHIMOTO, K. & OHKAWA, M. Chemical and Biochemical Studies on Carbohydrate Esters. X. Plant Growth Inhibition by Pure Anomers of Synthetic 1-O-Lauroyl-D-glucopyranose. *Chemical and Pharmaceutical Bulletin* **29**, 878-880 (1981).

19 NISHIKAWA, Y., YOSHIMOTO, K. & OHKAWA, M. Chemical and Biochemical Studies on Carbohydrate Esters. VII. Plant Growth Inhibition by an Anomeric Mixture of Synthetic 1-O-Lauroyl-D-glucose. *Chemical and Pharmaceutical Bulletin* **27**, 2011-2015 (1979).

20 Habulin, M., Šabeder, S. & Knez, Ž. Enzymatic synthesis of sugar fatty acid esters in organic solvent and in supercritical carbon dioxide and their antimicrobial activity. *The*

Journal of Supercritical Fluids **45**, 338-345, doi:https://doi.org/10.1016/j.supflu.2008.01.002 (2008).

21 AlFindee, M. N. *et al.* One-step synthesis of carbohydrate esters as antibacterial and antifungal agents. *Bioorganic & medicinal chemistry* **26**, 765-774 (2018).

22 Ferrer, M. *et al.* Synthesis of sugar esters in solvent mixtures by lipases from Thermomyces lanuginosus and Candida antarctica B, and their antimicrobial properties. *Enzyme and Microbial Technology* **36**, 391-398 (2005).

23 Nobmann, P., Bourke, P., Dunne, J. & Henehan, G. In vitro antimicrobial activity and mechanism of action of novel carbohydrate fatty acid derivatives against Staphylococcus aureus and MRSA. *Journal of applied microbiology* **108**, 2152-2161 (2010).

24 Iglauer, S., Wu, Y., Shuler, P., Tang, Y. & Goddard III, W. A. Alkyl polyglycoside surfactant–alcohol cosolvent formulations for improved oil recovery. *Colloids and Surfaces A: Physicochemical and Engineering Aspects* **339**, 48-59 (2009).

25 Fahmy, N. M. & Dahi, H. F. Changes in detoxifying enzymes and carbohydrate metabolism associated with spinetoram in two field-collected strains of Spodoptera littoralis (Biosd.). *Egyptian Academic Journal of Biological Sciences, F. Toxicology & Pest Control* **1**, 17-26 (2009).

26 Zhu, Z. *et al.* Regio-and Stereo-selective Synthesis of Peracetylated Carbohydrate Esters of Aromatic Fatty Acid Using p-Toluenesulfonic Acid as Catalyst. *Chinese Journal of Chemistry* **28**, 2245-2248 (2010).

27 Lee, D. & Taylor, M. S. Borinic acid-catalyzed regioselective acylation of carbohydrate derivatives. *Journal of the American Chemical Society* **133**, 3724-3727 (2011).

28 Winkler, H., Vorwerg, W. & Wetzel, H. Synthesis and properties of fatty acid starch esters. *Carbohydrate polymers* **98**, 208-216 (2013).

29 Nguyen, P. C. *et al.* A novel maltoheptaose-based sugar ester having excellent emulsifying properties and optimization of its lipase-catalyzed synthesis. *Food Chemistry* **352**, 129358 (2021).

30 Siebenhaller, S. *et al.* Lipase-catalyzed synthesis of sugar esters in honey and agave syrup. *Frontiers in chemistry* **6**, 24 (2018).

31 Gérard, D. *et al.* Enzymatically-synthesized xylo-oligosaccharides laurate esters as surfactants of interest. *Carbohydrate Research* **495**, 108090 (2020).

32 Adkins, H. & Thompson, Q. E. Diacylation of Water and of Hydrogen Sulfide with Acyl Chloride--Pyridine Compounds. *Journal of the American Chemical Society* **71**, 2242-2244, doi:10.1021/ja01174a090 (1949).

33 Wang, P. & Tao, B. Y. Synthesis and characterization of long-chain fatty acid cellulose ester (FACE). *Journal of applied polymer science* **52**, 755-761 (1994).

34 Wang, P. & Tao, B. Y. Synthesis of cellulose-fatty acid esters for use as biodegradable plastics. *Journal of environmental polymer degradation* **3**, 115-119 (1995).

35 Vaca-Garcia, C., Gozzelino, G., Glasser, W. & Borredon, M.-E. Dynamic mechanical thermal analysis transitions of partially and fully substituted cellulose fatty esters. *Journal of Polymer Science Part B: Polymer Physics* **41**, 281-288 (2003).

36 Otey, F. & Mehltretter, C. Preparation of 3-stearoyl-D-glucose—A bread-softening agent. *Journal of the American Oil Chemists' Society* **35**, 455-457 (1958).

37 Murdzheva, D. *et al.* Microwave-assisted synthesis of methyl esters of alginic acids as potential drug carrier. *International Journal of Pharmaceutical and Clinical Research* **8**, 1361-1368 (2016).

38 Ratanakamnuan, U., Atong, D. & Aht-Ong, D. Cellulose esters from waste cotton fabric via conventional and microwave heating. *Carbohydrate Polymers* **87**, 84-94 (2012).

39 Corsaro, A., Chiacchio, U., Pistara, V. & Romeo, G. Microwave-assisted Chemistry of Carbohydrates. *Current Organic Chemistry* **8**, 511-538, doi:10.2174/1385272043485828 (2004).

40 Muljana, H. *et al.* Synthesis of fatty acid starch esters in supercritical carbon dioxide. *Carbohydrate Polymers* **82**, 346-354, doi:https://doi.org/10.1016/j.carbpol.2010.04.067 (2010).

41 Šabeder, S., Habulin, M. & Knez, Ž. Comparison of the Esterification of Fructose and Palmitic Acid in Organic Solvent and in Supercritical Carbon Dioxide. *Industrial & Engineering Chemistry Research* **44**, 9631-9635, doi:10.1021/ie050266k (2005).

42 Palocci, C., Falconi, M., Chronopoulou, L. & Cernia, E. Lipase-catalyzed regioselective acylation of tritylglycosides in supercritical carbon dioxide. *The Journal of Supercritical Fluids* **45**, 88-93, doi:https://doi.org/10.1016/j.supflu.2007.11.009 (2008).

43 van den Broek, L. A. M. & Boeriu, C. G. Enzymatic synthesis of oligo- and polysaccharide fatty acid esters. *Carbohydrate Polymers* **93**, 65-72, doi:https://doi.org/10.1016/j.carbpol.2012.05.051 (2013).

44 Abdulmalek, E. *et al.* Improved enzymatic galactose oleate ester synthesis in ionic liquids. *Journal of Molecular Catalysis B: Enzymatic* **76**, 37-43, doi:https://doi.org/10.1016/j.molcatb.2011.12.004 (2012).

45 Yang, Z. & Huang, Z.-L. Enzymatic synthesis of sugar fatty acid esters in ionic liquids. *Catalysis Science & Technology* **2**, 1767-1775, doi:10.1039/C2CY20109G (2012).

46 Lee, S. H., Ha, S. H., Hiep, N. M., Chang, W.-J. & Koo, Y.-M. Lipase-catalyzed synthesis of glucose fatty acid ester using ionic liquids mixtures. *Journal of Biotechnology* **133**, 486-489, doi:https://doi.org/10.1016/j.jbiotec.2007.11.001 (2008).

47 Lee, S. H., Nguyen, H. M., Koo, Y.-M. & Ha, S. H. Ultrasound-enhanced lipase activity in the synthesis of sugar ester using ionic liquids. *Process Biochemistry* **43**, 1009-1012, doi:https://doi.org/10.1016/j.procbio.2008.05.001 (2008).

48 Gao, J., Luo, Z.-G. & Luo, F.-X. Ionic liquids as solvents for dissolution of corn starch and homogeneous synthesis of fatty-acid starch esters without catalysts. *Carbohydrate Polymers* **89**, 1215-1221, doi:https://doi.org/10.1016/j.carbpol.2012.03.096 (2012).

49 Kennedy, J. F. *et al.* Enzyme-catalyzed regioselective synthesis of sugar esters and related compounds. *Journal of Chemical Technology & Biotechnology: International Research in Process, Environmental & Clean Technology* **81**, 866-876 (2006).

50 Shi, Y. g., Li, J. r. & Chu, Y. H. Enzyme-catalyzed regioselective synthesis of sucrose-based esters. *Journal of Chemical Technology & Biotechnology* **86**, 1457-1468 (2011).

51 Chakraborty, S., Sahoo, B., Teraoka, I., Miller, L. M. & Gross, R. A. Enzyme-catalyzed regioselective modification of starch nanoparticles. *Macromolecules* **38**, 61-68 (2005).

52 Patil, P. S., Lee, C.-C., Huang, Y.-W., Zulueta, M. M. L. & Hung, S.-C. Regioselective and stereoselective benzylidene installation and one-pot protection of D-mannose. *Organic & biomolecular chemistry* **11**, 2605-2612 (2013).

53 Riva, S. Exploiting enzyme chemoselectivity and regioselectivity. *Organic Synthesis with Enzymes in Non-Aqueous Media*, 145-167 (2008).

54 Chang, S. W. & Shaw, J. F. Biocatalysis for the production of carbohydrate esters. *New Biotechnology* **26**, 109-116 (2009).

55 Ganske, F. & Bornscheuer, U. T. Lipase-catalyzed glucose fatty acid ester synthesis in ionic liquids. *Organic Letters* **7**, 3097-3098 (2005).

56 Gumel, A., Annuar, M., Heidelberg, T. & Chisti, Y. Lipase mediated synthesis of sugar fatty acid esters. *Process Biochemistry* **46**, 2079-2090 (2011).

57 Ren, K. & Lamsal, B. P. Synthesis of some glucose-fatty acid esters by lipase from Candida antarctica and their emulsion functions. *Food chemistry* **214**, 556-563 (2017).

58 Ignatyev, I., Van Doorslaer, C., Mertens, P., Binnemans, K. & De Vos, D. Synthesis of glucose esters from cellulose in ionic liquids. *Holzforschung* **66**, 417-425 (2012).

59 Lakeev, S., Maydanova, I., Mullakhmetov, R. & Davydova, O. Ester plasticizers for polyvinyl chloride. *Russian Journal of Applied Chemistry* **89**, 1-15 (2016).

60 Bocqué, M., Voirin, C., Lapinte, V., Caillol, S. & Robin, J. J. Petro-based and bio-based plasticizers: Chemical structures to plasticizing properties. *Journal of Polymer Science Part A: Polymer Chemistry* **54**, 11-33 (2016).

61 Howell, B. A. & Lazar, S. T. Biobased Plasticizers from Carbohydrate-Derived 2,5-Bis(hydroxymethyl)furan. *Industrial & Engineering Chemistry Research* **58**, 1222-1228, doi:10.1021/acs.iecr.8b05442 (2019).

62 Vassilev, D., Petkova, N., Koleva, M. & Denev, P. Ultrasound-Assisted Synthesis of Sucrose and Fructooligosaccharides Esters as Bio-Plasticizers. *Journal of Renewable Materials* **4**, 24-30, doi:10.7569/JRM.2015.634125 (2016).

63 Yin, B., Aminlashgari, N., Yang, X. & Hakkarainen, M. Glucose esters as biobased PVC plasticizers. *European Polymer Journal* **58**, 34-40, doi:https://doi.org/10.1016/j.eurpolymj.2014.06.008 (2014).

64 Wang, P. & Tao, B. Y. in *Biopolymers* Vol. 723 *ACS Symposium Series* Ch. 6, 77-87 (American Chemical Society, 1999).

65 Crépy, L., Miri, V., Joly, N., Martin, P. & Lefebvre, J.-M. Effect of side chain length on structure and thermomechanical properties of fully substituted cellulose fatty esters. *Carbohydrate polymers* **83**, 1812-1820 (2011).

66 Crépy, L., Chaveriat, L., Banoub, J., Martin, P. & Joly, N. Synthesis of cellulose fatty esters as plastics—influence of the degree of substitution and the fatty chain length on

mechanical properties. *ChemSusChem: Chemistry & Sustainability Energy & Materials* **2**, 165-170 (2009).

67 Chen, X., Zheng, N., Wang, Q., Liu, L. & Men, Y. Side-chain crystallization in alkyl-substituted cellulose esters and hydroxypropyl cellulose esters. *Carbohydrate polymers* **162**, 28-34 (2017).

68 Danjo, T. & Iwata, T. Syntheses of cellulose branched ester derivatives and their properties and structure analyses. *Polymer* **137**, 358-363 (2018).

69 Willberg-Keyriläinen, P., Vartiainen, J., Harlin, A. & Ropponen, J. The effect of side-chain length of cellulose fatty acid esters on their thermal, barrier and mechanical properties. *Cellulose* **24**, 505-517 (2017).

70 Nishio, Y., Matsuda, K., Miyashita, Y., Kimura, N. & Suzuki, H. Blends of poly (∈-caprolactone) with cellulose alkyl esters: effect of the alkyl side-chain length and degree of substitu tion on miscibility. *Cellulose* **4**, 131-145 (1997).

71 Samuel, A. Z. *et al.* Determination of percent crystallinity of side-chain crystallized Alkylated-Dextran derivatives with Raman spectroscopy and multivariate curve resolution. *Analytical chemistry* **88**, 4644-4650 (2016).

72 Vanmarcke, A. *et al.* Influence of fatty chain length and starch composition on structure and properties of fully substituted fatty acid starch esters. *Carbohydrate polymers* **164**, 249-257 (2017).

73 Zhai, W., Danjo, T. & Iwata, T. Synthesis and physical properties of Curdlan branched Ester derivatives. *Journal of Polymer Research* **25**, 1-7 (2018).

74 Gan, H. *et al.* Synthesis, properties and molecular conformation of paramylon ester derivatives. *Polymer Degradation and Stability* **145**, 142-149 (2017).

75 Shibakami, M. & Sohma, M. Thermal, crystalline, and pressure-sensitive adhesive properties of paramylon monoesters derived from an euglenoid polysaccharide. *Carbohydrate polymers* **200**, 239-247 (2018).

76 Puanglek, S., Kimura, S. & Iwata, T. Thermal and mechanical properties of tailor-made unbranched α-1, 3-glucan esters with various carboxylic acid chain length. *Carbohydrate polymers* **169**, 245-254 (2017).

77 Tournier, V. *et al.* An engineered PET depolymerase to break down and recycle plastic bottles. *Nature* **580**, 216-219 (2020).

78 Incarnato, L., Scarfato, P., Di Maio, L. & Acierno, D. Structure and rheology of recycled PET modified by reactive extrusion. *Polymer* **41**, 6825-6831, doi:https://doi.org/10.1016/S0032-3861(00)00032-X (2000).

79 Sun, Z., Jiang, Z. & Qiu, Z. Thermal, crystallization and mechanical properties of branched Poly (butylene succinate) copolymers with 1, 2-decanediol being the comonomer. *Polymer* **213**, 123197 (2021).

80 Zia, Q. *et al.* Porous poly (L–lactic acid)/chitosan nanofibres for copper ion adsorption. *Carbohydrate polymers* **227**, 115343 (2020).

81 Yokohara, T. & Yamaguchi, M. Structure and properties for biomass-based polyester blends of PLA and PBS. *European Polymer Journal* **44**, 677-685, doi:https://doi.org/10.1016/j.eurpolymj.2008.01.008 (2008).

82 Permanasari, A., Yulistiani, F., Purnama, R., Widjaja, T. & Gunawan, S. in *IOP Conference Series: Earth and Environmental Science.* 012002 (IOP Publishing).

83 Flood, A. E. & Srisanga, S. An improved model of the seeded batch crystallization of glucose monohydrate from aqueous solutions. *Journal of Food Engineering* **109**, 209-217, doi:https://doi.org/10.1016/j.jfoodeng.2011.09.035 (2012).

84 Schmidt-Lassen, J. & Lindhorst, T. K. Exploring the meaning of sugar configuration in a supramolecular environment: comparison of six octyl glycoside micelles by ITC and NMR spectroscopy. *MedChemComm* **5**, 1218-1226, doi:10.1039/C4MD00122B (2014).

85 Kadokawa, J.-i., Shoji, T. & Yamamoto, K. Preparation of Amylose-Carboxymethyl Cellulose Conjugated Supramolecular Networks by Phosphorylase-Catalyzed Enzymatic Polymerization. *Catalysts* **9**, 211 (2019).

86 Sasaki, T. & Miyata, M. Characterization of hidden chirality: two-fold helicity in β-strands. *Symmetry* **11**, 499 (2019).

87 Lee, Y. H. *et al.* Creating two self-assembly micro-environments to achieve supercrystals with dual structures using polyhedral nanoparticles. *Nature communications* **9**, 1-8 (2018).

88 Rorabeck, K. & Zhitomirsky, I. Salting-out aided dispersive extraction of Mn3O4 nanoparticles and carbon nanotubes for application in supercapacitors. *Colloids and Surfaces A: Physicochemical and Engineering Aspects*, 126451 (2021).

89 Liu, Y. *et al.* Stable polymer nanoparticles with exceptionally high drug loading by sequential nanoprecipitation. *Angewandte Chemie* **132**, 4750-4758 (2020).

90 Hosseini-Nassab, N., Samanta, D., Abdolazimi, Y., Annes, J. P. & Zare, R. N. Electrically controlled release of insulin using polypyrrole nanoparticles. *Nanoscale* **9**, 143-149 (2017).

91 Bodmeier, R. Effect of solvent type on preparation of ethyl cellulose microparticles by solvent evaporation method with double emulsion system using focused beam reflectance measurement. *Polymer International* **66**, 1448-1455 (2017).

92 Meirinho, S. *et al.* Salting-out assisted liquid–liquid extraction method optimized by design of experiments for the simultaneous high-performance liquid chromatography analysis of perampanel and stiripentol in mouse matrices. *Journal of Separation Science* **43**, 4289-4304 (2020).

93 Fu, H. *et al.* Effects of salting-out and salting-out extraction on the separation of butyric acid. *Separation and Purification Technology* **180**, 44-50 (2017).

94 Giroud, B. *et al.* Trace-level determination of two neonicotinoid insecticide residues in honey bee royal jelly using ultra-sound assisted salting-out liquid liquid extraction followed by ultra-high-performance liquid chromatography-tandem mass spectrometry. *Microchemical journal* **151**, 104249 (2019).

95 Edgar, K. J. Cellulose esters in drug delivery. *Cellulose* **14**, 49-64 (2007).

96 Pastor, M., Esquisabel, A., Marquínez, I., Talavera, A. & Pedraz, J. L. Cellulose acetate phthalate microparticles containing Vibrio cholerae: steps toward an oral cholera vaccine. *Journal of drug targeting* **22**, 478-487 (2014).

97 Hadef, I., Omri, M., Edwards-Lévy, F. & Bliard, C. Influence of chemically modified alginate esters on the preparation of microparticles by transacylation with protein in W/O emulsions. *Carbohydrate polymers* **157**, 275-281 (2017).

98 Cardea, S. & De Marco, I. Cellulose acetate and supercritical carbon dioxide: Membranes, nanoparticles, microparticles and nanostructured filaments. *Polymers* **12**, 162 (2020).

99 Zhang, K. *et al.* Polymeric Flower-Like Microparticles from Self-Assembled Cellulose Stearoyl Esters. *ACS Macro Letters* **4**, 214-219, doi:10.1021/mz500788e (2015).

100 Wang, Y. *et al.* Polymeric Flaky Nanostructures from Cellulose Stearoyl Esters for Functional Surfaces. *Advanced Materials Interfaces* **3**, 1600636, doi:https://doi.org/10.1002/admi.201600636 (2016).

101 Wang, Y., Zhang, C., Tian, J., Xie, Y. & Zhang, K. A Comparative Study of Self-Assembled Superstructures from Cellulose Stearoyl Ester and Poly(Vinyl Stearate). *Macromolecular Chemistry and Physics* **219**, 1800229, doi:https://doi.org/10.1002/macp.201800229 (2018).

102 Hornig, S. & Heinze, T. Efficient approach to design stable water-dispersible nanoparticles of hydrophobic cellulose esters. *Biomacromolecules* **9**, 1487-1492 (2008).

103 Hornig, S., Heinze, T., Becer, C. R. & Schubert, U. S. Synthetic polymeric nanoparticles by nanoprecipitation. *Journal of materials chemistry* **19**, 3838-3840 (2009).

104 Mazumder, S., Dewangan, A. K. & Pavurala, N. Enhanced dissolution of poorly soluble antiviral drugs from nanoparticles of cellulose acetate based solid dispersion matrices. *asian journal of pharmaceutical sciences* **12**, 532-541 (2017).

105 Nau, M., Seelinger, D. & Biesalski, M. Functional surface coatings from tailor-made long-chain hydroxypropyl cellulose ester nanoparticles. *Cellulose* **25**, 5769-5780 (2018).

106 Geissler, A., Scheid, D., Li, W., Gallei, M. & Zhang, K. Facile formation of stimuli-responsive, fluorescent and magnetic nanoparticles based on cellulose stearoyl ester via nanoprecipitation. *Cellulose* **21**, 4181-4194 (2014).

107 Kulterer, M. R. *et al.* Functional polysaccharide composite nanoparticles from cellulose acetate and potential applications. *Advanced functional materials* **22**, 1749-1758 (2012).

108 Liebert, T., Hornig, S., Hesse, S. & Heinze, T. Nanoparticles on the Basis of Highly Functionalized Dextrans. *Journal of the American Chemical Society* **127**, 10484-10485, doi:10.1021/ja052594h (2005).

109 Hornig, S., Liebert, T. & Heinze, T. Structure Design of Multifunctional Furoate and Pyroglutamate Esters of Dextran by Polymer-Analogous Reactions. *Macromolecular Bioscience* **7**, 297-306, doi:https://doi.org/10.1002/mabi.200600189 (2007).

110 Hornig, S. & Heinze, T. Nanoscale structures of dextran esters. *Carbohydrate Polymers* **68**, 280-286, doi:https://doi.org/10.1016/j.carbpol.2006.12.007 (2007).

111 Petzold-Welcke, K., Schwikal, K., Daus, S. & Heinze, T. Xylan derivatives and their application potential – Mini-review of own results. *Carbohydrate Polymers* **100**, 80-88, doi:https://doi.org/10.1016/j.carbpol.2012.11.052 (2014).

Appendix

Author's peer-reviewed publications

Publication 1

Differential anti-fungal effects from hydrophobic and superhydrophobic wood based on cellulose and glycerol stearoyl esters

Yawen Yao,[1] Antje Gellerich,[2] Michaela Zauner,[2] Xiaoxu Wang,[3] Kai Zhang[1]*

1. Wood Technology and Wood Chemistry, Georg-August-University of Goettingen, Büsgenweg 4, 37077 Göttingen, Germany.

2. Wood Biology and Wood Products, Georg-August-University of Goettingen, Büsgenweg 4, 37077 Göttingen, Germany.

3. College of Biological Sciences and Technology, Beijing Forestry University, Tsinghua East Road 35, 100083 Beijing, PR China.

Corresponding author:

*Email: kzhang1@uni-goettingen.de. Phone: +49551394505. Fax: +49551399646.

Originally published in:

Cellulose

Springer

https://doi.org/10.1007/s10570-017-1626-x

Received: 20 August 2017; Published: 19 December 2017

Abstract: Wood is still a widely used raw material in many fields and is surface-modified for diverse applications. Though a few studies reported the anti-fungal effect derived from enhanced hydrophobicity of wood surface, no report about the influence of superhydrophobic surface upon fungi is known and the comparison of anti-fungal effects between hydrophobicity and superhydrophobicity on wood surface has not been demonstrated. We herein addressed these aspects regarding the anti-fungal properties of both hydrophobic and superhydrophobic wood. Hydrophobic and superhydrophobic beech and pine, representing hard- and softwood were fabricated, using environmentally friendly organic materials (cellulose and glycerol). Cellulose stearoyl ester was used for dip-coating (1st layer) the wood, leading to a hydrophobic surface and glycerol stearoyl ester was used for brush-coating (2nd layer) the wood, leading to a hierarchical superhydrophobic surface. Results showed that hydrophobic and superhydrophobic woods exhibited better anti-fungal properties comparing with non-treated wood. Furthermore, differential anti-fungal effects of hydrophobic and superhydrophobic wood were observed: superhydrophobic wood could thoroughly prevent fungal attachment to treated wood, while fungi could still be found inside hydrophobic wood after anti-fungal test.

Keywords: wood, cellulose stearoyl ester, glycerol stearoyl ester, anti-fungal, superhydrophobic

INTRODUCTION

Wood, which is an important part of people's daily lives, has been used as a construction material for making tools, furniture, papers and weapons for thousands of years due to its extraordinary mechanical and processing properties. However, wood can frequently get damaged due to the attack of mold (Carey 1980, Zabel and Terracina 1980). Hydrophilic wood surfaces combining with absorbed moisture, sufficient air and fat provide favorable environment conditions for the attachment and growth of mold. Following this, diverse types of damage caused by mold have been observed during the use of wood products (Zabel and Terracina 1978, Bravery 1988, Zabel and Morrell 2012).

In order to promote anti-fungal properties, one strategy is to fabricate a water barrier on surface such as hydrophobic and superhydrophobic surfaces. Hydrophobic surface is generally defined as a surface with a static water contact angle (WCA) of more than 90°, while superhydrophobicity is generally defined as a surface with a static water contact angle (WCA) of

over 150° and a sliding angle of less than 10° (Wang and Jiang 2007, Wen, Tian et al. 2015). As far as we know, hydrophobic surfaces are commonly reported anti-fungal barriers. For example, Chen reported there was an optimum hydrophobicity window in which high antimicrobial activity could be obtained (Chen, Guarnieri et al. 2007); Kuroda proved that the antimicrobial activity depended sigmoidally on the mole fraction of hydrophobic groups (Kuroda, Caputo et al. 2009) and Yin reported the roles of hydrophobicity and charge distribution of cationic antimicrobial peptides in peptide-membrane interactions (Yin, Edwards et al. 2012). Furthermore, hydrophobicity resulting from cold plasma treatment also led to decreased microbial adhesion (Guillemot, Despax et al. 2008). In addition, further studies also addressed the advantageous effect of hydrophobicity for the anti-fungal properties of wood. For example, treatment of wood with mDMDHEU resulted in higher hydrophobicity and at the same time greater resistance regarding wood-decay and staining fungi (Xie, Krause et al. 2008). In another study, enhanced decay-resistance of acetylated wood was proved to be due to the lower cell-wall moisture content, so that no fungal attack was possible and thus the initial enzymic attack could not take place (Rowell, Ibach et al. 2009). However, no paper reports the ability of superhydrophobic barrier to promote anti-fungal properties or compares the anti-fungal properties derived from hydrophobicity and superhydrophobicity.

Hydrophobic surfaces on wood have been prepared after simple surface coating using various materials, such as polymers (Raghavan, Riley et al. 1998) and wax (Lesar, Pavlič et al. 2011). Superhydrophobic wood has been fabricated using tetraethoxysilane (TEOS) (Chang, Tu et al. 2015), potassium methyl siliconate (PMS) (Liu, Wang et al. 2011) and inorganic metal oxides, such as ZnO (Wang, Shi et al. 2011) and TiO_2 (Gao, Lu et al. 2015, Liu, Qing et al. 2015). These processes for fabricating superhydrophobic wood surfaces involve the application of organic-inorganic hybrids or inorganic materials onto wood surfaces to form micro/nano hierarchical structures, while the usage of pure organic materials still remains rare. Moreover, to our best knowledge, no comparison of the differential anti-fungal effects between hydrophobic and superhydrophobic coatings on wood has been carried out to explore their distinct functions.

Based on our former research (Geissler, Loyal et al. 2014), bulky and nanostructured cellulose stearoyl ester can be used to fabricate hydrophobic and superhydrophobic surfaces. In this work, we showed a facile method to fabricate hydrophobic and superhydrophobic wood surfaces by using stearoyl esters of cellulose (CSE) and glycerol (GSE), which are inexpensive and

environmentally friendly organic compounds. The stearoyl esters of cellulose and glycerol were prepared after the esterification of microcrystalline cellulose (MCC) and glycerol by using stearoyl chloride. The process of producing superhydrophobic wood includes 2 steps. First, wood samples were dip-coated in CSE solution, leading to the 1st hydrophobic layer. After that, GSE solution was brush-coated onto the obtained hydrophobic layer of the wood, resulting in a superhydrophobic surface (2nd layer). The wood samples with and without surface treatments were subsequently examined regarding their anti-fungal properties and anti-fungal properties between hydrophobic and superhydrophobic woods were compared.

EXPERIMENTAL SECTION

Materials. Wood samples (40 mm×40 mm×5 mm) were obtained from air-dried boards of European beech (*Fagus sylvatica L.*) and Scots pine (*Pinus sylvestris L.*) sapwood. Microcrystalline cellulose (MCC) with an average granule size of 50 µm and stearoyl chloride (90%) were purchased from Sigma-Aldrich (Steinheim, Germany). Glycerol was obtained from J. T. Baker (PA, U.S.A). Dichloromethane (DCM) and ethyl acetate (EA) of analytical grade were purchased from VWR (Darmstadt, Germany). Ethanol (technical) was obtained from Th. Geyer (Hamburg, Germany). Other chemicals were all of analytical grade and used as received without further purification.

Synthesis of cellulose stearoyl esters (CSE) and glycerol stearoyl esters (GSE). CSE was synthesized according to published procedures (Zhang, Geissler et al. 2015). Briefly, 1 g of MCC and 30 mL of pyridine was mixed and heated up to 100°C and 13.83 mL of stearoyl chloride was dropped into the mixture, while the system was purged with nitrogen. After stirring at 100°C for 1 h, the reaction mixture was immediately poured into 300 mL ethanol. The precipitate was separated by centrifugation and purified through multiple washing by dissolution in DCM and precipitation in ethanol. Finally, CSE was obtained after drying. The synthesis of GSE was basically the same as the synthesis of CSE, while 1 g of glycerol, 52.77 mL of pyridine and 21.93 mL of stearoyl chloride were used for the synthesis.

Preparation of hydrophobic and superhydrophobic wood. The preparation of superhydrophobic wood includes two steps, which leads to a two-layer surface as demonstrated in Scheme 1. First, wood samples (named as OB for original beech and OP for original pine)

were washed by deionized water and ethanol under ultrasonic conditions for 10 min and dried under vacuum at 80°C for overnight, leading to washed wood samples (named as WB for washed beech and WP for washed pine). Afterwards, WB and WP samples were dipped into CSE solution of 50 mg/mL in DCM for 10 s and dried for 5 min under ambient conditions. The first layer was formed and the wood became hydrophobic (named as HB for hydrophobic beech and HP for hydrophobic pine). Then, GSE was dissolved into ethyl acetate (EA) with a concentration of 50 mg/mL at 60°C. The GSE solution was brush-coated onto HB/HP and the wood samples were dried for 5 min under ambient conditions. The brushing and drying process was repeated 5 times, until the second layer was formed. The resulting two-layer wood surfaces exhibited superhydrophobic properties (named as SHB for superhydrophobic beech and SHP for superhydrophobic pine).

Characterization. Nuclear magnetic resonance (NMR) was recorded at room temperature on a Bruker DRX 500 spectrometer (Bruker, Biospin GmbH, Ettlingen). Fourier transform infrared spectroscopy (FT-IR) was conducted with an Alpha FTIR Spectrometer (Bruker) at room temperature between 4000 and 600 cm^{-1} with a resolution of 4 cm^{-1}. The samples were measured twice with 32 scans and an average spectrum was then generated for each sample. The carbon and hydrogen content of the samples were analyzed by using an Elemental Analyser vario EL III CHN from Elementar (Hanau, Germany). The total degree of substitution ascribed to stearoyl groups (DS_{SE}) of CSE and the structure of GSE was analyzed using elemental analysis and NMR, according to the published procedures (Vaca-Garcia, Borredon et al. 2001, Van de Velde and Kiekens 2004). The morphology of the prepared wood surfaces was characterized using a LEO Supra-35 high-resolution field emission scanning electron microscope (Carl Zeiss AG, Germany). For this, the sample surface was coated with a 10 nm layer of carbon before SEM measurements. Static contact angles were measured on a contact angle measuring system OCA 15EC (Dataphysics, Germany) and photos were taken after droplets stayed on the wood for 5 s.

Anti-fungal test. All the wood samples, including WB/WP (as positive controls), HB/HP and SHB/SHP were used for anti-fungal test. The test was conducted according to a method adapted from a modified British and European standard test (EN 152, BS 3900-G6) to obtain the most accurate and efficient results for the specimens with hydrophobic and superhydrophobic surfaces. 10 wood samples of each type (WB/WP, HB/HP and SHB/SHP) were used. The nutrient medium was prepared by mixing 7.5 g citric acid, 12 g Malt, 72 mL NaOH (1 M) and

234 mL HCl (0.1 M) and the pH was adjusted to 4.2, which is the optimal conditions for fungal growth. 8 types of mold and staining fungi which are present in environmental atmosphere were used: *Aspergillus versicolor, Aureobasidium pullulans, Cladosporium cladosporioides, Penicillium purpurogenum, Rhodotorula rubra, Sydowia polyspora, Stachybotrys chartarum* and *Ulocladium atrum*. The spore suspension was conditioned at a relative humidity of 70% and 22°C for 5 days for fungal growth before use. The anti-fungal test was processed after steam-sterilizing all of the flasks, implements and vermiculite (121°C for 2 h). Before sterilization, vermiculites were uniformly placed at the bottom of the flasks and wetted with 75 mL deionized water. After sterilization, 15 mL of mixed spore suspension was injected into flasks. Following this, wood samples were placed onto vermiculites inside flasks. Eventually, all the specimens were conditioned at a relative humidity of 70% and 22°C for 6 weeks.

RESULTS AND DISCUSSION

Synthesis of cellulose stearoyl ester (CSE) and glycerol stearoyl ester (GSE). In order to prepare hydrophobic and superhydrophobic wood, the raw materials CSE and GSE for the coating were synthesized at first (**Scheme 1**). Esterification of cellulose and glycerol was successfully carried out using stearoyl chloride as confirmed by FT-IR and ^{13}C NMR spectra of CSE and GSE in deuterated benzene (**Figure 1**). The DS_{SE} of CSE was calculated as 3 using the results from elemental analysis and all the hydroxyl groups of GSE were esterified by stearoyl groups as confirmed by its ^{13}C NMR spectrum.

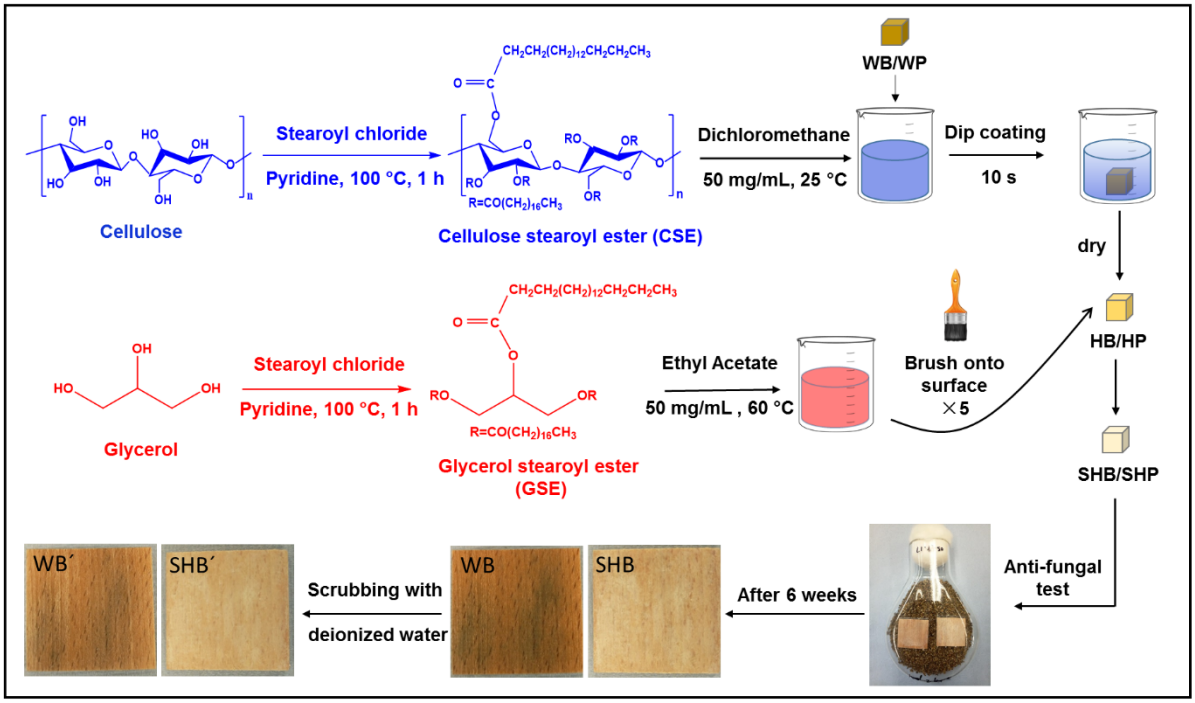

Scheme 1. Schematic overview for the synthesis of cellulose stearoyl ester and glycerol stearoyl ester as well as the fabrication of hydrophobic and superhydrophobic wood (beech and pine). WB/WP: washed beech and pine; HB/HP: hydrophobic beech and pine; SHB/SHP: superhydrophobic beech and pine.

The FT-IR spectra showed characteristic peaks of CSE and GSE (**Figure 1a**). In the spectra of MCC and glycerol, the peaks near 3305 cm^{-1} represent OH groups, while these peaks disappeared in the spectra of CSE and GSE. New bands appear at 2917 and 2850 cm^{-1}, which are attributed to the asymmetric and symmetric stretching vibrations of methylene groups, respectively. Another new signal at 1747 cm^{-1} is ascribed to the stretching vibrations of C=O groups and the new band at 1467 cm^{-1} is derived from the deformation vibrations of C-H groups of long aliphatic chains. In addition, new bands at 1159 and 721 cm^{-1} are ascribed to stretching and rocking vibrations of C-C groups of long aliphatic chains, respectively.

In ^{13}C NMR spectra of GSE and CSE (**Figure 1b** & **1c**), the signals between 10-35 ppm represent carbons in aliphatic ester groups. The single peaks can be classified as shown within the ^{13}C NMR spectra (Zhang, Geissler et al. 2015). Within the spectrum of GSE, the signals at 70 and 63 ppm are typical for C1 and C2/C3. The peaks at 173 ppm are ascribed to the carbons of

C=O groups. Within the spectrum of CSE, the peaks between 171 and 173 ppm are attributed to carbons of C=O groups at C6, C3 and C2 position of anhydroglucose units of cellulose.

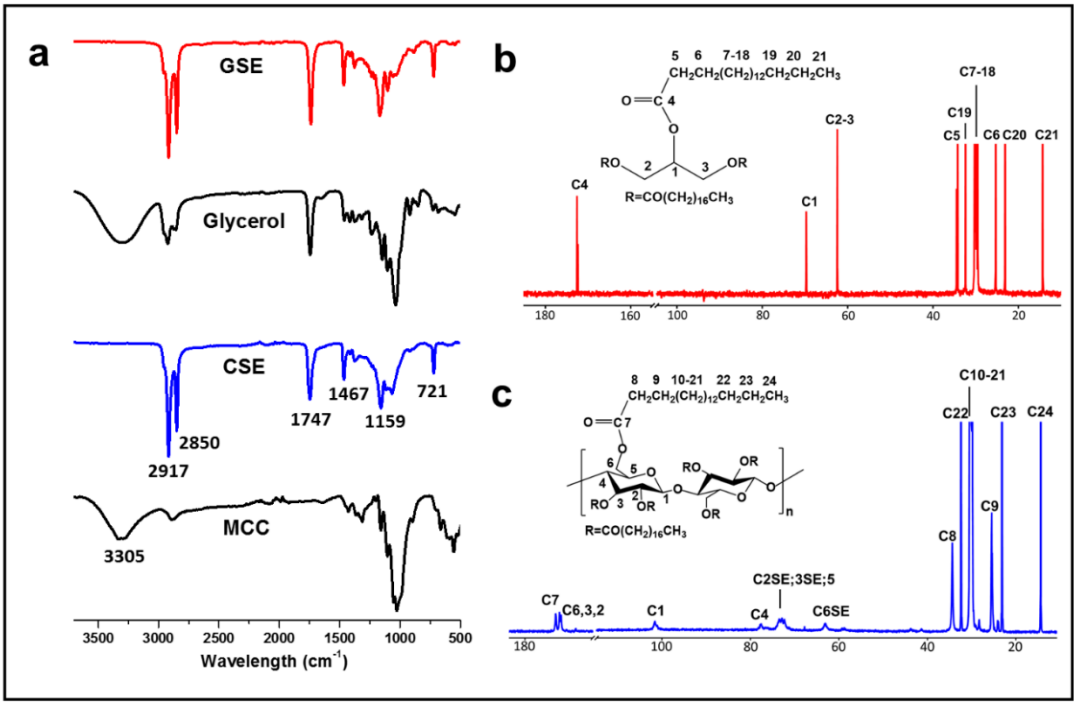

Figure 1. FT-IR and ^{13}C NMR spectra of CSE and GSE recorded in benzene-d6: a) the FT-IR spectra of MCC, CSE, glycerol and GSE, respectively. b) ^{13}C NMR spectrum (185-10 ppm) of GSE; c) ^{13}C NMR spectrum of CSE (185-10 ppm).

Preparation of hydrophobic and superhydrophobic wood. As shown in Scheme 1, the surfaces of wood samples turned hydrophobic and superhydrophobic during the two coating steps. WB/WP were dip-coated in CSE solution and dried under ambient conditions, leading to HB/HP with the 1st hydrophobic layer. Then, brush-coating GSE solution onto HB/HP and drying under ambient conditions led to the fabrication of SHB/SHP with the 2nd superhydrophobic layer. The brushing and drying process was repeated for 5 times, in order to cover the whole surface using GSE. Eventually, the superhydrophobic wood surfaces with hierarchical micro-/nanostructure and self-cleaning property were obtained (Supporting Movie S1 and S2). After the dip-coating process, the average weights of adsorbed CSE on beech and pine sample were 13±4 and 18±2 mg/g, respectively. After subsequent brushing coating, the

average weights of GSE on hydrophobized beech and pine surface (40 mm×40 mm) were 8±3 and 8±1 mg/cm^2.

As shown in **Figure 2**, it is obvious that these coating treatments didn't lead to a notable change of the appearance of both beech and pine wood samples. However, their surface wetting ability was significantly modified, as represented by static WCAs of these surfaces.

Static WCAs of water droplets on WB and WP are 64° and 80° after 5 s, respectively. The results show similar WCAs as published papers (Hakkou, Pétrissans et al. 2005, Wang, Piao et al. 2011), which present hydrophilic properties. After the dip-coating in CSE solution and drying, the static WCAs on beech (HB) and pine (HP) increased to 122° and 118°, showing enhanced hydrophobic properties. After further brush-coating with GSE solution, the static WCAs of beech (SHB) and pine (SHP) increased to 159° and 155°, respectively. These values are similar to the known static WCAs of other superhydrophobic woods, for example wood treated with ZnO (Wang, Shi et al. 2011, Chang, Tu et al. 2015). These results confirmed the successful formation of hydrophobic and superhydrophobic wood surfaces using the two coating steps. Moreover, both the treated beech and pine exhibited similar superhydrophobic properties, which demonstrates the efficiency of the method for both hard- and softwood. In addition, the insensitivity of the method to substrate further shows the applicability of these methods and the coating materials to increase the surface hydrophobicity of diverse other substrates.

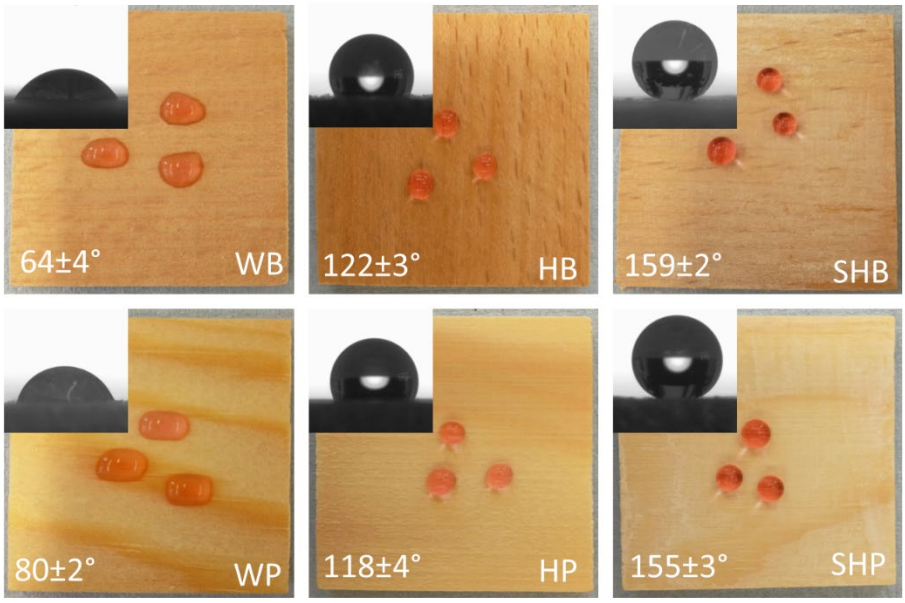

Figure 2. Appearance and static water contact angles (in insets) of non-treated and treated wood as beech (WB, HB and SHB) and pine (WP, HP and SHP). The water droplets were dyed with tee and the photos were taken after the droplets put onto wood for 5 s.

Surface morphology of untreated and treated wood. Comparing the SEM images of WB/WP with those of HB/HP in **Figure 3**, a relatively smooth and continuous membrane with cracks could be observed under higher magnification on HB/HP. This should be due to the formation of the continuous CSE layer on the rough wood surface, which partially fills the cavities at the surface during the fast evaporation of DCM. However, the textures of the wood surface of both beech and pine are still clearly visible, meaning that the CSE layer was very thin (**Figure 3**, HB and HP). Thus, the low surface roughness of this thin CSE layer can only contribute to the formation of hydrophobic surfaces. To exactly determine the thickness of the 1st coating, one has to perform a model experiment on flat and non-porous substrates, as we have shown before (Geissler, Bonaccurso et al. 2014). The thickness of the coating was 53±0.8 nm, when a CSE/DCM solution with the same concentration of 10 mg/ml was used for coating wafer substrates. Based on this paper and the unique structure of wood, the evaluated thickness of the 1st coating on wood surface should be slightly less than 53 nm.

In comparison to HB/HP, subsequent brush-coating of GSE for the fabrication of SHB/SHP led to extremely coarse surfaces with a highly-textured cellular structure (**Figure 3**, SEM images

of SHB and SHP). This structure is based on the crystallized GSE at the surface, which enhanced the surface roughness at microscale. Moreover, the GSE layer shows coarse and non-uniform surface with porous structure. This structure should contribute to the formation of superhydrophobic surfaces by trapping air between wood surfaces and water droplets. Regarding the 2nd coating, GSE can be deposited on the surface of the wood and inside the vessels of wood structure after drying. Thus, it's not easy to obtain an accurate value of the coating thickness. According to the SEM measurements, we can estimate that the thickness of 2nd layer on wood surfaces should be between 20 and 30 μm. Furthermore, for the preparation of the GSE surface, the GSE solution in ethyl acetate was brush-coated on the surface. This solution will slightly swell the CSE layer and there is no clear separation between the CSE layer and GSE layer.

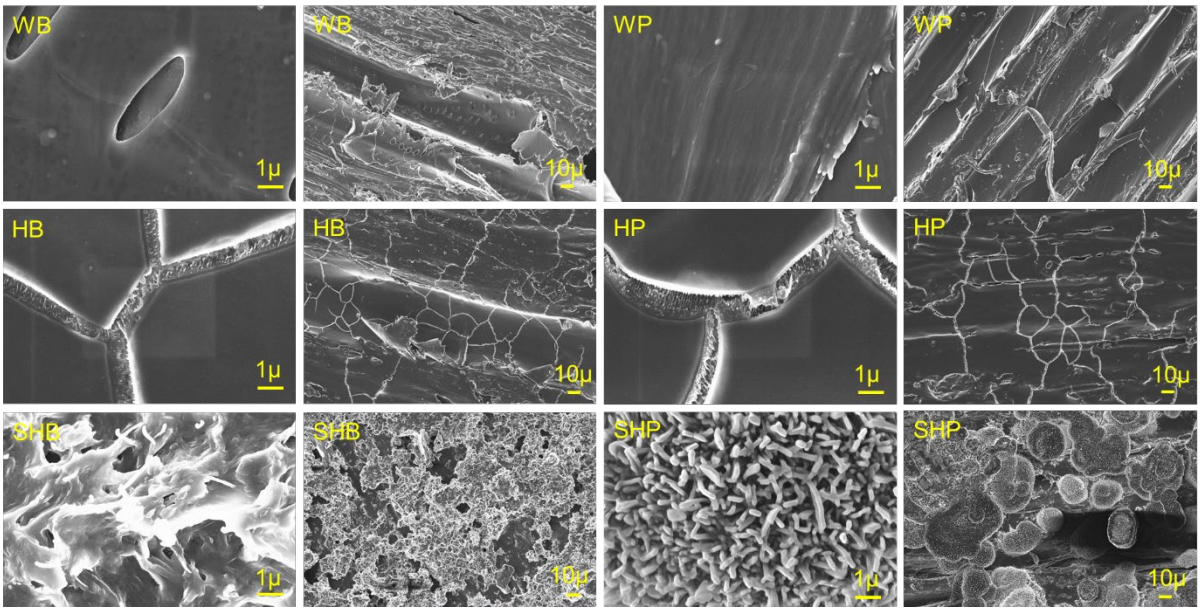

Figure 3. Representative SEM images of wood surfaces of beech (WB, HB and SHB) and pine (WP, HP and SHP) at diverse magnifications.

Anti-fungal tests. Figure 4 exhibits the appearances of treated and untreated wood samples after fungal cultivation and compares the appearances of the wood before and after scrubbing with deionized water. Grey and black dots belonging to the spores of fungi were present on WB/WP surfaces after fungal cultivation. After scrubbing with deionized water, significant

amounts of grey and black dots still existed on WB'/WP' surfaces, which can be explained by the intrusion of fungi inside the wood samples.

However, HB/HP samples exhibited fewer spores on the surface after the cultivation of fungi, which illustrated better anti-fungal properties compared with WB/WP. After scrubbing with deionized water, fewer grey and black dots can be found on HB'/HP' wood surfaces, but still some spores are visible in HB'/HP' wood samples after the cleaning process.

In comparison, much fewer spores are notable on the SHB/SHP surfaces after fungal cultivation (**Figure 4**, SHB/SHP). These spores could be easily removed by scrubbing with deionized water, leading to SHB'/SHP' with clean surfaces again.

The WCA on diverse wood specimens were measured again after scrubbing process (**Figure 4**). WCA values on WB and WP maintained with slight increase to 79±4° and 81±4°, respectively. On the contrary, the WCA values of HB/HP and SHB/SHP after scrubbing treatment were all slightly reduced. This should be caused by the partial smoothing of the surface coating during scrubbing process. Nevertheless, HB/HP stayed hydrophobic properties and SHB/SHP still maintained highly hydrophobicity with WCA of over 140°.

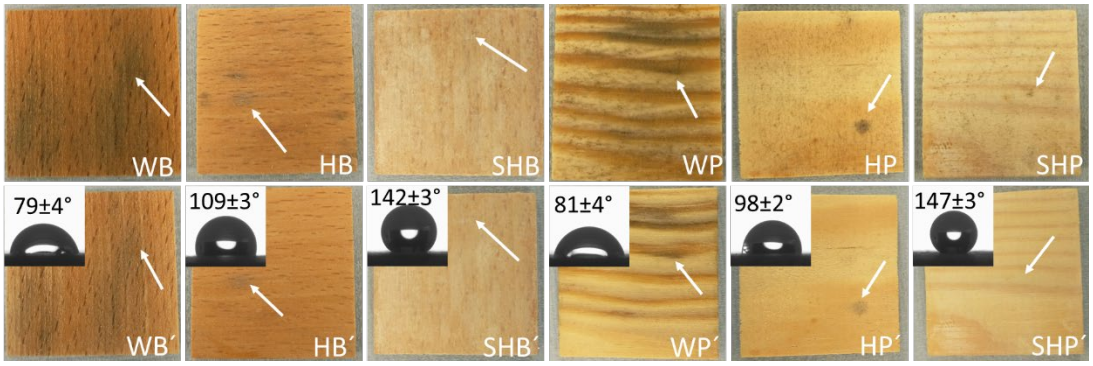

Figure 4. Representative photo images of wood samples after anti-fungal test for 6 weeks and static contact angles on wood surfaces after further scrubbing with deionized water: WB/WP, HB/HP, SHB/SHP were the wood samples after 6 weeks anti-fungal test. WB'/WP', HB'/HP', SHB'/SHP' were the same samples after further scrubbing with deionized water.

Figure 5 shows the growth and distribution of these fungal spores within the wood samples. In the images of WB/WP, the darker section with grey and black colors was contaminated by fungi,

which demonstrates the intrusion of fungi into the wood samples. Compared HB/HP with WB/WP, the cross-sections of HB/HP showed fewer fungi spores due to the hydrophobic CSE membranes on wood. This proved that a barrier against water penetration can increase anti-fungal properties. However, still some grey and black dots could be observed on the profile of HB/HP. This can be explained by the existence of cracks in the CSE membrane. Even though the hydrophobic CSE membrane can prevent fungal spores from inside wood structures, the cracks in the membrane still provide access for fungal spores intruding wood. Nevertheless, the profiles of SHB/SHP samples are absolutely clear, indicating no intrusion of fungi during the 6 weeks cultivation. Thus, the double coating superhydrophobic layer highly enhanced the anti-fungi properties of the single layer coating using CSE and absolutely prevented the penetration of fungi. The fungi only grew on the surface of the superhydrophobic layers constructed by GSE and could be easily removed after gentle scrubbing with wet paper tissue.

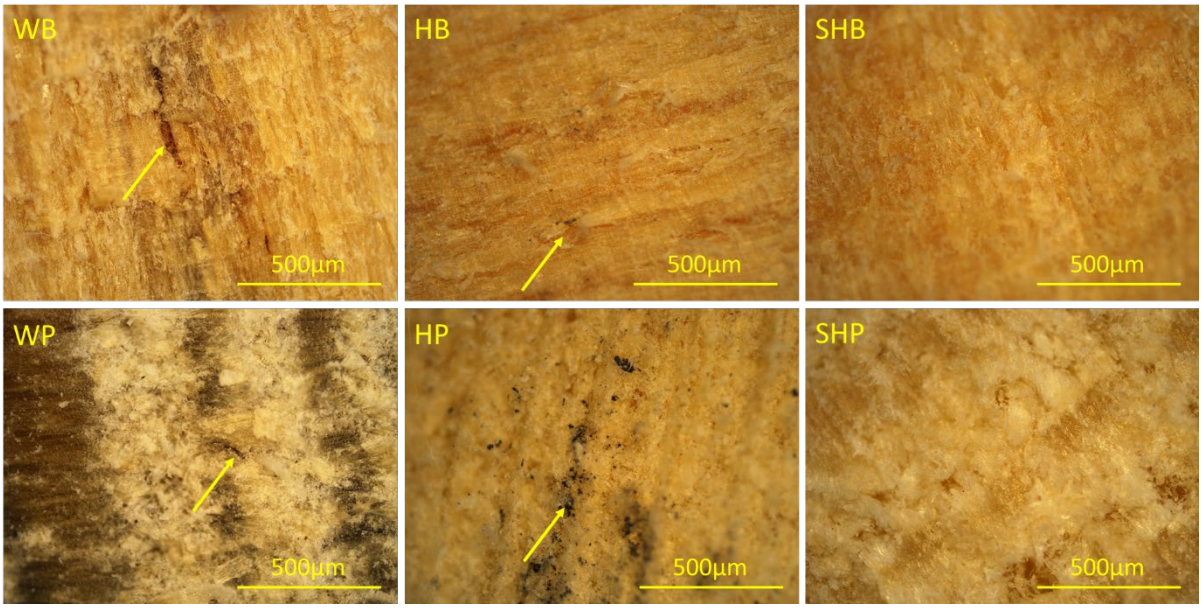

Figure 5. Representative light microscopy images of the morphology of profiles of WB/WP, HB/HP and SHB/SHP. The profiles were fabricated by cutting the wood along the direction that is perpendicular to the annual ring.

Conclusion

In summary, we studied the anti-fungal effects of hydrophobic and superhydrophobic coatings on wood, which has been realized via a facile method using pure organic materials. The method could be applied to both hard wood (beech) and soft wood (pine). Cellulose stearoyl ester (CSE) and glycerol stearoyl ester (GSE) were used to create the hydrophobic and superhydrophobic surfaces, respectively. Two coating steps were involved for the fabrication of superhydrophobic wood: dip-coating with CSE and brush-coating with GSE. The static WCAs on hydrophobic beech (HB) and pine (HP) were 122° and 118°, while those on superhydrophobic beech (SHB) and pine (SHP) were around 159° and 155°, respectively. After dip-coating with CSE, a hydrophobic membrane with cracks was formed on wood substrate. The obtained superhydrophobicity on wood surfaces should be primarily attributed to the combination of CSE membrane and coarse and highly-textured cellular structure resulted from GSE, which leads to the ability to extensively trap air between water droplets and wood surfaces. Anti-fungal tests further showed the beneficial properties of the hydrophobic and superhydrophobic treatment for the anti-fungal properties. When untreated wood were attacked by fungi severely, both at the surface and in the interior, hydrophobic and superhydrophobic wood showed better anti-fungal properties. Comparing hydrophobic with superhydrophobic wood, significant anti-fungal properties by maintaining their clean and clear wood structures could only be maintained by SHB/SHP. This could be explained by the synergistic effect of hydrophobic membrane formed by CSE and hierarchical structure on wood surface caused by GSE. Thus, we provided here an efficient method containing two coating steps with pure organic compounds for the surface coating, wood protection, and construction of nanostructures on wood substrates. To date, fungicide was generally used for anti-fungal coating, which already causes a lot of environmental issues. This study demonstrated the use of superhydrophobicity for anti-fungal application, which provides a new potential solution by only constructing nano/microstructures on wood surfaces.

ASSOCIATED CONTENT

Supporting information.

Superhydrophobic beech (mp4)

Superhydrophobic pine (mp4)

ACKNOWLEDGEMENT

Y.Y. thanks the China Scholarship Council (CSC) for financial support. K.Z. thanks Georg-August-University of Goettingen for the Anschubfinanzierung (Funding for the promotion of Young Academics of University of Goettingen) and Fonds der Chemischen Industrie (FCI) for the financial support. Y.Y. thanks Petra Heinze for the help of anti-fungal test; Katharina Dabow and Martin Kaßel for the instruction of Contact Angle Meter.

REFERENCES

Bravery, A. (1988). Biodeterioration of paint—a state-of-the-art comment. Biodeterioration 7, Springer**:** 466-485.

Carey, J. K. (1980). The mechanism of infection and decay of window joinery, University of London.

Chang, H., et al. (2015). "Fabrication of mechanically durable superhydrophobic wood surfaces using polydimethylsiloxane and silica nanoparticles." RSC Advances **5**(39): 30647-30653.

Chen, Y., et al. (2007). "Role of peptide hydrophobicity in the mechanism of action of α-helical antimicrobial peptides." Antimicrobial agents and chemotherapy **51**(4): 1398-1406.

Gao, L., et al. (2015). "A robust, anti-acid, and high-temperature–humidity-resistant superhydrophobic surface of wood based on a modified TiO 2 film by fluoroalkyl silane." Surface and Coatings Technology **262**: 33-39.

Geissler, A., et al. (2014). "Temperature-responsive thin films from cellulose stearoyl triester." The Journal of Physical Chemistry C **118**(5): 2408-2417.

Geissler, A., et al. (2014). "Thermo-responsive superhydrophobic paper using nanostructured cellulose stearoyl ester." Cellulose **21**(1): 357-366.

Guillemot, G., et al. (2008). "Plasma deposition of silver nanoparticles onto stainless steel for the prevention of fungal biofilms: a case study on Saccharomyces cerevisiae." Plasma Processes and Polymers **5**(3): 228-238.

Hakkou, M., et al. (2005). "Investigation of wood wettability changes during heat treatment on the basis of chemical analysis." Polymer degradation and stability **89**(1): 1-5.

Kuroda, K., et al. (2009). "The role of hydrophobicity in the antimicrobial and hemolytic activities of polymethacrylate derivatives." Chemistry-a European Journal **15**(5): 1123-1133.

Lesar, B., et al. (2011). "Wax treatment of wood slows photodegradation." Polymer degradation and stability **96**(7): 1271-1278.

Liu, C., et al. (2011). "Fabrication of superhydrophobic wood surfaces via a solution-immersion process." Applied Surface Science **258**(2): 761-765.

Liu, M., et al. (2015). "Facile fabrication of superhydrophobic surfaces on wood substrates via a one-step hydrothermal process." Applied Surface Science **330**: 332-338.

Raghavan, S. R., et al. (1998). "Composite polymer electrolytes based on poly (ethylene glycol) and hydrophobic fumed silica: dynamic rheology and microstructure." Chemistry of materials **10**(1): 244-251.

Rowell, R. M., et al. (2009). "Understanding decay resistance, dimensional stability and strength changes in heat-treated and acetylated wood." Wood Material Science & Engineering **4**(1-2): 14-22.

Vaca-Garcia, C., et al. (2001). "Determination of the degree of substitution (DS) of mixed cellulose esters by elemental analysis." Cellulose **8**(3): 225-231.

Van de Velde, K. and P. Kiekens (2004). "Structure analysis and degree of substitution of chitin, chitosan and dibutyrylchitin by FT-IR spectroscopy and solid state 13 C NMR." Carbohydrate polymers **58**(4): 409-416.

Wang, C., et al. (2011). "Synthesis and characterization of superhydrophobic wood surfaces." Journal of Applied Polymer Science **119**(3): 1667-1672.

Wang, S. and L. Jiang (2007). "Definition of superhydrophobic states." Advanced materials **19**(21): 3423-3424.

Wang, S., et al. (2011). "Fabrication of a superhydrophobic surface on a wood substrate." Applied Surface Science **257**(22): 9362-9365.

Wen, L., et al. (2015). "Bioinspired Super-Wettability from Fundamental Research to Practical Applications." Angewandte Chemie International Edition **54**(11): 3387-3399.

Xie, Y., et al. (2008). "Weathering of uncoated and coated wood treated with methylated 1, 3-dimethylol-4, 5-dihydroxyethyleneurea (mDMDHEU)." European Journal of Wood and Wood Products **66**(6): 455-464.

Yin, L. M., et al. (2012). "Roles of hydrophobicity and charge distribution of cationic antimicrobial peptides in peptide-membrane interactions." Journal of Biological Chemistry **287**(10): 7738-7745.

Zabel, R. and F. Terracina (1978). "Nutrition of saprobic fungi and control strategies for paint mildew caused by< i> Aureobasidium pullulans." Journal of coatings technology **50**(639): 43-47.

Zabel, R. and F. Terracina (1980). The role of Aureobasidium pullulans in the disfigurement of latex paint films. Developments in industrial microbiology**:** 179-190.

Zabel, R. A. and J. J. Morrell (2012). Wood microbiology: decay and its prevention, Academic press.

Zhang, K., et al. (2015). "Polymeric flower-like microparticles from self-assembled cellulose stearoyl esters." ACS Macro Letters **4**(2): 214-219.

Scheme 1. Schematic overview for the synthesis of cellulose stearoyl ester and glycerol stearoyl ester as well as the fabrication of hydrophobic and superhydrophobic wood (beech and pine). WB/WP: washed beech and pine; HB/HP: hydrophobic beech and pine; SHB/SHP: superhydrophobic beech and pine.

Figure 1. FT-IR and ^{13}C NMR spectra of CSE and GSE recorded in benzene-d6: a) the FT-IR spectra of MCC, CSE, glycerol and GSE, respectively. b) ^{13}C NMR spectrum (185-10 ppm) of GSE; c) ^{13}C NMR spectrum of CSE (185-10 ppm).

Figure 2. Appearance and static water contact angles (in insets) of non-treated and treated wood as beech (WB, HB and SHB) and pine (WP, HP and SHP). The water droplets were dyed with tee and the photos were taken after the droplets put onto wood for 5 s.

Figure 3. Representative SEM images of wood surfaces of beech (WB, HB and SHB) and pine (WP, HP and SHP) at diverse magnifications.

Figure 4. Representative photo images of wood samples after anti-fungal test for 6 weeks and after further scrubbing with deionized water: WB/WP, HB/HP, SHB/SHP were the wood samples after 6 weeks anti-fungal test. WB'/WP', HB'/HP', SHB'/SHP' were the same samples after further scrubbing with deionized water.

Figure 5. Representative light microscopy images of the morphology of profiles of WB/WP, HB/HP and SHB/SHP. The profiles were fabricated by cutting the wood along the direction that is perpendicular to the year ring.

Publication 2

Chiral hierarchical structure in glucose stearoyl esters and the role of bond configuration

Yawen Yao[1#], Qiyun Tang[2#], Sabine Rosenfeldt[3], Marcel Krüsmann[4], Matthias Karg[4], Kai Zhang[1*]

[1] Wood Technology and Wood Chemistry, Dept. Wood Technology and Wood-based Composites, Georg-August-University of Göttingen, Büsgenweg 4, 37077 Göttingen, Germany.

[2] Institute of Theoretical Physics, Georg-August-University of Göttingen, Friedrich-Hund-Platz 1, 37077 Göttingen, Germany

[3] Department of Chemistry and Bavarian Polymer Institute, University of Bayreuth Universitätsstraße 30, 95447 Bayreuth, Germany

[4] Institute of Physical Chemistry I: Colloids and Nanooptics, Heinrich Heine University, Universitätsstr.1, 40225 Düsseldorf, Germany.

* E-mail: kai.zhang@uni-goettingen.de

Manuscript

Abstract

Chirality is ubiquitous in nature, especially in biomolecules. Biomolecules with diverse chirality may lead to huge differences in chemical structures and biological functions. Here we show for the first time that chiral, hierarchical superstructures can be obtained from D/L-glucose stearoyl esters (D/L-GlcSE). Chiral 'left-handed' (counterclockwise) spiralling morphology can be obtained by D-GlcSE, while 'right-handed' (clockwise) morphology can be induced by L-GlcSE. The α configuration leads to irregular aggregates, which show worse thermal and crystallization properties, while mature round smooth microparticles with better thermal and crystallization properties are beneficial from β configuration. Axially stretched α configuration improves the difficulties of stacking of GlcSE molecules during self-assembly, while better stacking is beneficial from equatorially stretched β configuration. However, only when appropriate number of bonds stretching axially/equatorially (α/β of 20/80) can result in chirality in microparticles. Besides, other conditions including aging temperature, concentration and cooling rate were also studied. Thus, these findings suggest a chiral growth mechanism for how sugar-based chiral molecules might exert hierarchical control to form left- and right-handed chiral superstructures.

Introduction

Chirality is a ubiquitous phenomenon in nature and living matters and is universal from subatomic, atomic, molecular, nanoscale, microscale and even bigger scale which can be observed by our bare eyes.[1-6] The standard definition of chirality can be explained as the two similar objects which cannot be superimposed onto each other but are symmetric with its mirror-image.[7] From atom level, an efficient way to distinguish a chiral atom is to see if there are asymmetric carbon atoms in the molecules, which connecting 4 diverse atoms or groups of atoms. Chirality also exists in molecules including amino acids and monosaccharides, macromolecular superstructures such as chiral microparticles, biominerals like helical snail and sea shells and human organs such as human hands, to name a few.

Hierarchical chiral superstructures have attracted wide interests due to the formation of complex nano- and micro-architecture morphologies. The most studied chiral superstructures include self-assembled microparticles[8], calcium carbonate in biomineralization[3,7,9] and cholesteric liquid

crystals[4,10-13]. Typical supramolecular chirality in self-assembled microparticles were reported from both inorganic and organic compounds such as fullerene[8] and naphthalenediimide[14], respectively. For example, Nakashima et al. reported the helical nanostructures in the shapes of rings, irregular rings, lassos, handcuffs, catenanes, pseudorotaxanes, and figure-eight structures using fullerene C70-filled carbon nanotubes and empty single-walled carbon nanotubes via aqueous dispersions.[15] Nakanishi et al. introduced flower-shaped supramolecular assemblies from fullerene bearing long aliphatic chains. Remarkably, enantiopure 2-(R)- and 2-(S)-butanol solution of modified fullerene can be used to obtain left-handed and right-handed micrometer-sized spiral architectures.[8] The possible explanation for the handedness may be the weak interactions between the hydroxy groups in butanol and fullerene derivatives. Besides, Shang et al. achieved left-handed and right-handed complex chiral motifs composed of seven C60 molecules on Cd (0001).[16] Shejul et al. studied the aggregation-induced emission characteristics of the solvent triggered hierarchical self-assembled chiral superstructures from naphthalenediimide amphiphiles.[14] Chirality is also commonly found in biological systems including invertebrate marine and terrestrial organisms. Two famous examples are helical snail shells and the already extinct ammonites.[7] Some publications explained that the formation of chirality in biology is due to the chiral molecules. However, how to connect the chiral molecules to the hierarchical superstructures in invertebrate marine and terrestrial organisms have been verified difficult. In order to deeply understand the mechanism, many groups studied the formation of chiral structures with handedness by introducing acidic amino acid (D/L-aspartic acid)[7,9,17] or chiral α-hydroxycarboxylic acids (D/L-malic acid, D/L-lactic acid, D/L-tartaric acid)[18] into calcium phosphate, calcium carbonate or calcium oxalate. For example, Jiang et al. reported the formation of left-handed and right-handed calcium carbonate microparticles induced by chiral acidic amino acids.[7] The possible mechanism could be explained by the nanoparticle tilting after binding of chiral amino acids. When connected with chiral acidic amino acids, the 'mother' units slightly tilt and consequential 'daughter' units amplify the minor tilt by forming major displacement. Thus, chiral hierarchical structures with handedness formed. In the drug industry and nanoscience, sometimes you can only obtain racemic chiral materials. Thus, enantiomer sorting is a big challenge in application. The optical enantioseparation has been fully studied by many groups. Among all, chiral cholesteric liquid crystals are excellent models to study passive all-optical enantioselective sorting of chiral particles from lateral optical forces

induced by linearly or circularly polarized laser beams.[4,10,11,13] This technology has a huge potential use in research areas including optical trapping and manipulations, microfluidics and optofluidics, sensors, photonics, photonics crystals, colloidal and materials science. Beside chiral cholesteric liquid crystals, other chiral materials such as polyacetylene[19-21] have also been introduced. Based on the publications mentioned above, the emergence of supramolecular chirality might be triggered by the chirality transfer, chirality amplification and asymmetry breaking of either chiral or achiral compounds in single or multiple component systems. Nevertheless, the progress of our understanding on how chiral superstructures are formed from chiral molecules and/or achiral molecules has been proved to be slow.

Beside the mentioned publications, glucose-based materials are also very interesting due to the large scale, inexpensive and green properties. Furthermore, glucose can also be divided into D- or L-, based on whether the -OH at C5 stretching on the right (Dextro) or left (Levo) in the Fischer formulas. It has been widely accepted that chiral superstructures can be achieved via self-assembly by using external stimuli. However, how to obtain chirality without using external stimuli and why chiral superstructures formed are still understudied. Furthermore, no study of chiral superstructures from monosaccharides has been reported before. Moreover, how diverse factors including aging temperature, aging time, concentration and cooling rate determine the final chiral superstructures need more profound investigation. In this study, we for the first time report the formation of chiral microparticles by only using D/L-glucose stearoyl esters (D/L-GlcSE) via self-assembly without applying external stimuli. It was found that D- and L-configuration can lead to 'left-handed' and 'right-handed' spiralling microparticles. In order to have a deep understanding of how and why chiral superstructures are formed, other conditions including aging temperature, aging time, concentration and cooling rate were also compared and studied.

Results

Synthesis, characterization of D/L-GlcSE and preparation of D/L-GlcSE microparticles

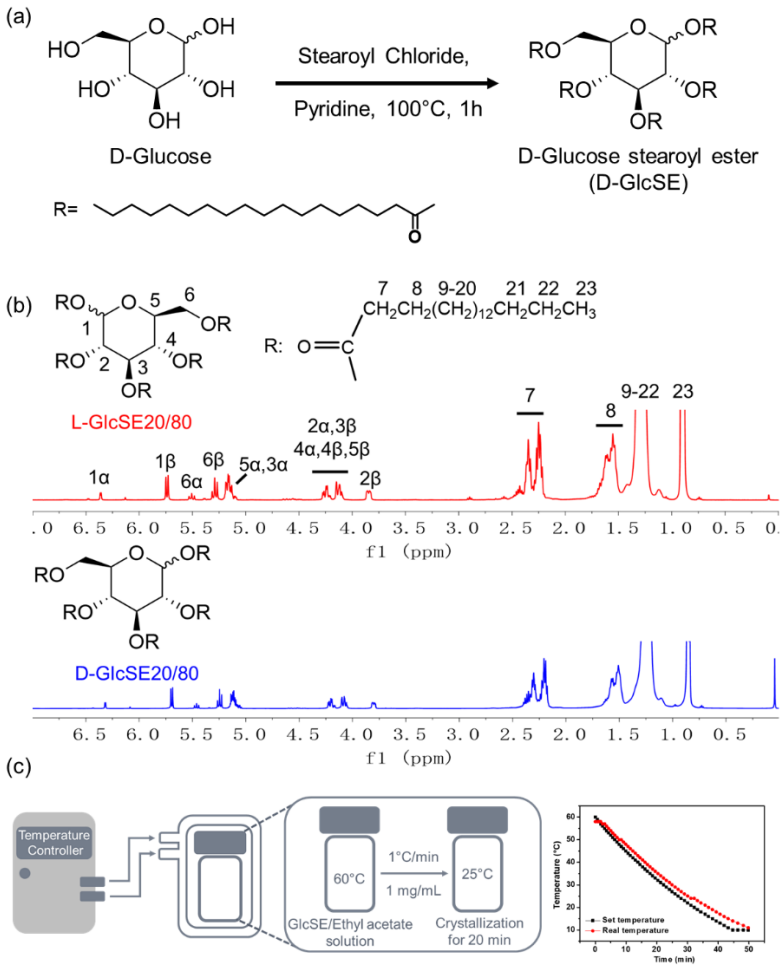

Figure 1. Synthesis, characterization of D/L-GlcSE and preparation of D/L-GlcSE microparticles a) Schematic illustration of the synthesis of D/L-GlcSE; **b)** ^{1}H NMR spectra of the synthesized D/L-GlcSE; **c)** Schematic illustration of the preparation of chiral microparticles from D/L-GlcSE.

D/L-Glucose stearoyl esters (D/L-GlcSE) can be obtained by using D/L-glucose, stearoyl chloride in pyridine at 100°C for 1 h as shown in **Figure 1a**. The synthesis of D-GlcSE and L-GlcSE were exactly the same by using the same amount of stearoyl chloride and pyridine. After synthesis, the obtained materials were characterized by using ^{1}H NMR spectra. It has been verified that D-GlcSE and L-GlcSE have absolutely the same ^{1}H NMR spectra due to the same molecular formula regardless of the D/L configurations. The detailed information has been marked in **Figure 1b**. Notably, glucose can be divided into α/β-glucose according to the -OH

configuration at C1 in both D- and L-glucose. After synthesis, both of the obtained D- and L-GlcSE exhibit the α/β ratio of 20/80 which can be verified according to ^{1}H NMR (**Figure 1b**). Thus, the involved D/L-GlcSE can be named as D-GlcSE20/80 and L-GlcSE20/80. The preparation of chiral microscale superstructures from D/L-GlcSE can be achieved by using temperature controller and ethyl acetate. First, D/L-GlcSE were dissolved into ethyl acetate with the concentration of 1 mg/mL at 60°C. Then the temperature was decreased from 60°C to 25°C with a cooling rate of 1 °C/min. When the temperature reached to 25°C, the precipitations were aged at 25°C for 20 min. Finally, the precipitations were taken out to a smooth Si-wafer for drying and characterization by SEM. Furthermore, diverse conditions such as different aging temperatures, cooling rates and aging time will also be compared in details.

Morphology and the formation process of D/L-GlcSE

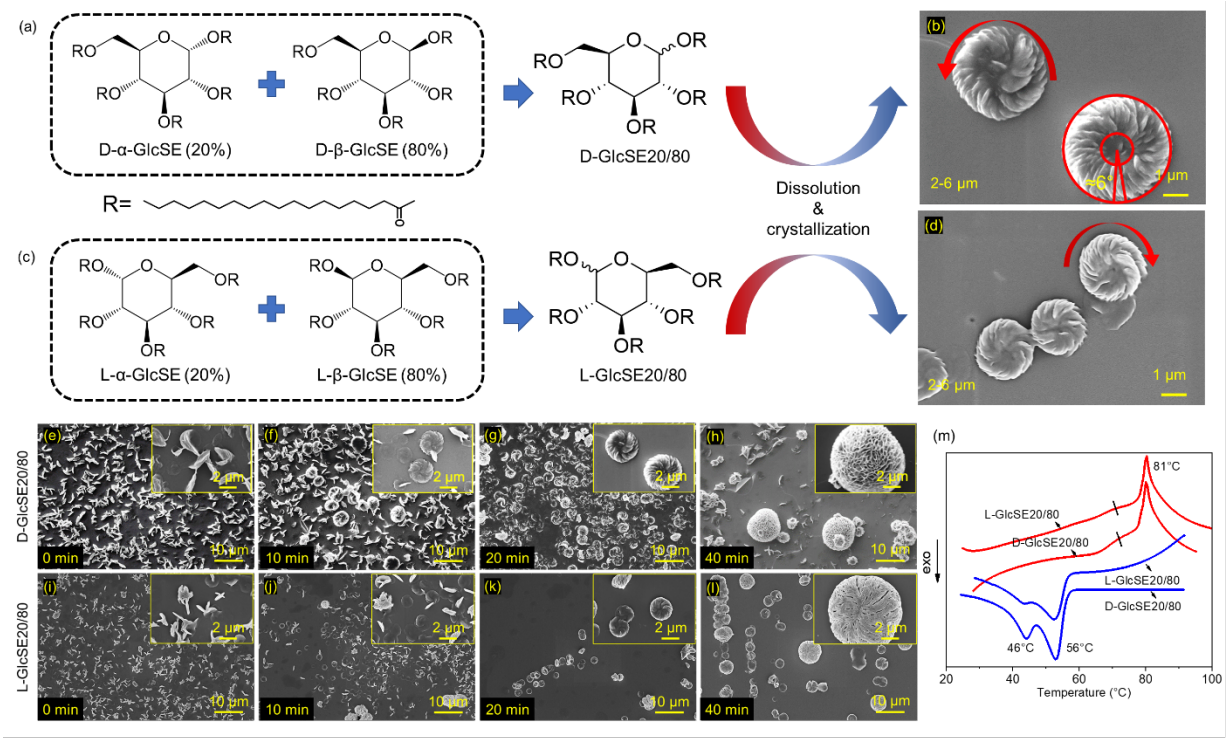

Figure 2. Chiral microparticles from D/L-GlcSE20/80 and the formation process. a and **c)** Haworth structures of D/L and α/β configuration of GlcSE; SEM images of **b)** left-handed and **d)** right-handed microparticles; SEM images of self-assembled aggregates from **e-h)** D-GlcSE20/80 and **i-l)** L-GlcSE20/80 prepared with their solutions in ethyl acetate at the concentration of 1

mg/mL from 60°C to 25°C with the cooling rate of 1 °C/min and aged at 25°C for 0, 10, 20 and 40 min, respectively. **m)** DSC heating and cooling curves of L/D-GlcSE20/80.

By decreasing the temperature of D/L-GlcSE20/80 solutions in ethyl acetate with the concentration of 1 mg/ml from 60°C to 25°C and aged for 20 min at 25°C, chiral microscaled precipitates with flaky nanostructures were formed instantly (**Figure 2b** and **d**). As shown in **Figure 2e-l**, different aging time at 25°C of 0, 10, 20 and 40 min led to petal shapes, cookie shapes and microparticles, respectively. Without aging time, the as-prepared precipitates right after the reaching 25°C exhibited no cookie-shaped morphology, but only curly petal-shaped pieces with the thickness between 0.5 μm to 2 μm. After aging for 10 min, prototypes of cookie-shaped microparticles with the diameter between 1 μm to 5 μm were obtained even though still amounts of curly petal-shaped structures dispersed around them. After aging for 20 min, typical left-handed and right-handed cookie-shaped morphology with the diameters between 2 μm to 6 μm were obtained from D-GlcSE20/80 and L-GlcSE20/80. The morphology is similar to the chiral hierarchical structures obtained from fullerene and calcium carbonate. The petals in the left- and right-handed cookie-shaped morphology have a displacement of around 6° anti-clockwise and clockwise, respectively. When aged for 40 min, the formed hierarchical structures are assigned as over-grown, porous microparticles, with the size over 10 μm and the handedness disappeared. According to the DSC measurement of the microparticles from L/D-GlcSE20/80, they exhibit absolutely the same thermal properties. To be precise, both L/D-GlcSE20/80 have the same melting temperature (T_m) of 81°C and two crystallization temperature (T_c) of 46°C and 56°C.

Separation and characterization of D-GlcSE with diverse α/β configurations

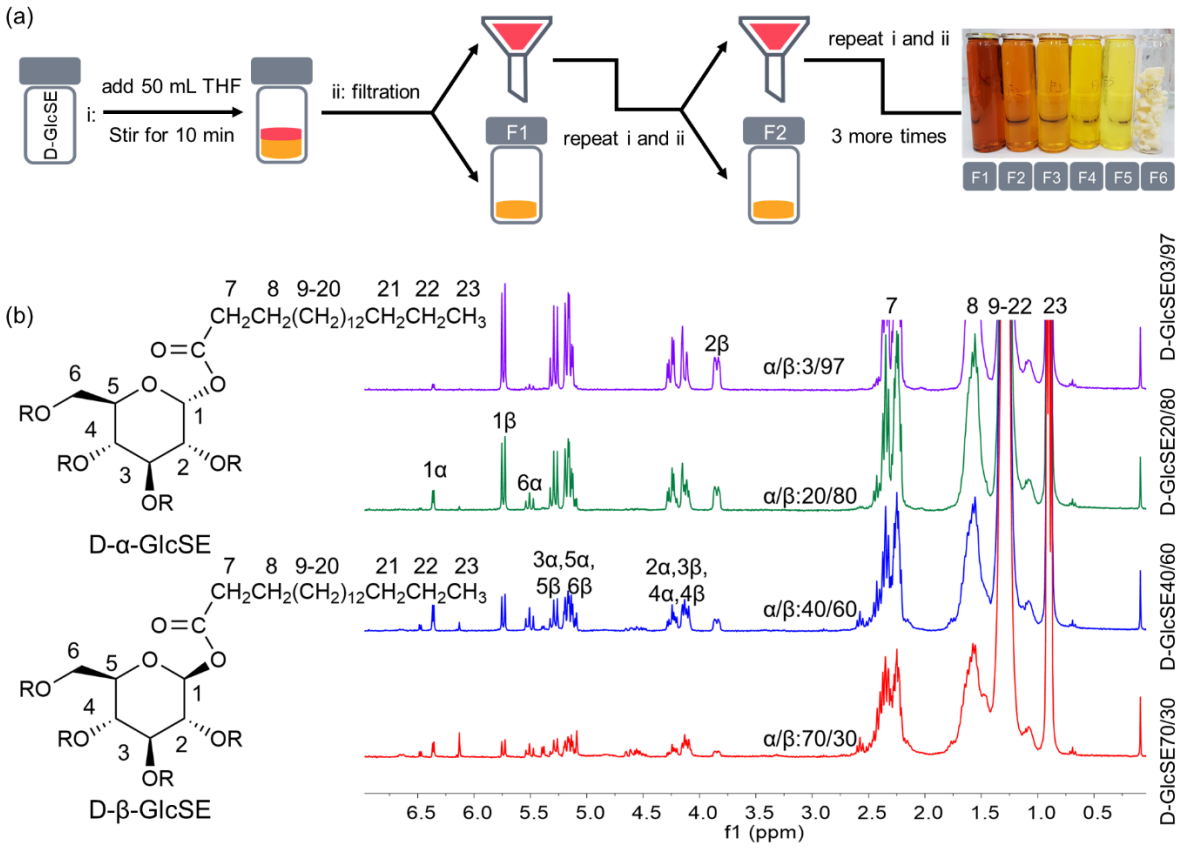

Figure 3. Separation and characterization of D-GlcSE with diverse α/β configurations. a) Schematic illustration of the separation of D-GlcSE with diverse α/β configurations; **b)** ^{1}H NMR spectra of the obtained D-GlcSE with diverse α/β configurations.

During the experiment, it was found that the solubility of D-β-GlcSE in THF is slightly lower than D-α-GlcSE. Thus, the preparation of D-GlcSE with diverse α/β ratios can be achieved by dissolving D-GlcSE20/80 in THF and filtration (**Figure 3a**). First, the purified D-GlcSE and 50 mL THF were added into a beaker and stirred for 10 min. Then, the mixture was separated into solid phase and liquid phase. After filtration, the obtained liquid phase was dried and named as Fraction 1 (F1). Meanwhile, the solid phase was mixed with another 50 mL THF for 10 min. Afterwards, similar solid phase and liquid phase were observed in the mixture. After filtration, the liquid phase was dried and named as F2, while the dissolving and filtration procedure was kept using for the solid phase to get F3, F4, F5 and F6. After dried, all of these 6 samples were

characterized by ^{1}H NMR. According to the spectra, four different α/β ratios of 70/30, 40/60, 20/80 and 03/97 were determined (**Figure 3b**). Then, these samples were named as D-GlcSE70/30, D-GlcSE40/60, D-GlcSE20/80 and D-GlcSE03/97, respectively.

Morphology, thermal and crystallization properties of microparticles prepared from D-GlcSE with diverse α/β ratios

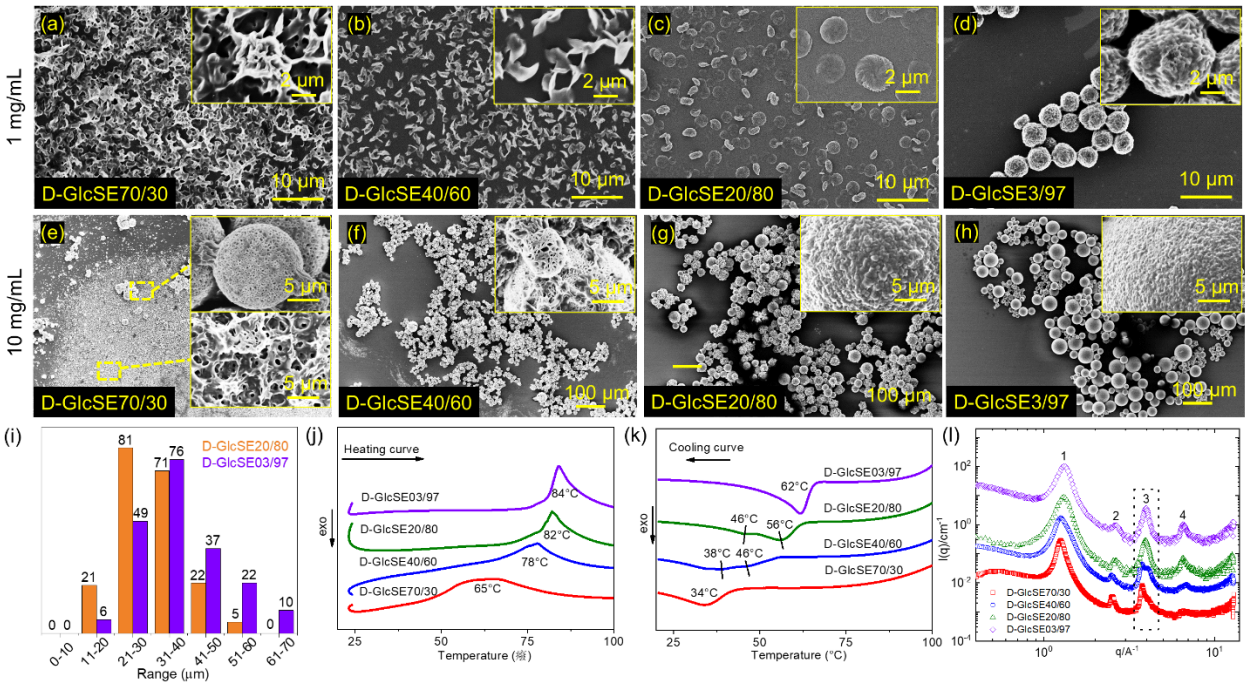

Figure 4. SEM, DSC and SAXS characterization of the microparticles prepared from D-GlcSE with diverse α/β ratios. a-d) SEM images of self-assembled aggregates prepared from D-GlcSE with diverse α/β ratios with the concentration of 1 mg/mL from 60°C to 25°C with the cooling rate of 1 °C/min and aged at 25°C for 20 min; **e-h)** SEM images of self-assembled aggregates prepared from D-GlcSE with diverse α/β ratios with the concentration of 10 mg/mL from 60°C to 10°C with the cooling rate of 1 °C/min and aged for 2h; **i)** Size distribution of microparticles prepared from **g)** D-GlcSE20/80 and **h)** GlcSE03/97 with the concentration of 10 mg/mL from 60°C to 10°C with the cooling rate of 1 °C/min and aged for 2h; DSC curves as **j)** heating and **k)** cooling as well as **l)** SAXS curves of the D-GlcSE with different α/β ratios.

When prepared with the concentration of 1 mg/mL (**Figure 4a-4d**), it can be seen that with more α configuration, the self-assembled D-GlcSE exhibit irregular aggregates (**Figure 4a**), while with the increasing of β configuration, petal shapes (**Figure 4b**), cookie shapes (**Figure 4c**) and microparticles (**Figure 4d**) were obtained. However, only cookie shapes prepared from D-GlcSE20/80 show chirality. When D-GlcSE70/30, D-GlcSE40/60, D-GlcSE20/80 and D-GlcSE03/97 were self-assembled with the concentration of 10 mg/mL from 60°C to 10°C, all of them exhibit microparticle structures (**Figure 4e-4h**). Nevertheless, for D-GlcSE70/30 (**Figure 4e**), most of the self-assembled structures are irregular aggregates with only a few porous flower-like microparticles distributed randomly. With the increasing of β-configuration, D-GlcSE40/60 (**Figure 4f**) exhibit more porous microparticles. When β-configuration dominant the content, mature and independent solid microparticles can be obtained (**Figure 4g** and **4h**). Besides, in comparison of microparticles from D-GlcSE20/80 (**Figure 4g**) and D-GlcSE03/97 (**Figure 4h**), the more β-configuration they have, the bigger size and smoother morphology the microparticles will be obtained (**Figure 4i**). Similar trend can also be found in L-GlcSE with diverse α/β ratios (**Figure S3**). D-GlcSE with diverse α/β ratios were further measured by DSC and SAXS. According to the DSC heating curves (**Figure 4j**), D-GlcSE03/97 with 97% β-configuration exhibits the highest melting temperature (T_m=84°C), while GlcSE70/30 with 70% α-configuration shows the T_m of 65°C. Similarly, D-GlcSE03/97 with 97% β-configuration exhibits the highest T_c of 62°C, while D-GlcSE70/30 with 30% β-configuration has the lowest T_c of 34°C, see **Figure 4k**. Interestingly, two peaks emerge in the DSC cooling curves of D-GlcSE40/60 and D-GlcSE 20/80. This can be explained by the discrepant crystallization properties of α/β configurations: the lower T_c is from α-configuration, while the higher one is from β-configuration. SAXS measurement was also employed to understand the crystallization properties of the D-GlcSE with diverse α/β ratios. As shown in **Figure 4l**, all samples exhibit similar SAXS patterns of 4 Bragg peaks, which show the semi-crystalline nature of the samples in two-dimensional substructures. The ratio of the Bragg reflexes of q1/q2/q3 is 1:2:3, which results in a lamellar packing with a repeating distance of 5.0 nm (D-GlcSE70/30), 5.0 nm (D-GlcSE40/60), 4.8 nm (D-GlcSE20/80) and 4.8 nm (D-GlcSE03/97), respectively. The sharpness of the peaks is most pronounced for D-GlcSE03/97, compared to D-GlcSE with other α/β ratios. Besides, with more α-configuration inside, the 3rd peak in SAXS (marked in **Figure 4l**) exhibit

an obvious shoulder, which represents the different crystallization properties from α/β-configuration.

How aging temperature, concentration and cooling rate affect the self-assembly

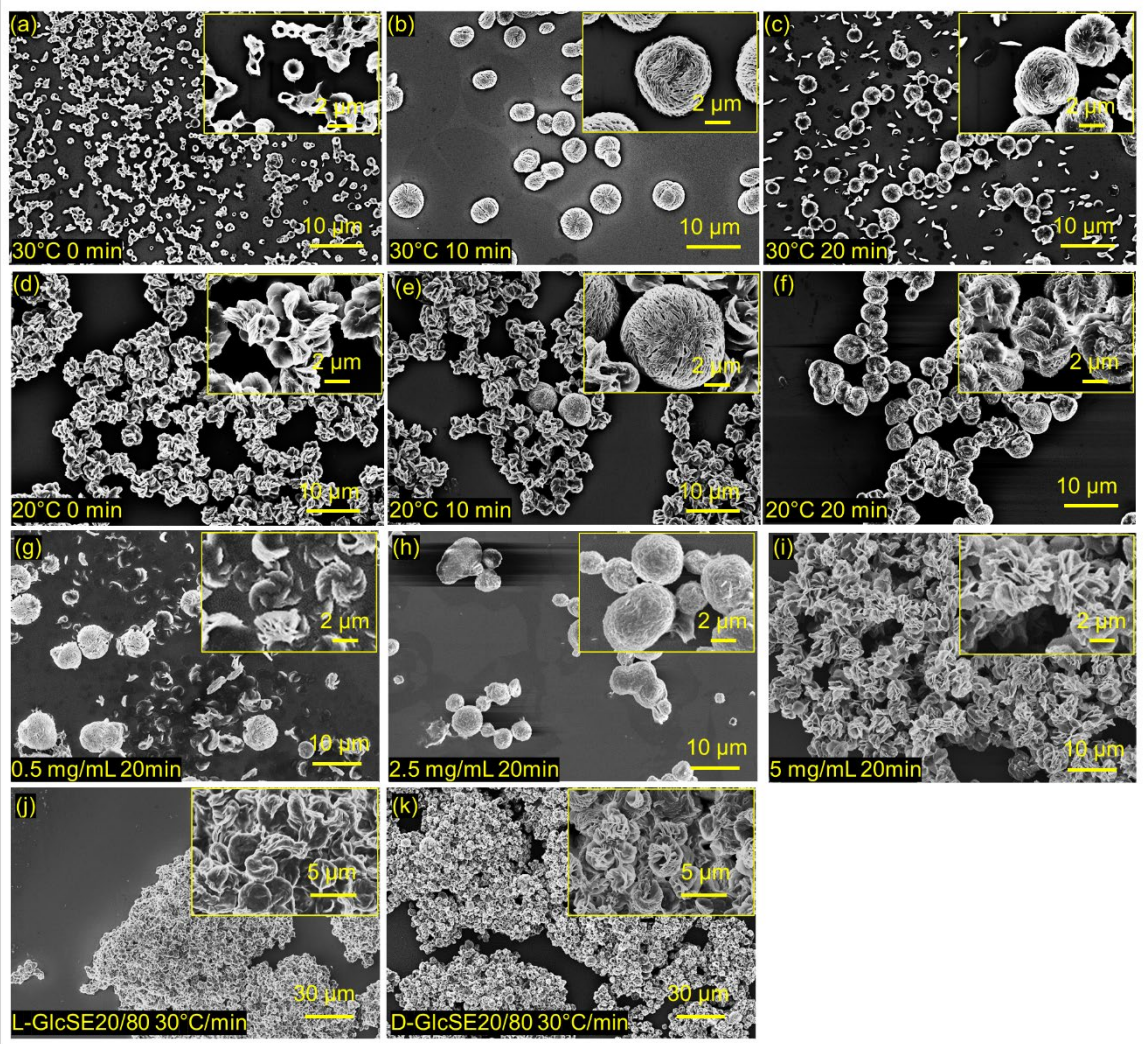

Figure 5. SEM images of the precipitates formed from D-GlcSE20/80 under diverse conditions. SEM images of self-assembled microparticles from D-GlcSE20/80 prepared with the concentration of 1 mg/mL from 60°C to 25°C, cooling rate of 1 °C/min, **a-c)** aging temperature at 30°C for diverse time; **d-f)** aging temperature at 20°C for diverse time. **g-i)** SEM images of self-assembled microparticles from D-GlcSE20/80 prepared with diverse concentrations from 60°C to 25°C, cooling rate of 1 °C/min and aging time of 20 min; **j and k)** SEM images of microparticles prepared from L-GlcSE20/80 and D-GlcSE20/80 with the concentration of 10

mg/mL, cooling rates of 30°C/min from 60°C to 10°C and aged at 10°C for 2 hours. The insets show the enlarged microparticles.

The aging processes at other temperatures, 30°C (**Figure 5a-c**) and 20°C (**Figure 5d-f**) were also studied with different aging times. When aging at 30°C for 0 min, the precipitates tend to form a ring-shape prototype of microparticles. With the increase of aging time, round-shape microparticles were obtained. On the contrary, aging at 20°C can easily promote the formation of irregular aggregates, which can be seen as the overgrown petals. However, neither of them can form chirality. Diverse concentrations were also studied including 0.5, 2.5 and 5 mg/mL. It can be seen that when using the concentration of 0.5 mg/mL, two extremes representing the prototype of chiral microparticles and the over-grown microparticles were obtained. When the concentration is 2.5 mg/mL, only over-grown can be achieved. However, when the concentration reached to 5 mg/mL, irregular petal-shaped aggregates can be observed. Furthermore, beside the lower cooling rate of 1 °C/min, higher cooling rate of 30 °C/min was also studied, both for D- and L-GlcSE20/80. Compare the morphology of the aggregates in **Figure 5j** with **5k**, it turns out that superstructures from D- and L-GlcSE20/80 exhibit similar but smaller size of aggregates and prototype of the chirality. On the contrary, those from lower cooling rate (1 °C/min) show solid morphology with bigger size of distribution.

Discussion

Based on the mentioned results, as enantiomers, D/L-GlcSE molecules are absolutely mirror-imaged. Thus, the mirror-imaged, cookie-shaped microparticles are resulted from the D- and L-configuration. By controlling the aging time, we can observe that the self-assembly is start from the formation of petal-shaped structures (0 min). Then, molecules continue growing on the formed petals with displacements (10 min). The final sophisticated handed microparticles (20 min) exhibit a displacement of around 6° anti-clockwise and clockwise in left- and right-handed chiral superstructures. However, with the aging time over 40 min, the handedness of the microparticles disappeared and the over-grown microparticles were achieved. The α configuration leads to irregular aggregates, which show worse thermal and crystallization

properties, while mature round smooth microparticles with better thermal and crystallization properties are beneficial from β configuration. Axially stretched α configuration improves the difficulties of stacking of MSSE molecules during self-assembly, while better stacking is beneficial from equatorially stretched β configuration. However, only when appropriate number of bonds stretching axially/equatorially (α/β of 20/80) can result in chirality in microparticles.

Furthermore, it has been verified that higher concentration and longer aging time can promote the formation of complete and mature microparticles. Besides, aging at 30°C facilitate the degree of super-cooing for the nucleation of the ring-shaped growing center, while aging at 20°C may lead to the extra degree of super-cooing and dominate the formation of petal-shaped units. However, only aging temperature of 25°C is best for the balance of nucleation and growth of the formation of chiral microparticles.

In conclusion, monosaccharide esters with 5 side chains and 96% bonds stretched equatorially can lead to the formation of chiral microparticles, while those with 5 side chains and around 74% bonds stretched equatorially result in flower-like microparticles. These can be explained by the displacement during molecular stacking. Then, amplification executed in the hierarchical superstructures. Thus, our results provide a new idea and method to design and control the superstructures with chiral, solid and porous morphology by simply adapting the bond configuration in the sugar rings. These findings can facilitate the future study and application of superstructures with solid, chiral and flower-like morphology under certain needs.

Methods

Materials. D-glucose were purchased from VWR International BVBA (Leuven, Belgium). L-glucose and stearoyl chloride (90%) was purchased from Sigma-Aldrich (Steinheim, Germany). Pyridine (99%) was got from abcr GmbH (Karlsruhe, Germany). Chloroform (99.5%), acetone and ethyl acetate were obtained from Th. Geyer (Hamburg, Germany). All the chemicals were used as received without further purification.

Synthesis of D/L-GlcSE. For the synthesis of D/L-GlcSE ,1 g of D/L-glucose was dispersed in 30 mL of pyridine and the mixture was heated to 100°C. Then, 21.00 mL of stearoyl chloride was added into the mixture, while the system was purged with nitrogen gas. After stirring at 100°C for 1 h, the reaction mixture was immediately poured into 300 mL acetone. After that, the

mixture was kept in the fridge at 4°C for at least 6 h. The precipitate was separated by centrifugation at 4°C and purified through multiple washing by dissolution in chloroform and precipitation in acetone at 4°C. Finally, D/L-GlcSE was obtained after drying under vacuum condition at 25°C.

Preparation of D-GlcSE with diverse α/β ratio. First, 50 mL of THF was added into the obtained D-GlcSE prepared from 1 g of glucose and the mixture was stirred for 10 min. Then, the mixture was separated into two phases: dissolved and undissolved parts. After filtration, the dissolved part was named as fraction 1 (F1), while another 50 mL of THF was added into the undissolved part. After stirring for 10 min, this mixture can also be separated as dissolved part, named as fraction 2 (F2) and undissolved part. The same procedure was further repeated for another 3 more times to the undissolved parts to obtain fraction 3, 4, 5 and 6 (F3, F4, F5 and F6).

Self-assembly of D/L-GlcSE in ethyl acetate. First, D/L-GlcSE were dissolved into ethyl acetate at 60°C with the concentration of 1 or 10 mg/mL. Then, the temperature was decreased to 25°C or 10°C with the cooling rate of 1 or 30 °C/min by using a temperature controller. After the specific aging time, a drop of each solution was pipetted onto Si-wafer and dried under ambient conditions.

Sample characterization.

Nuclear magnetic resonance (NMR) was recorded at room temperature on a Bruker DRX 500 spectrometer (Bruker, Biospin GmbH, Ettlingen) using chloroform-d as the solvent.

Fourier transform infrared spectroscopy (FTIR) was conducted on an Alpha FTIR Spectrometer (Bruker) at room temperature between 4000 and 600 cm^{-1} with a resolution of 4 cm^{-1}. The samples were measured twice with 32 scans and an average spectrum was then generated for each sample.

Scanning electron microscopy (SEM) images of the particles were obtained on a LEO Supra-35 high-resolution field emission scanning electron microscope (Carl Zeiss AG, Germany). Before SEM measurement, the sample surface was coated with a 10 nm layer of carbon. Samples were measured under ambient conditions with the electron voltage of 5 kV.

Dynamic Light Scattering (DLS). For the size and size distribution measurement of particles, the dynamic light scattering analysis was implemented on a Zetasizer Nano ZS instrument (Malvern Ltd, UK). The thoroughly cleaned quartz cuvette (Starna, Pfungstadt, Germany) filled with 1 mL

of particle dispersions was used for the measurement. Each sample was processed from 60°C to 10°C and scanned three times at every 5°C, then the average values were taken as the final result.

Differential scanning calorimetry (DSC) measurements of 8~10 mg sample were recorded on a NETZSCH/DSC/200/F3/Maia (NETZSCH, Germany) between 20°C and 100°C with a heating rate of 10 K/min. Dried N_2 gas was purged with a constant flow rate (20 mL/min) during the measurement.

Thermogravimetric analysis (TGA) was carried out on a NETZSCH TG/209/F1/Iris (NETZSCH, Germany) between 100°C and 600°C with a heating rate of 10 K/min under constant nitrogen flow of 20 mL/min.

Small angle X-ray scattering (SAXS) was performed using the small-angle X-ray system "Double Ganesha AIR" (SAXSLAB, Denmark). The X-ray source is a rotating anode (copper, MicoMax 007HF, Rigaku Corporation, Japan) providing a micro-focused beam. The data were recorded by a position sensitive detector (PILATUS 300K, Dectris). To cover the range of scattering vectors q between 0.004-2.0 $Å^{-1}$ different detector positions were used. The scattering vectors q is given by

$$q = |\vec{q}| = \frac{4\pi}{\lambda}\sin\left(\frac{\theta}{2}\right) \quad (1),$$

where $\boldsymbol{\lambda}$ is the wavelength and $\boldsymbol{\theta}$ is the scattering angle. The circularly averaged data were normalized to incident beam, sample thickness and measurement time before the subtraction of the background (solvent).

Data availability

The data that support the findings of this study are available from the corresponding authors upon reasonable request. Source data are provided with this paper.

References

1 Abuaf, M. & Mastai, Y. Synthesis of Multi Amino Acid Chiral Polymeric Microparticles for Enantioselective Chemistry. *Macromolecular Chemistry and Physics* **221**, 2000328, doi:https://doi.org/10.1002/macp.202000328 (2020).

2 He, C. *et al.* Highly enantioselective photo-polymerization enhanced by chiral nanoparticles and in situ photopatterning of chirality. *Nature Communications* **11**, 1188, doi:10.1038/s41467-020-15082-6 (2020).

3 Jiang, W., Yi, X. & McKee, M. D. Chiral biomineralized structures and their biomimetic synthesis. *Materials Horizons* **6**, 1974-1990, doi:10.1039/C9MH00431A (2019).

4 Kravets, N., Aleksanyan, A., Chraïbi, H., Leng, J. & Brasselet, E. Optical Enantioseparation of Racemic Emulsions of Chiral Microparticles. *Physical Review Applied* **11**, 044025, doi:10.1103/PhysRevApplied.11.044025 (2019).

5 Li, M. *et al.* Chiral Nanoparticles with Full-Color and White CPL Properties Based on Optically Stable Helical Aromatic Imide Enantiomers. *ACS Applied Materials & Interfaces* **10**, 8225-8230, doi:10.1021/acsami.8b00341 (2018).

6 Naaman, R., Paltiel, Y. & Waldeck, D. H. Chiral molecules and the electron spin. *Nature Reviews Chemistry* **3**, 250-260, doi:10.1038/s41570-019-0087-1 (2019).

7 Jiang, W. *et al.* Chiral acidic amino acids induce chiral hierarchical structure in calcium carbonate. *Nature Communications* **8**, 15066, doi:10.1038/ncomms15066 (2017).

8 Nakanishi, T. *et al.* Flower-Shaped Supramolecular Assemblies: Hierarchical Organization of a Fullerene Bearing Long Aliphatic Chains. *Small* **3**, 2019-2023, doi:https://doi.org/10.1002/smll.200700647 (2007).

9 Jiang, W., Pacella, M. S., Vali, H., Gray, J. J. & McKee, M. D. Chiral switching in biomineral suprastructures induced by homochiral l-amino acid. *Science Advances* **4**, eaas9819, doi:10.1126/sciadv.aas9819 (2018).

10 Hernández, R. J., Mazzulla, A., Pane, A., Volke-Sepúlveda, K. & Cipparrone, G. Attractive-repulsive dynamics on light-responsive chiral microparticles induced by polarized tweezers. *Lab on a Chip* **13**, 459-467, doi:10.1039/C2LC40703E (2013).

11 Cipparrone, G., Mazzulla, A., Pane, A., Hernandez, R. J. & Bartolino, R. Chiral Self-Assembled Solid Microspheres: A Novel Multifunctional Microphotonic Device. *Advanced Materials* **23**, 5773-5778, doi:https://doi.org/10.1002/adma.201102828 (2011).

12 Tkachenko, G. & Brasselet, E. Optofluidic sorting of material chirality by chiral light. *Nature Communications* **5**, 3577, doi:10.1038/ncomms4577 (2014).

13 Donato, M. G. *et al.* Polarization-dependent optomechanics mediated by chiral microresonators. *Nature Communications* **5**, 3656, doi:10.1038/ncomms4656 (2014).

14 Shejul, D. A. *et al.* Aggregation-induced emission characteristics and solvent triggered hierarchical self-assembled chiral superstructures of naphthalenediimide amphiphiles. *New Journal of Chemistry* **44**, 1615-1623, doi:10.1039/C9NJ05137F (2020).

15 Nakashima, N. *et al.* Helical Superstructures of Fullerene Peapods and Empty Single-Walled Carbon Nanotubes Formed in Water. *The Journal of Physical Chemistry B* **109**, 13076-13082, doi:10.1021/jp050958m (2005).

16 Shang, Y. *et al.* Orientation Ordering and Chiral Superstructures in Fullerene Monolayer on Cd (0001). *Nanomaterials* **10**, 1305 (2020).

17 Liu, N. *et al.* Shape and structure controlling of calcium oxalate crystals by a combination of additives in the process of biomineralization. *RSC Advances* **8**, 11014-11020, doi:10.1039/C8RA00661J (2018).

18 Moussa, H. *et al.* Selective Crystal Growth Regulation by Chiral α-Hydroxycarboxylic Acids Improves the Strength and Toughness of Calcium Sulfate Cements. *ACS Applied Bio Materials* **3**, 8559-8566, doi:10.1021/acsabm.0c00918 (2020).

19 Huang, H., Yang, W. & Deng, J. Chiral, fluorescent microparticles constructed by optically active helical substituted polyacetylene: preparation and enantioselective recognition ability. *RSC Advances* **5**, 26236-26245, doi:10.1039/C4RA16466K (2015).

20 Zhang, H., Qian, G., Song, J. & Deng, J. Optically Active, Magnetic Microparticles: Constructed by Chiral Helical Substituted Polyacetylene/Fe3O4 Nanoparticles and Recycled for Uses in Enantioselective Crystallization. *Industrial & Engineering Chemistry Research* **53**, 17394-17402, doi:10.1021/ie503114z (2014).

21 Zhao, Y., Zhang, X., Li, W. & Zhang, A. Stimuli-responsive poly(phenyl acetylene) microparticles with tunable chirality. *European Polymer Journal* **118**, 275-279, doi:https://doi.org/10.1016/j.eurpolymj.2019.05.054 (2019).

Acknowledgements

K.Z. thanks Deutsche Forschungsgemeinschaft with the grant ZH546/3-1 for the financial support and Georg-August-University of Goettingen for the Department Start-up funding. Y.Y. thanks the China Scholarship Council (CSC) for financial support. Q. T. acknowledges the financial support by the Deutsche Forschungsgemeinschaft under grant Mu1674/15-2. The

simulations were performed at the GWDG Goettingen, the HLRN Goettingen, and the von-Neumann Institute for Computing, Juelich, Germany.

Competing interests

The authors declare no competing interests.

Additional information

Supplementary information is available for this paper at

Correspondence and requests for materials should be addressed to K.Z.

Peer review information Nature Communications thanks xx for their contribution to the peer review of this work. Peer reviewer reports are available.

Reprints and permission information is available at

Publisher's note Springer Nature remains neutral with regard to jurisdictional claims in

published maps and institutional affiliations.

Supplementary Information for:

Chiral hierarchical structure in glucose stearoyl esters and the role of bond configuration

Yawen Yao[1#], Qiyun Tang[2#], Sabine Rosenfeldt[3], Marcel Krüsmann[4], Matthias Karg[4], Kai Zhang[1*]

Structural characterization of L-glucose stearoyl esters (L-GlcSE)

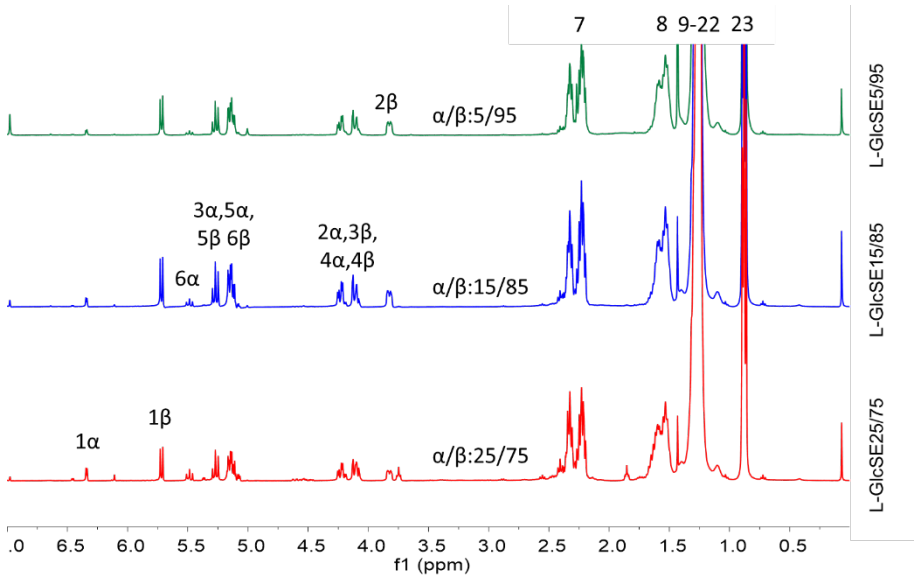

Figure S1: ^{1}H NMR spectra of the obtained L-GlcSE with 3 diverse α/β ratios, to be precise, α/β ratio of 25/75, 15/85 and 5/95 recorded in deuterated chloroform.

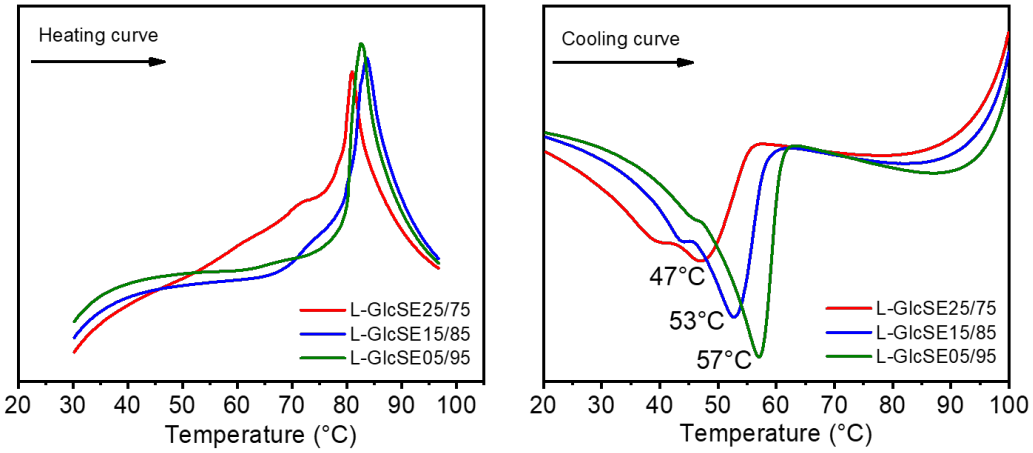

Figure S2: Heating and cooling DSC curves of L-GlcSE25/75, L-GlcSE 15/85 and L-GlcSE 5/95.

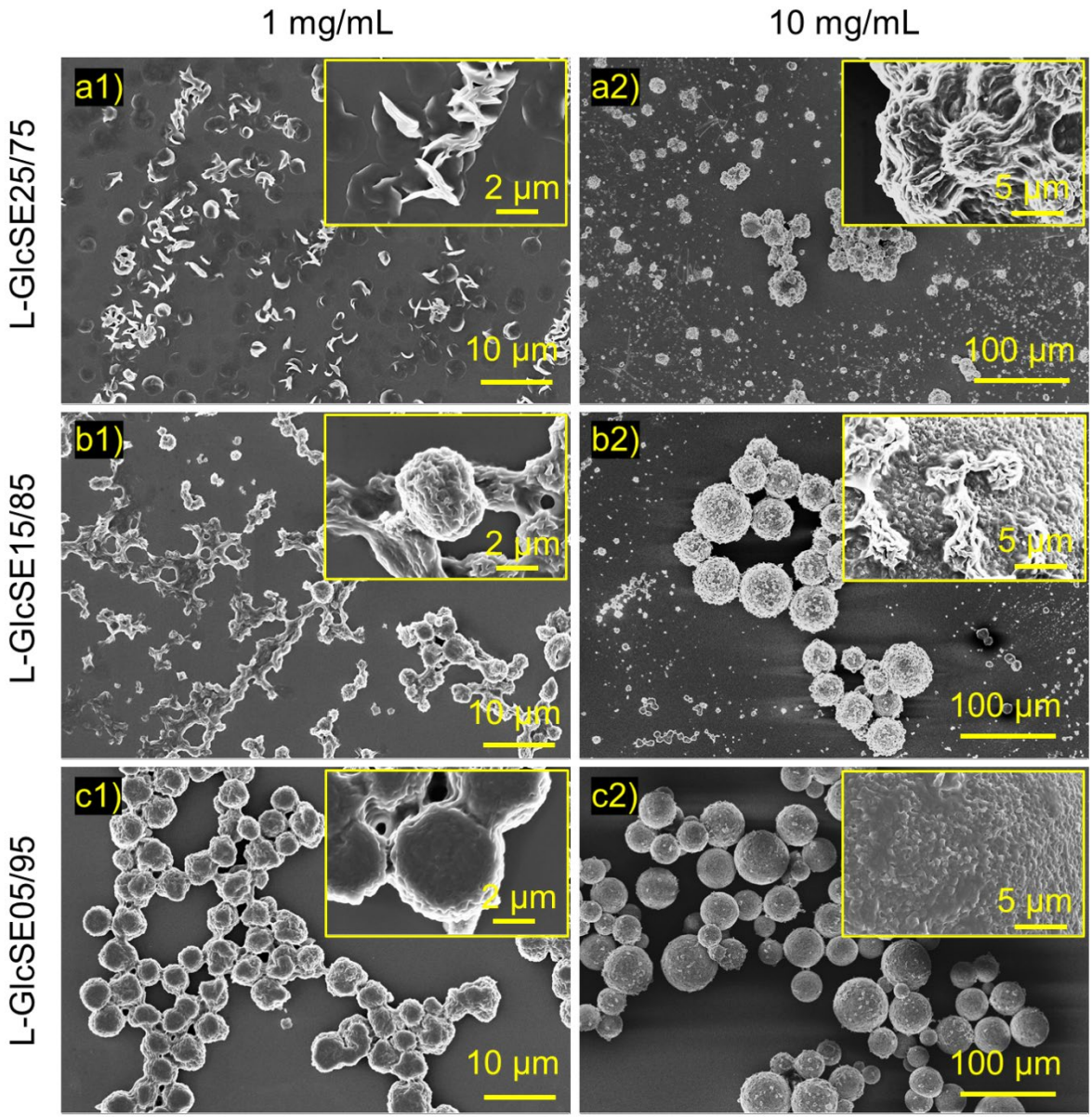

Figure S3: SEM images of the self-assembled aggregates of L-GlcSE with the α/β ratio of a) 25/75, b) 15/85 and c) 05/95 prepared with the concentration of 1) 1 mg/mL from 60°C to 25°C and 2) 10 mg/mL from 60°C to 10°C. The insets are the zoom-in SEM images.

Publication 3

Single Bond Bending on Monosaccharide Rings enables Flower-Like Particles via Liquid-Liquid Phase Separation

Yawen Yao, [a]# Qiyun Tang, [b]# Sabine Rosenfeldt, [c] Kai Zhang[a]*

[a] Y. Yao, Prof. Dr. K. Zhang.
Wood Technology and Wood Chemistry, Dept. Wood Technology and Wood-based Composites, Georg-August-University of Goettingen
Büsgenweg 4, 37077 Göttingen, Germany.

[b] Dr. Q. Tang.
Institute of Theoretical Physics, Georg-August-University of Goettingen
Friedrich-Hund-Platz 1, 37077 Göttingen, Germany.

[c] S. Rosenfeldt.
Department of Chemistry and Bavarian Polymer Institute, University of Bayreuth
Universitätsstraße 30, 95447 Bayreuth, Germany

# These authors contributed equally.

Corresponding authors:
* E-mail: kai.zhang@uni-goettingen.de

Manuscript

Abstract

Connecting diverse moieties on backbone molecules is a common strategy to modify the morphology of assembled nano/microparticles, e.g. specific microsized flower-like particles (FLP) from alkanoylated cellulose or fullerene based on partially crystallized side chains, but the function of backbone molecules remains unclear. Herein, stearoylated derivatives of four monosaccharides (D-glucose, D-galactose, D-mannose and D-xylose) with very similar molecular configurations (only difference at one position of monosaccharide rings between each sugar and D-glucose), are employed to study the effect of core structures on the formation of microparticles with varied morphologies. The configurational discrepancies of the sugar rings cause different thermal, colloidal properties of these sugar derivatives, and morphologies of obtained microparticles. While the stearolyated D-galactose and D-mannose with only one C-O-bond axially sticking out of the sugar ring plane generate FLP, stearolyated D-glucose and D-xylose with all the C-O-bonds directing equatorially within the sugar ring plane only form solid microparticles. Furthermore, FLP containing thin nanoplates that are formed upon cooling the solutions of stearoylated D-galactose and D-mannose from >55 to 10°C, undergo similar formation kinetics during the initial liquid-liquid phase separation as the solid microparticles formed by stearoylated D-glucose and D-xylose.

Introduction

Flower-like particles (FLP) are hierarchical micro- or nanoparticles featuring thin sheets as "petals" that are arranged into nearly spherical particles, similar to a flower. Their high surface area and dimensional stability enable enhanced enzymatic activity[1], optical response[2], and further widespread potential applications in bioelectronics[3], optoelectronics[4], drug delivery[5], sensors[6], and catalysis[7]. These complex hierarchical structures can be fabricated from inorganic compounds, such as CuO[2], MnO_2[8], fullerene[9], or inorganic-organic composites, for instance proteins/enzyme with the presence of metallic oxides[1, 10], or even the organic species, for example polyimides[11], polyaniline[12], multi-aromatic rings[13], and nucleosides[14]. Diverse interactions between distinct components, such as van der Waals interactions[2, 8], electrostatic interactions[1, 10], π-π stacking[13], hydrogen bonding[14], and the interplay of these interactions[9] together with various molar ratios between different species[12] give rise to the growth of FLP.

Among others, long aliphatic side chains promoted the formation of petal structures of the FLP by forming the semicrystalline nanosheets[9, 15]. For instance, cellulose stearoyl esters generated FLP via side chain crystallization induced by solvent exchange[15] or temperature decrease[16]. This is similar to the FLP prepared with a fullerene derivative containing three hexadecyloxy aliphatic chains via side chain self-assembly[9]. Here, both cellulose and fullerene were acting as the center cores, whereas the crystallizing long side chains linking to these cores are crucial for the formation of FLP. Further experiments showed that molecules with other backbones, such as polyvinyl or glycerol stearoyl esters could not form FLP under equal conditions[17]. Considering the huge configurational differences between cellulose[15-16] and fullerene[9] as well as other backbones that are feasible for the formation of FLP[10-14], it is still unclear whether and how the configurations of core structures affect the formation of FLP.

In this study, we found for the first time that certain monosaccharides can be core components for FLP and especially, the only configuration difference at one position on the monosaccharide rings strongly affects the morphologies of obtained microparticles and therefore the formation of FLP. D-monosaccharide stearoyl esters (D-MSSEs) from four monosaccharides (glucose, xylose, galactose, and mannose) with highly similar stereo-structures were synthesized after esterifying all hydroxyl groups with the same stearoyl groups as side chains (**Figure 1**). Resulting D-glucose

stearoyl ester (D-GlcSE), D-xylose stearoyl ester (D-XylSE), D-galactose stearoyl ester (D-GalSE) and D-mannose stearoyl ester (D-ManSE) were used to study the effect of core configurations on the formation of diverse microparticles, in particular FLP, and to clarify their growth kinetics at early stages during the temperature cooling.

Results and Discussion

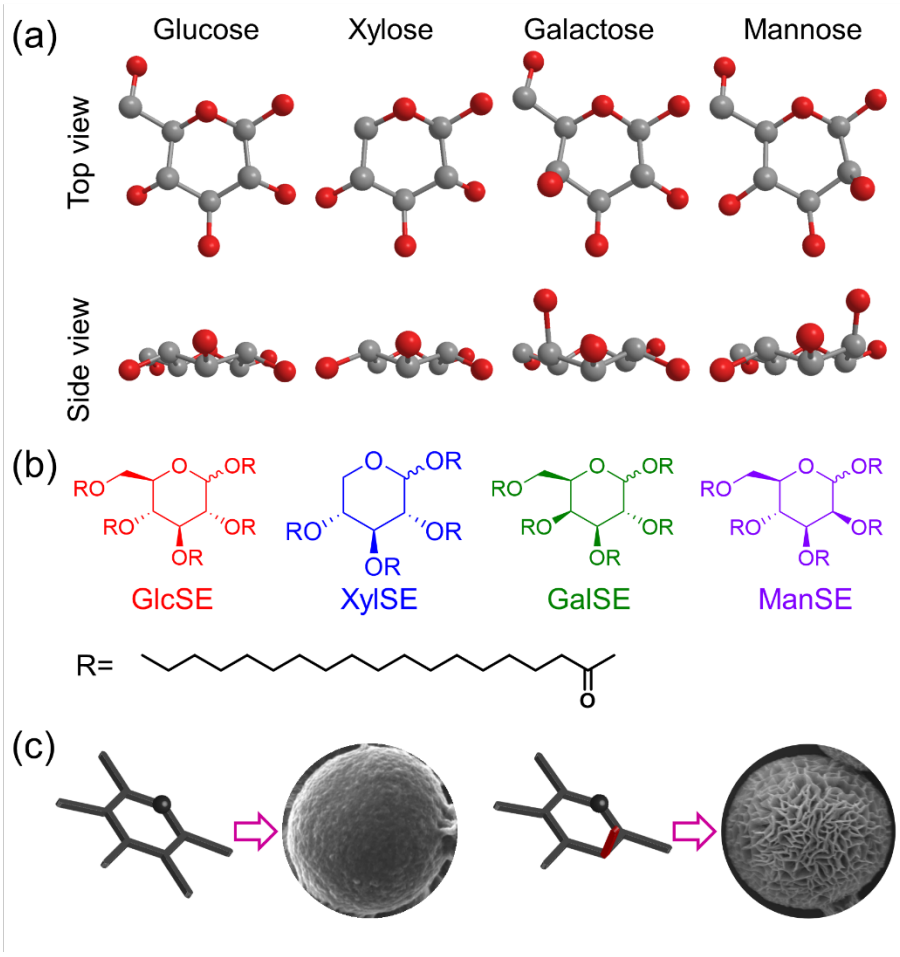

Figure 1. (a) Stereo-structures of D-glucose, D-xylose, D-galactose and D-mannose as the top and side views. (b) Structural formula of D-glucose stearoyl ester (D-GlcSE), D-xylose stearoyl ester (D-XylSE), D-galactose stearoyl ester (D-GalSE) and D-mannose stearoyl ester (D-ManSE). R represents stearoyl group. (c) Schematic illustration for the formation of filled microparticle from D-GlcSE or D-XylSE and FLP from D-GalSE or D-ManSE with one bond sticking out of the sugar ring plane.

The structures of the 4 D-MSSEs were characterized by nuclear magnetic resonance (NMR) and Fourier transform infrared spectroscopy (FTIR) as shown in supplementary information (**Figure S1-S4**). The three-dimensional stereo-structures of these 4 sugar rings are illustrated in **Figure 1a** with the top and side views, and their stearoyl esters are shown in **Figure 1b**. It should be noted that D-XylSE only contains 4 side chains, while the other 3 D-MSSE molecules bear 5 side chains linked to the sugar backbone. Moreover, D-GlcSE and D-XylSE have all the bonds connecting with the side chains on the same plane of the sugar rings, whereas D-GalSE and D-ManSE have one bond axially sticking out of the sugar ring plane. These four D-MSSEs were dissolved in ethyl acetate at 80°C, and the temperatures of obtained solutions were exactly decreased toward 10°C using a temperature controller. The concentration of D-MSSEs in ethyl acetate was scoped at first and a sufficiently high concentration of at least 10 mg/ml was required for D-GalSE and D-ManSE to generate uniform FLP with nanoplates as structuring components (**Figure 1c**), while lower concentrations of 1 mg/ml only led to nonuniform and incomplete FLP. In comparison, D-GlcSE and D-XylSE predominantly formed solid, filled microparticles at 10 mg/ml (**Figure 1c**), while they only occasionally formed porous microparticles with the majority as nearly filled microparticles at lower concentrations of 1 mg/ml (**Figure S5**).

Then, the D-MSSEs solutions in ethyl acetate of 10 mg/ml were analyzed using dynamic light scattering (DLS) by recording the results with 5°C intervals, in order to detect the initial particle formation of each D-MSSE during the temperature decrease from 80°C to 10°C. Between 80 and 60°C, the DLS measurements of the solutions showed no signals, indicating the full dissolution of D-MSSE molecules. DLS signals emerged at 55°C for the solutions of all four D-MSSEs (**Figure 2**) and one can clearly see the peaks representing a length scale of around 100 nm. These peaks indicate the formation of initial, dense liquid droplets, which are metastable with respect to the low-concentration solutions and the crystalline solids. Similar behavior was also observed in the crystallization of lumazine synthase from solution[18], where the short lifetime of the droplets hinders their growth toward detectable dimensions for liquid-liquid phase separation. Once the temperature is low enough, the crystalline nuclei formed within the dense liquid droplets will grow and ripen toward crystalline solids. With steady temperature decrease before the precipitation temperature, these droplets maintained their sizes for all D-MSSEs in their

solutions. Once the temperature is lower than the precipitation temperature, e.g. at 25°C for D-GlcSE solution (**Figure 2a**), DLS curves show the formation of structures of a few microns. Such precipitation temperatures vary and lie at 15°C for D-GalSE (**Figure 2c**) and D-ManSE (**Figure 2d**). In comparison, D-XylSE microparticles exhibited solid properties by precipitating at around 31°C, instead of forming flakes and thus cloudy suspension according to their photo images in solutions (**Figure 2b**). These different precipitation temperatures can be attributed to the different solubility of D-MSSE molecules in solutions, distinct densities of dense droplets and growth rates of the crystalline nuclei within the droplets, which are chiefly dictated by their molecular configurations (**Figure 1a**).

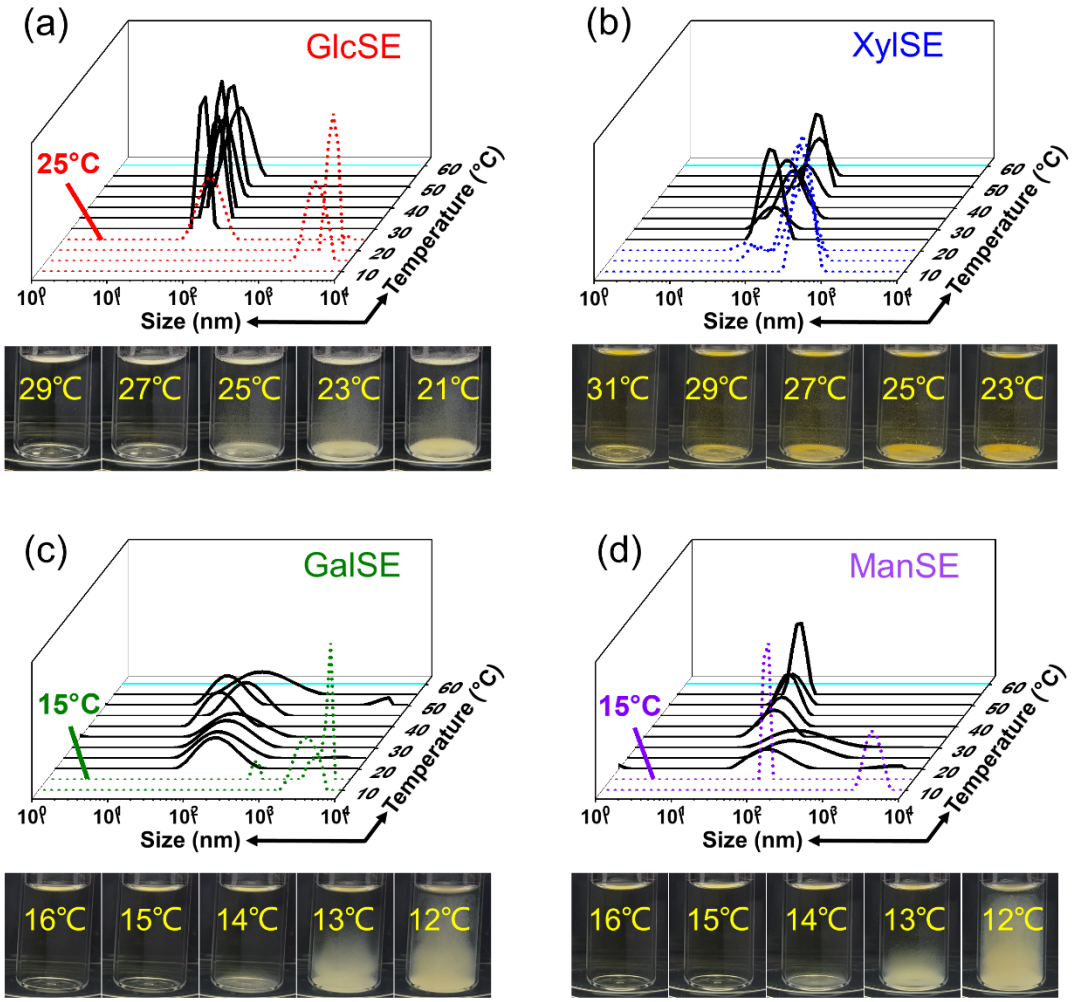

Figure 2. DLS curves of the solutions of (a) D-GlcSE, (b) D-XylSE, (c) D-GalSE, and (d) D-ManSE in ethyl acetate at 10 mg/mL during the cooling process of 1 °C/min. The bottom images in each panel show the photos of the solutions at various temperatures.

The existence of the dense liquid droplets during the cooling process indicates a two-step nucleation mechanism in solutions, which have been confirmed by many simulations and experiments in the past two decades[18-19]. This mechanism predicts that rather than nucleating directly from dilute solutions according to the classical nucleation theory, the solutes first form dense liquid droplets of a few hundred nanometers, from which the crystalline nuclei appear and grow toward large-scale particles. The dense liquid droplets were experimentally observed[18] and a two-step mechanism was proven to be free-energy favorable compared to the classical nucleation theory[19a-19b]. In this mechanism, the liquid-liquid phase separation plays a dominant role in the formation of dense liquid droplets at the early stages during the cooling process.

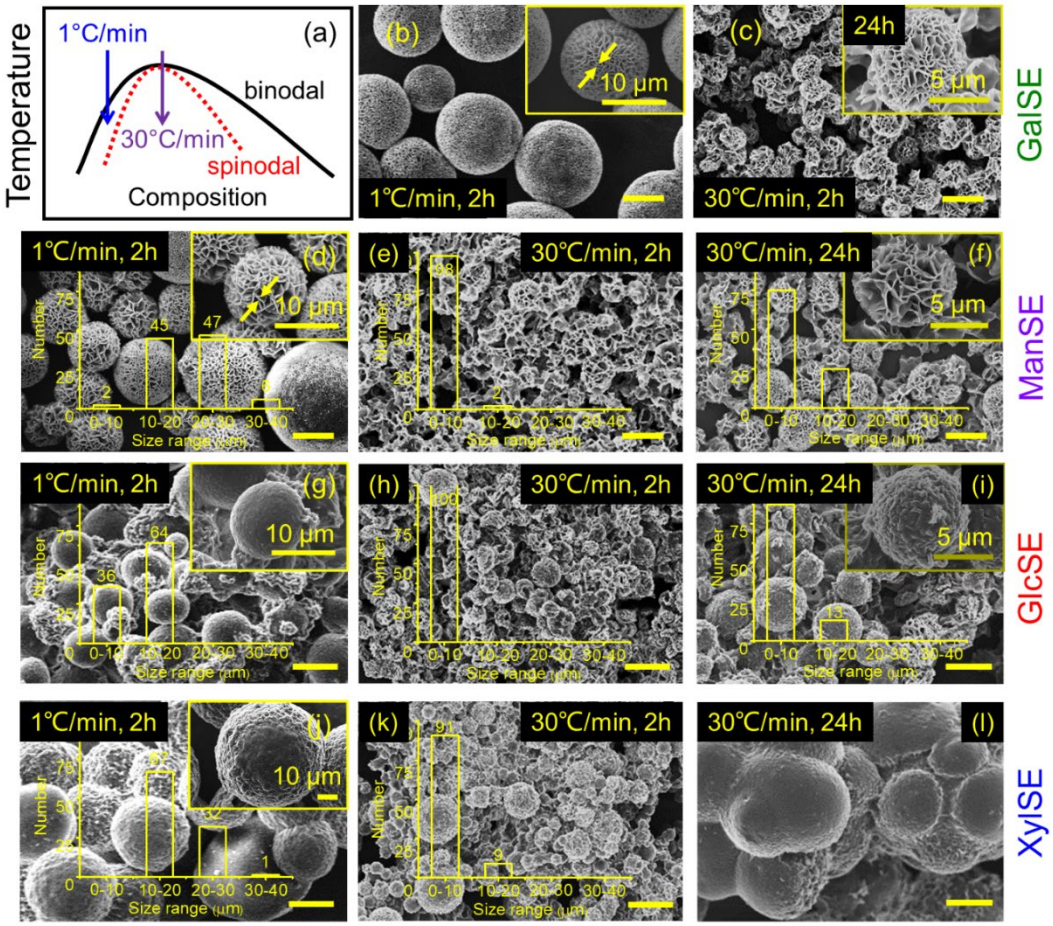

Figure 3. (a) Illustrative temperature vs. composition phase diagram of D-MSSE molecules in solution. The black solid and red dotted lines correspond to the binodal and spinodal lines. The blue and purple arrows show two different paths during the cooling process. (b)-(c) SEM images of D-GalSE microparticles obtained with the cooling rates of (b) 1 °C/min and (c) 30 °C/min, and further aged at 10°C for 2 hours. The inset in panel (b) shows the enlarged microparticles and that in panel (c) shows the enlarged microparticles after 24 hours aging. (d)-(f) SEM images of D-ManSE microparticles obtained at different cooling rates and aging times (see labels). The yellow figures show the size distributions of microparticles, each measured from 100 independent samples. (g)-(i) SEM images and size distributions of D-GlcSE microparticles. (j)-(l) SEM images and size distributions of D-XylSE microparticles. The scale bars in main panels from (b) to (l) represent 10 μm.

Figure 3a shows an illustrative phase diagram of the D-MSSEs solutions at the early stages[20]. A low cooling rate drives the solutions into liquid-liquid coexistence region, where the classical nucleation theory dominates the liquid-liquid phase separation. However, a faster cooling might promote the solution into the unstable region on the phase diagram, where spinodal decomposition determines the liquid-liquid phase separation. To verify this assumption, solutions of D-MSSEs in ethyl acetate at 10 mg/mL were cooled from 80°C to 10°C using two different cooling rates, 1 °C/min and 30 °C/min. Subsequently, obtained microparticles were aged at 10°C for 2 hours, and the precipitated microparticles were measured using SEM. Based on microparticles of D-GalSE in **Figure 3b**, a smaller cooling rate (1 °C/min) led to bigger microparticles with a wider size distribution (10-40 μm). This implies that the crystalline nuclei formed from the dense liquid droplets experienced a classical nucleation process, of which the rare event generated wider size distributions. In comparison, the higher cooling rate (30 °C/min) resulted in smaller microparticles with narrower size distribution (0-10 μm) (**Figure 3c**). These demonstrate that the D-MSSEs solutions were in the unstable region on the phase diagram after the fast-cooling process. In this scenario, the dense liquid droplets were formed following the spinodal decomposition, where only the given modes of fluctuations could grow, giving rise to a narrow size distribution of liquid droplets. The microparticles formed within these narrow-size-distribution droplets were difficult to grow, because the amount of free D-MSSEs molecules in solution became quite low and the further growth of microparticles was hindered. This explains

why the average size of microparticles in **Figure 3c** is smaller than that in **Figure 3b**. Similar behaviors were also observed for the microparticles formed from D-ManSE, D-GlcSE, and D-XylSE (**Figure 3d-3l**).

In particular, the microparticles formed from D-GalSE and D-ManSE show FLP structures at both low and high cooling rates (insets of **Figure 3b** and **3c**, and of **3d** and **3f**). Petal structures with the thickness of 170±100 nm (inset of **Figure 3b**) and 140±90 nm (inset of **Figure 3d**) can be observed. In contrast, D-GlcSE and D-XylSE molecules primarily formed filled microparticles. These observations indicate that the formation of FLP is independent from their process conditions at early stages. It only relied on the molecular configurations of core structures of D-GalSE and D-ManSE, where one bond is protruding perpendicular to the sugar ring plane.

These distinct D-MSSE microparticles were further analyzed by employing DSC, SAXS, XRD, as well as molecular simulations, to measure and calculate the thermal and structural properties (**Figure 4**). First, we focus on the crystalline properties of these microparticles via DSC and molecular simulations. **Figure 4a** illustrates the DSC curves of D-MSSE microparticles, where the heating curve of D-XylSE microparticles demonstrates a melting temperature T_m of 93°C, which is larger than 81°C for D-GlcSE, 60°C for D-GalSE, and 63°C for D-ManSE microparticles. The cooling curves exhibit the crystallization temperatures T_c of the D-MSSE samples and show a similar trend: the D-XylSE microparticles exhibited the highest T_c of 63°C, followed by the 55°C for D-GlcSE, 47°C for D-GalSE, and 49°C for D-ManSE microparticles. The analogous heating and cooling curves of the D-GalSE and D-ManSE microparticles indicate that the position of the axially protruding bonds (whether at C2 or C4) on sugar rings of mannose or galactose do not strongly influence their crystalline properties (**Figure 1**). However, one single stereochemically different bond significantly reduced their feasibility to crystallize and thus led to their lower T_m and T_c, compared to D-GlcSE and D-XylSE.

To clearly demonstrate the relationship between molecular structures of D-MSSE molecules and their crystalline properties, we employed computer simulations to calculate the average crystallinity of distinct D-MSSE molecules (**Figure 4** and **S7-S9**) [21]. The simulations were

performed based on a coarse-grained model of D-MSSE molecules: all the sugar rings are coarse-grained as one monomer, whereas their configuration features are characterized by the co-planar behaviors of the bonds connecting the side chains and sugar rings (see the top panel of **Figure 4b** and **Figure 1a**). Other simulation details are summarized in Supporting Information. We chose the system size of 30×30×30 nm^3 with the monomer density of 0.60/nm^3 (other densities have also been explored, see Supporting Information). The variations of the crystallinity for the D-MSSE molecules are shown in the bottom row of **Figure 4b**. It is clear that the average crystallinity of the D-XylSE is larger than that of the D-GlcSE and D-GalSE, indicating that the D-XylSE is easier to crystallize than other D-MSSE molecules at the same conditions. This is consistent with the DSC results in **Figure 4a**, where the D-XylSE takes the highest melting and crystallization temperatures.

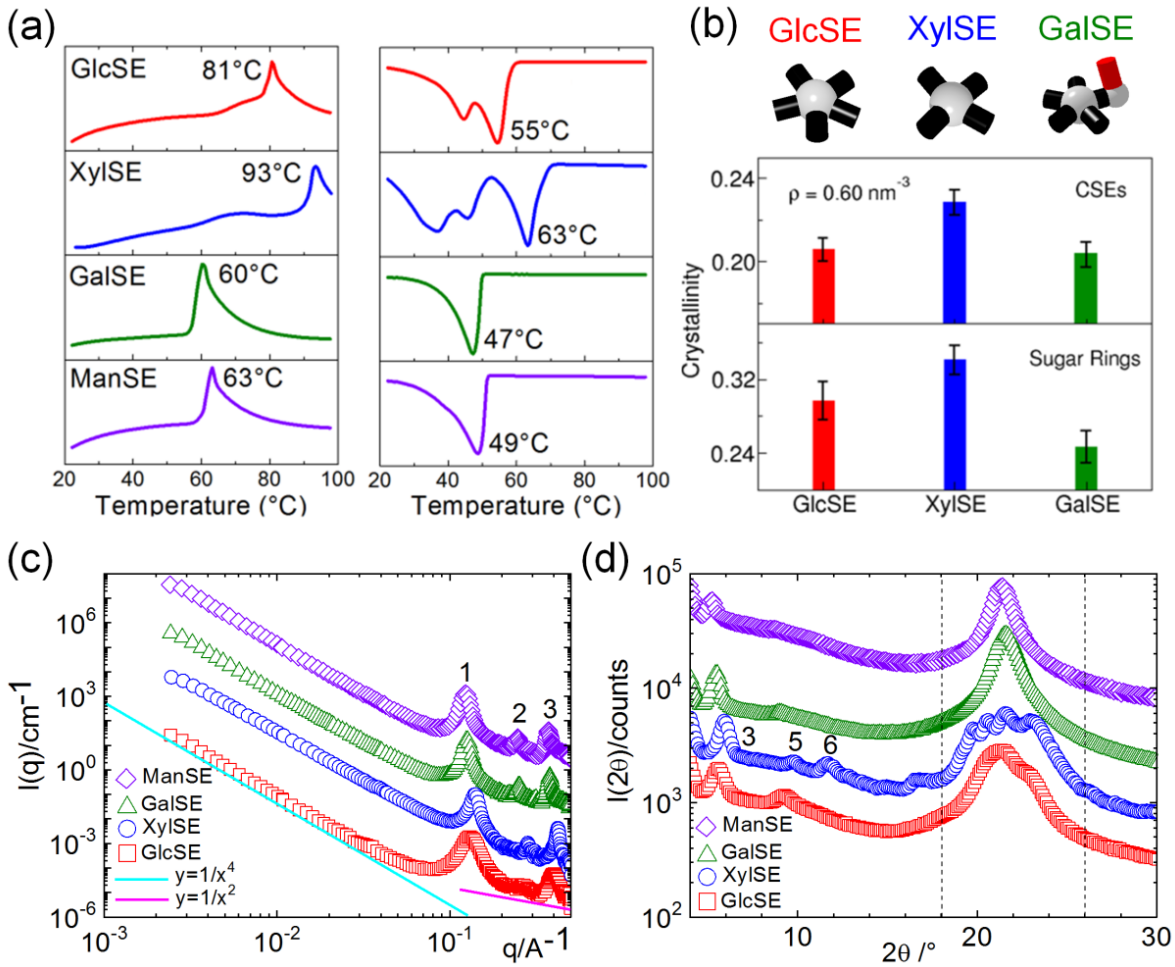

Figure 4. (a) Heating (left) and cooling (right) DSC curves of D-GlcSE, D-XylSE, D-GalSE and D-ManSE microparticles obtained after the precipitation and aging time of 2 hours. (b) Top panel: The coarse-grained structures of D-GlcSE, D-XylSE and D-GalSE molecules in simulation, where the stearoyl chains are not shown. Bottom panel: average crystallinity of melts of 3 D-MSSE molecules and sugar-rings from simulations. (c) SAXS and (d) XRD measurements of D-GlcSE, D-XylSE, D-GalSE and D-ManSE microparticles.

However, given the obvious differences of thermal properties between microparticles of D-GlcSE and D-GalSE (**Figure 4a**), their crystallinities calculated from simulations are closer to each other. To explore the origins of the discrepancies, we measured the crystallinities of the core monomers for sugar rings (see the bottom panel in **Figure 4b**). Results show that the core monomers of D-GlcSE molecules are easier to crystallize than that of D-GalSE molecules, which is consistent with experiments in **Figure 4a**. Therefore, the differences of the thermal properties for D-MSSE microparticles shown in **Figure 4a** can be attributed to different origins: the difference between D-XylSE and D-GlcSE/ D-GalSE is chiefly dictated by the number of side chains, whereas the axially protruding bonds in D-GalSE (or D-ManSE) on the sugar ring hinder the crystallization of the D-MSSE molecules and lower the crystalline and melting temperatures compared to D-GlcSE.

In **Figure 4a**, some additional peaks are emerging on the cooling curves of D-GlcSE and D-XylSE microparticles at lower temperatures. These peaks correspond to the polymorphic crystals formed by D-MSSE molecules, as shown in previous studies, e.g. on the crystallization behaviors of milk fat[22]. To further explore the structural properties of D-MSSE microparticles, we employed the SAXS and XRD methods to measure the powder samples of D-MSSE microparticles. As shown in **Figure 4c**, all D-MSSE microparticles exhibit similar SAXS patterns, showing a q^{-4} scaling law for $q<0.1$ Å^{-1} as expected due to the large dimension of the micrometersized particles (Porod's law). The q^{-2} behavior for $q>0.1$ Å^{-1} hints to the existence of a two-dimensional substructure inside the object. The corresponding Bragg peaks show the semi-crystalline nature of the samples in the two-dimensional substructure. The ratio of the Bragg reflexes of q1/q2/q3 is 1:2:3, which results in a lamellar packing with a repeating distance of 4.6 nm (D-XylSE), 4.8 nm (D-GlcSE), 5.0 nm (D-GalSE) and 5.1 nm (D-ManSE), respectively. The

sharpness of the peaks is most pronounced for D-XylSE, compared to other D-MSSEs. XRD data for the D-MSSEs are given in **Figure 4d**. The packing of neighboring aliphatic chains forming crystallites reflects in the range of 2Θ=18-26°[23], where the D-MSSEs exhibit differences in the number of distinct peaks: D-XylSE (4 well defined peaks, 4.5-3.8Å), D-GlcSE (broad peak with a shoulder, 4.2-3.8Å) and D-GalSE and D-ManSE (both 1 peak, 4.1-4.2Å). These peaks perfectly correspond to the peaks in DSC cooling curves of D-MSSEs in **Figure 4a**. The area of the XRD peaks represents the crystalline areas of D-MSSEs, which also reflects the crystalline ability of D-MSSE molecules. The largest peak area of D-XylSE in **Figure 4d** indicates the best crystalline ability, which is consistent with the DSC measurements and simulation calculations. Therefore, these outlined simulation and experimental results demonstrate a strong relationship between the thermal and structural properties of the D-MSSE microparticles and the configurations of D-MSSE molecules. These results further indicate that the configurational change of one simply bond of D-MSSE molecules induces significant change of their macroscopic properties.

Conclusion

In summary, we demonstrated the formation of diverse microparticles, in particular FLP using D-MSSEs for the first time and the function of the core component during the formation of these microparticles including FLP. We further showed via experiments and simulations to demonstrate that the configurational difference of the bonds connecting the side chains to monosaccharide rings strongly affected the formation of FLP, the surface morphologies of the obtained microparticles and their thermal and structural properties. Our results further demonstrate that stereochemical difference of only one bond on monosaccharide rings enables the formation of FLP, which is independent from their formation kinetics.

Acknowledgements

K.Z. thanks Deutsche Forschungsgemeinschaft with the grant ZH546/3-1 for the financial support and Georg-August-University of Goettingen for the Department Start-up funding. Y.Y. thanks the China Scholarship Council (CSC) for financial support. Q. T. acknowledges the financial support by the Deutsche Forschungsgemeinschaft under grant Mu1674/15-2. The

simulations were performed at the GWDG Goettingen, the HLRN Goettingen, and the von-Neumann Institute for Computing, Juelich, Germany.

Conflict of Interest

The authors declare no conflict of interest.

Keywords: flower-like particles, monosaccharide, stearoyl, liquid-liquid phase separation, configuration

References

[1] J. Ge, J. Lei, R. N. Zare, *Nat. Nanotechnol.* **2012**, *7*, 428-432.

[2] Y. Duan, X. Liu, L. Han, S. Asahina, D. Xu, Y. Cao, Y. Yao, S. Che, *J. Am. Chem. Soc.* **2014**, *136*, 7193-7196.

[3] Q. He, Y. Cui, J. Li, *Chem. Soc. Rev.* **2009**, *38*, 2292-2303.

[4] Y. S. Zhao, H. Fu, A. Peng, Y. Ma, Q. Liao, J. Yao, *Acc. Chem. Res.* **2010**, *43*, 409-418.

[5] D. Peer, J. M. Karp, S. Hong, O. C. Farokhzad, R. Margalit, R. Langer, *Nat. Nanotechnol.* **2007**, *2*, 751.

[6] C. J. Martinez, B. Hockey, C. B. Montgomery, S. Semancik, *Langmuir* **2005**, *21*, 7937-7944.

[7] Z. Bao, M. R. Weatherspoon, S. Shian, Y. Cai, P. D. Graham, S. M. Allan, G. Ahmad, M. B. Dickerson, B. C. Church, Z. Kang, *Nature* **2007**, *446*, 172-175.

[8] G. Li, W. Li, K. Xu, R. Zou, Z. Chen, J. Hu, *J. Mater. Chem. A* **2014**, *2*, 7738-7741.

[9] T. Nakanishi, K. Ariga, T. Michinobu, K. Yoshida, H. Takahashi, T. Teranishi, H. Moehwald, D. G. Kurth, *Small* **2007**, *3*, 2019-2023.

[10] J. Shi, S. Zhang, X. Wang, C. Yang, Z. Jiang, *J. Mater. Chem. B* **2014**, *2*, 4289-4296.

[11] B. Baumgartner, M. J. Bojdys, M. M. Unterlass, *Polym. Chem.* **2014**, *5*, 3771-3776.

[12] C. Zhou, J. Han, R. Guo, *Macromolecules* **2008**, *41*, 6473-6479.

[13] Y. Xiao, M. Zhang, F.-X. Wang, G.-B. Pan, *CrystEngComm* **2012**, *14*, 1933-1935.

[14] H. Zhao, X. Guo, S. He, X. Zeng, X. Zhou, C. Zhang, J. Hu, X. Wu, Z. Xing, L. Chu, *Nat. Commun.* **2014**, *5*, 3108.

[15] K. Zhang, A. Geissler, X. Chen, S. Rosenfeldt, Y. Yang, S. Förster, F. Müller-Plathe, *ACS Macro Letters* **2015**, *4*, 214-219.

[16] Y. Wang, J. Tian, X. Deng, L. Chen, S. Rosenfeldt, S. Förster, P. Vana, K. Zhang, *Adv. Mater. Interfaces* **2016**, *3*, 1600636.

[17] Y. Wang, C. Zhang, J. Tian, Y. Xie, K. Zhang, *Macromol. Chem. Phys.* **2018**, *219*, 1800229.

[18] O. Gliko, N. Neumaier, W. Pan, I. Haase, M. Fischer, A. Bacher, S. Weinkauf, P. G. Vekilov, *J. Am. Chem. Soc.* **2005**, *127*, 3433-3438.

[19] a) P. R. ten Wolde, D. Frenkel, *Science* **1997**, *277*, 1975-1978; b) J. F. Lutsko, G. Nicolis, *Phys. Rev. Lett.* **2006**, *96*, 046102; c) D. Erdemir, A. Y. Lee, A. S. Myerson, *Acc. Chem. Res.* **2009**, *42*, 621-629; d) P. G. Vekilov, *Nanoscale* **2010**, *2*, 2346-2357.

[20] As the macroscopic liquid-liquid phase separation is undetectable in our experiments, this phase diagram is only drawn for the guidance of liquid-liquid phase separation at early stages.

[21] a) G. S. Grest, K. Kremer, *Phys. Rev. A* **1986**, *33*, 3628; b) T. Yamamoto, in *Interphases and Mesophases in Polymer Crystallization III*, Springer, **2005**, pp. 37-85.

[22] a) E. Ten Grotenhuis, G. Van Aken, K. Van Malssen, H. Schenk, *J. Am. Oil Chem.' Soc.* **1999**, *76*, 1031-1039; b) C. Lopez, P. Lesieur, C. Bourgaux, M. Ollivon, *J. Dairy Sci.* **2005**, *88*, 511-526; c) J. Tomaszewska-Gras, *J. Therm. Anal. Calorim.* **2013**, *113*, 199-208.

[23] T. Yamamoto, K. Nozaki, T. Hara, *J. Chem. Phys.* **1990**, *92*, 631-641.

Graphical Abstract

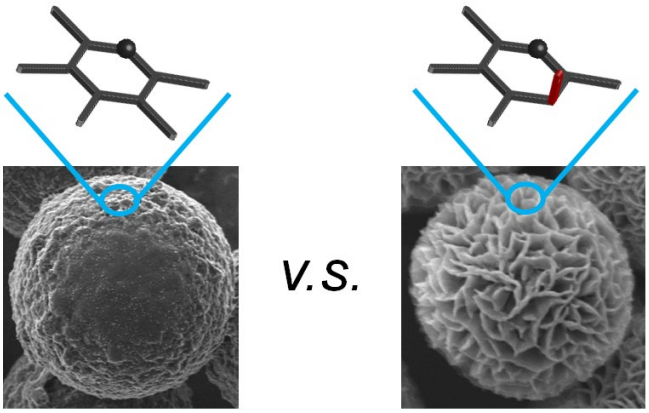

Configuration discrepancy of one single bond on sugar rings dictates the surface morphology of self-assembled semicrystalline solid or flower-like microparticles

Supporting Information

Single Bond Bending on Monosaccharide Rings enables Flower-Like Particles via Liquid-Liquid Phase Separation

Yawen Yao, [a]# Qiyun Tang, [b]# Sabine Rosenfeldt, [c] Kai Zhang[a]*

EXPERIMENTAL

Materials. D-glucose was purchased from VWR International BVBA (Leuven, Belgium). D-xylose, D-galactose and D-mannose were obtained from AppliChem GmbH (Darmstadt, Germany). Stearoyl chloride (90%) was purchased from Sigma-Aldrich (Steinheim, Germany). Pyridine (99%) was got from abcr GmbH (Karlsruhe, Germany). Chloroform (99.5%), acetone and ethyl acetate were obtained from Th. Geyer (Hamburg, Germany). All the chemicals were used as received without further purification.

Synthesis of D-monosaccharide stearoyl esters (D-MSSEs). The synthesis of D-MSSEs were carried out as reported before[1]. To set D-glucose as the example, 1 g of D-glucose was dispersed in 30 mL of pyridine and the mixture was heated to 100°C. Then, 21.00 mL of stearoyl chloride was added into the mixture, while the system was purged with nitrogen gas. After stirring at 100°C for 1 h, the reaction mixture was immediately poured into 300 mL acetone. After that, the mixture was kept in the fridge at 4°C for at least 6 h. The precipitate was separated by centrifugation at 4°C and purified through multiple washing by dissolution in chloroform and precipitation in acetone at 4°C. Finally, D-glucose stearoyl ester (D-GlcSE) was obtained after drying under vacuum condition at 25°C. The synthesis of D-galactose stearoyl ester (D-GalSE) and D-mannose stearoyl ester (D-ManSE) were exactly the same as fabricating D-GlcSE, while the amount of stearoyl chloride used for making D-xylose stearoyl ester (D-XylSE) was 20.15 ml.

Self-assembly process of D-monosaccharide stearoyl esters (D-MSSEs) in ethyl acetate. First, all four D-MSSEs were dissolved into ethyl acetate at 80°C with the concentration of 10

mg/mL. Then, the temperature was decreased to 10°C. After keeping at 10°C for 2h, a drop of each solution was pipetted onto Si-wafer and the system was immediately placed under ambient condition. To study the effect of concentration, various solutions of 1, 5 and 10 mg/mL were used. Besides, other temperatures have also been investigated. After the complete evaporation of the solvent, the samples were analyzed on scanning electron microscopy (SEM). In addition, corresponding solutions with a concentration of 10 mg/mL within these four types of solvents were dried in a vial under ambient condition for differential scanning calorimetry (DSC), thermogravimetric analysis (TGA) and small angle X-ray scattering (SAXS) characterization.

CHARACTERIZATION

Nuclear magnetic resonance (NMR) was recorded at room temperature on a Bruker DRX 500 spectrometer (Bruker, Biospin GmbH, Ettlingen) using chloroform-d as the solvent.

Fourier transform infrared spectroscopy (FTIR) was conducted on an Alpha FTIR Spectrometer (Bruker) at room temperature between 4000 and 600 cm^{-1} with a resolution of 4 cm^{-1}. The samples were measured twice with 32 scans and an average spectrum was then generated for each sample.

Scanning electron microscopy (SEM) images of the particles were obtained on a LEO Supra-35 high-resolution field emission scanning electron microscope (Carl Zeiss AG, Germany). Before SEM measurement, the sample surface was coated with a 10 nm layer of carbon. Samples were measured under ambient conditions with the electron voltage of 5 kV.

Dynamic Light Scattering (DLS). For the size and size distribution measurement of particles, the dynamic light scattering analysis was implemented on a Zetasizer Nano ZS instrument (Malvern Ltd, UK). The thoroughly cleaned quartz cuvette (Starna, Pfungstadt, Germany) filled with 1 mL of particle dispersions was used for the measurement. Each sample was processed from 60°C to 10°C and scanned three times at every 5°C, then the average values were taken as the final result.

Differential scanning calorimetry (DSC) measurements of 8~10 mg sample were recorded on a NETZSCH/DSC/200/F3/Maia (NETZSCH, Germany) between 20°C and 100°C with a heating

rate of 10 K/min. Dried N_2 gas was purged with a constant flow rate (20 mL/min) during the measurement.

Thermogravimetric analysis (TGA) was carried out on a NETZSCH TG/209/F1/Iris (NETZSCH, Germany) between 100°C and 600°C with a heating rate of 10 K/min under constant nitrogen flow of 20 mL/min.

Small angle X-ray scattering (SAXS) was performed using the small-angle X-ray system "Double Ganesha AIR" (SAXSLAB, Denmark). The X-ray source is a rotating anode (copper, MicoMax 007HF, Rigaku Corporation, Japan) providing a micro-focused beam. The data were recorded by a position sensitive detector (PILATUS 300K, Dectris). To cover the range of scattering vectors q between 0.004-2.0 $Å^{-1}$ different detector positions were used. The scattering vectors q is given by

$$q = |\vec{q}| = \frac{4\pi}{\lambda} \sin\left(\frac{\theta}{2}\right) \quad (1),$$

where $\boldsymbol{\lambda}$ is the wavelength and $\boldsymbol{\theta}$ is the scattering angle. The circularly averaged data were normalized to incident beam, sample thickness and measurement time before the subtraction of the background (solvent).

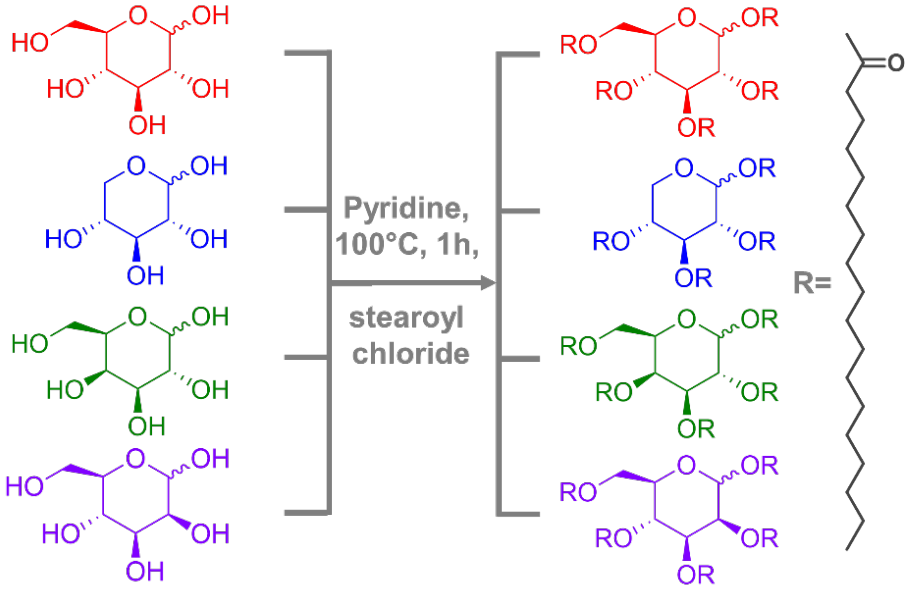

Figure S1. Schematic illustration of the synthesis of D-monosaccharide stearoyl esters: D-glucose stearoyl ester (D-GlcSE, red), D-xylose stearoyl ester (D-XylSE, blue), D-galactose stearoyl ester (D-GalSE, green) and D-mannose stearoyl ester (D-ManSE, purple). R represents C18 aliphatic chains.

The synthesis of D-MSSEs was achieved by using stearoyl chloride (**Figure S1**) and all the hydroxyl groups of monosaccharides were successfully esterified by stearoyl groups as confirmed by NMR analysis (**Figure S2** and **S3**).

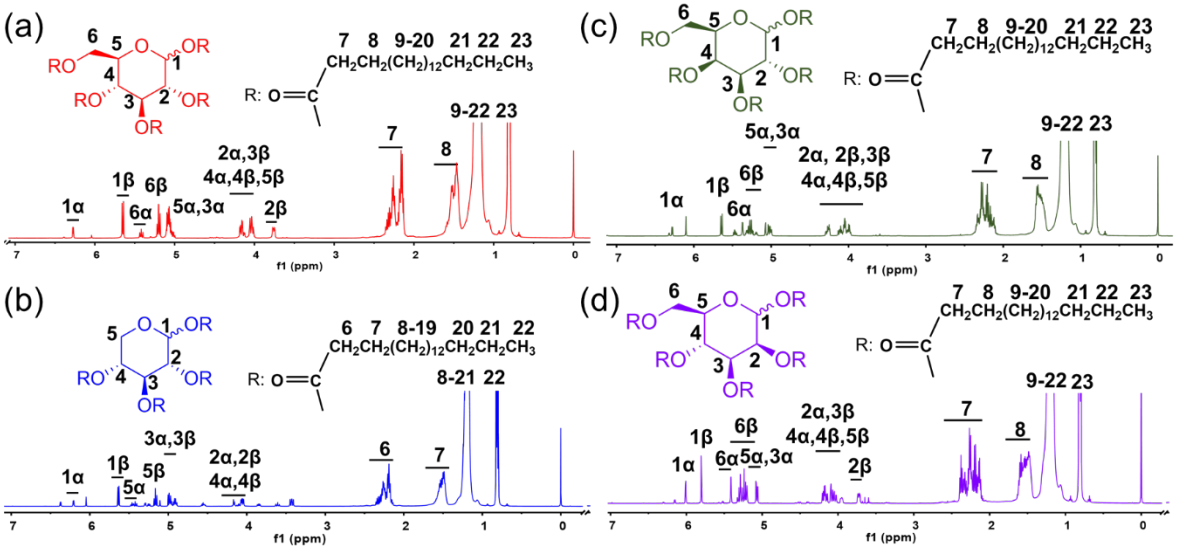

Figure S2. ^{1}H NMR spectra of a) D-glucose stearoyl ester (D-GlcSE); b) D-xylose stearoyl ester (D-XylSE); c) D-galactose stearoyl ester (D-GalSE) and d) D-mannose stearoyl ester (D-ManSE) recorded in deuterated chloroform.

In ^{1}H NMR spectra of the 4 D-MSSEs (D-GlcSE, D-XylSE, D-GalSE and D-ManSE), the signals between 0-3 ppm represent hydrogens in aliphatic ester groups. The peaks between 3-7 ppm can be classified to corresponding hydrogens in the sugar rings of the 4 D-MSSEs[2]. The specific signals were assigned as shown in **Figure S2**. After the integration of the peaks in ^{1}H NMR spectra, the α/β ratio of the 4 D-MSSEs can be calculated. The α/β ratio of the 4 D-MSSEs

are 20/80 of D-GlcSE; 15/85 of D-XylSE; 27/73 of D-GalSE and 35/65 of D-ManSE. Similar α/β ratio illustrates that the main discrepancy between D-GlcSE and D-XylSE is the number of side chains, whereas the configuration of bonds at C2 and C4 is the main difference among D-GlcSE, D-XylSE and D-ManSE.

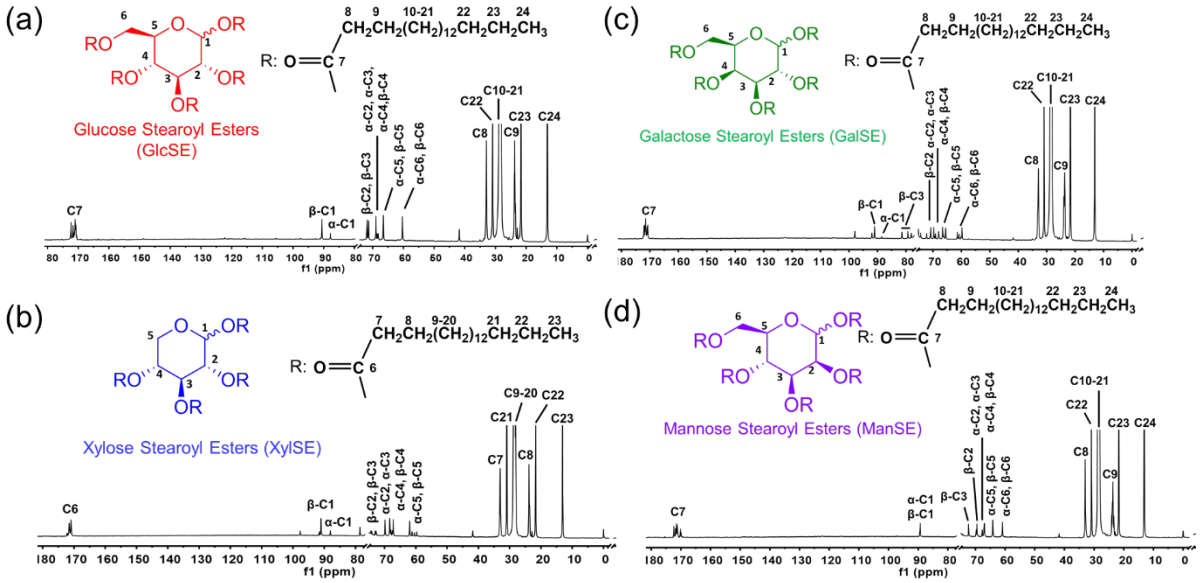

Figure S3. ^{13}C NMR spectra of a) D-glucose stearoyl ester (D-GlcSE); b) D-xylose stearoyl ester (D-XylSE); c) D-galactose stearoyl ester (D-GalSE) and d) D-mannose stearoyl ester (D-ManSE) recorded in deuterated chloroform.

In the ^{13}C NMR spectra of all the D-MSSEs (D-GlcSE, D-XylSE, D-GalSE and D-ManSE), the resonance signals for carbon atoms of methyl groups at 17 ppm and of methylene at 22 and 35 ppm were observed. Moreover, the presence of the resonance signals for carbon from methylene units at 62 ppm and the carbon of -C=O at 173 ppm confirmed the formation of ester linkages during preparation process[3]. The signals between 10 and 60 ppm were ascribed to the carbons of aliphatic chains, while the carbons of monosaccharides gave signals between 60 and 110 ppm[4]. The single peaks could be assorted as shown within the ^{13}C NMR spectra.

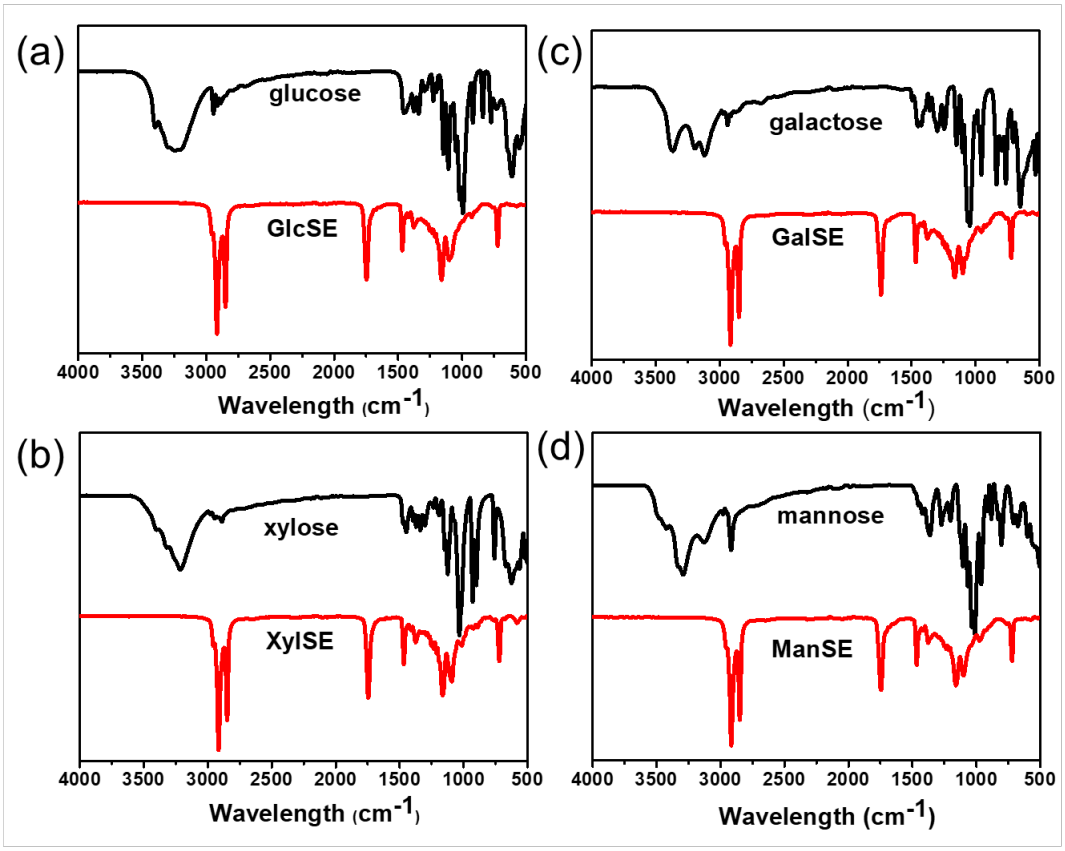

Figure S4. FTIR spectra of a) D-glucose stearoyl ester (D-GlcSE); b) D-xylose stearoyl ester (D-XylSE); c) D-galactose stearoyl ester (D-GalSE) and d) D-mannose stearoyl ester (D-ManSE).

FTIR spectra indicated characteristic peaks of D-MSSEs and pointed out the new bands attributed to the vibrations of stearoyl groups. In the spectra of D-glucose, D-xylose, D-galactose, D-mannose, they showed similar spectra, which represent the similar molecular structure. The peaks near 3305 cm^{-1} represented hydroxyl groups. These typical peaks were disappeared in the spectra of D-GlcSE, D-XylSE, D-GalSE and D-ManSE. At the same time, new signals came into being at peaks of 2850 and 2917 cm^{-1}, which were ascribed to the symmetric stretching vibrations of methylene and asymmetric groups, respectively[5]. Apart from that, other new bands were also being generated through the process of esterification. As shown in the spectra of D-GlcSE, D-XylSE, D-GalSE and D-ManSE, peaks at 1747 cm^{-1} were attributed to the stretching

vibrations of C=O groups[6]. Peaks at 1467 cm^{-1} were obtained from the deformation vibrations of C–H groups of long aliphatic chains[7]. Moreover, new bands at 1159 and 721 cm^{-1} were ascribed to stretching and rocking vibrations of C-C groups of long aliphatic chains, respectively[8]. In addition, a few signals derived from the D-glucose, D-xylose, D-galactose, D-mannose backbone disappeared during the esterification, e.g. the signals around 2894 and 1030 cm^{-1}.

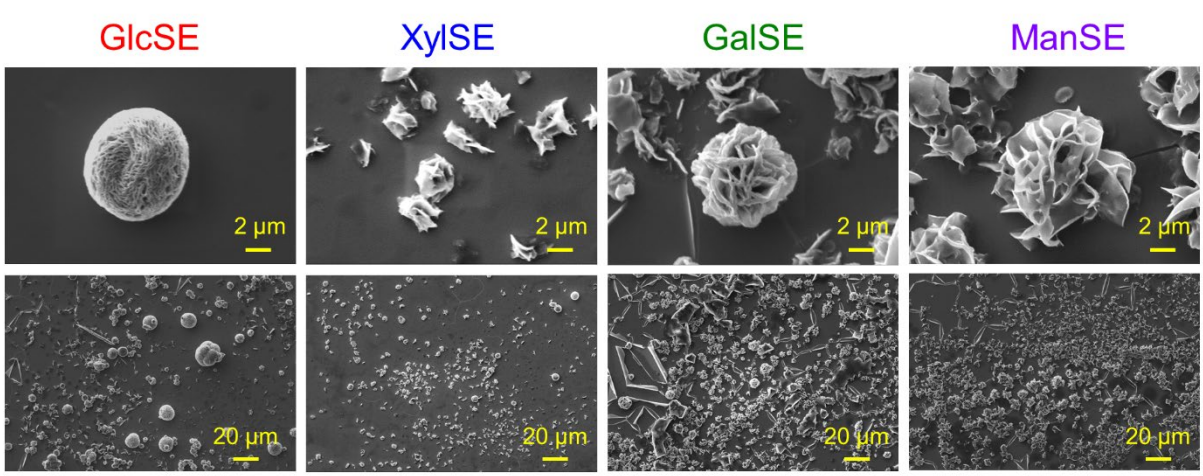

Figure S5. SEM images of aggregates from D-MSSEs prepared with the concentration of 1 mg/mL under different magnifications.

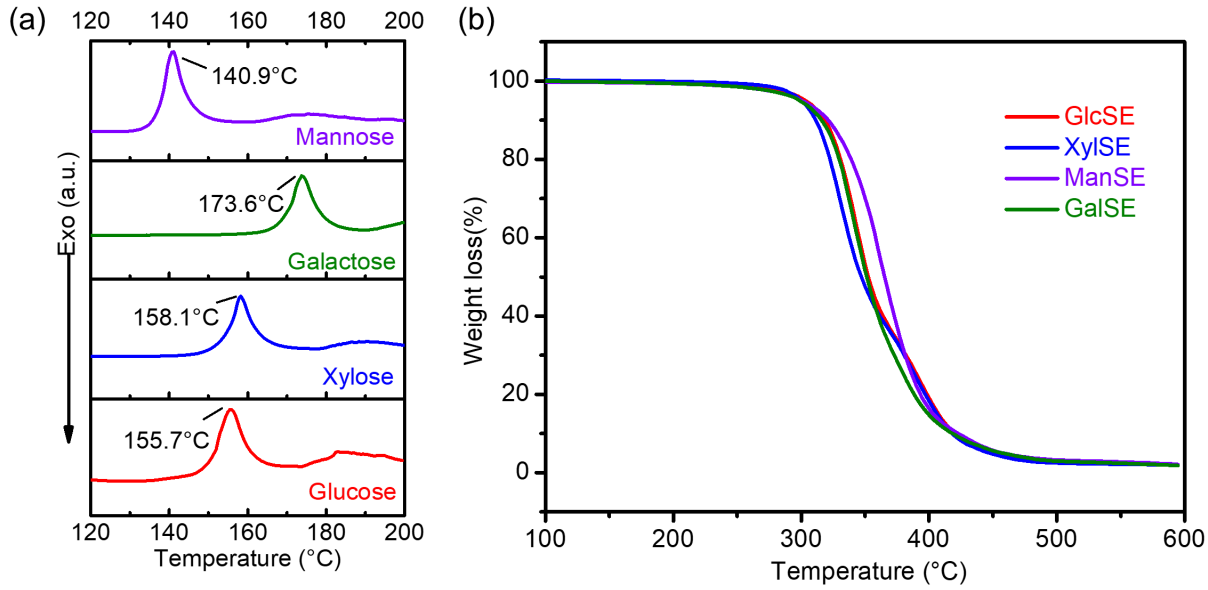

Figure S6. a) DSC heating curves of monosaccharides and b) TG curves of D-glucose stearoyl ester (D-GlcSE, red), D-xylose stearoyl ester (D-XylSE, blue), D-galactose stearoyl ester (D-GalSE, green) and D-mannose stearoyl ester (D-ManSE, purple) between 100-600°C.

Due to the existed hydrogen bonds, monosaccharides have higher melting temperature than their stearoyl esters. The mass loss curves (TG) for D-MSSEs analyzed in inert atmosphere were presented in **Figure S6b**. In order to determine the thermal stability of the D-MSSEs, we performed thermogravimetric analysis in nitrogen atmosphere and dynamic conditions with 10 °C/min heating rate, at temperature ranging between 20°C and 500°C. The curves from the 4 D-MSSEs showed similar one main step between about 250°C and 500°C. This step was mainly attributed to the total degradation of D-MSSEs. The analyzed D-MSSEs have relatively good thermal stabilities. Up to 300°C, the D-MSSEs lost non-significant weight (less than 9%). Only when heating up to 350°C, the D-MSSEs lost more than half of its mass (around 57%) and in the heating range of 350-400°C, D-MSSEs lost most of the mass (55%-85%). At 600°C, D-MSSEs lost nearly all of their weight.

SIMULATION PART

Model and simulation details.

Here we used Monte Carlo simulations based on a coarse-grained model of D-MSSE molecules to describe the crystallization behaviors of D-GlcSE, D-XylSE, and D-GalSE (D-ManSE) connected by stearoyl chains from solutions. In experiments, each stearoyl chain is comprised of 18 C atoms. In our simulation, we group 3 -[CH_2]- groups into one monomer. Therefore, there are 6 monomers within one coarse-grained chain. The sugar ring is modeled as one core monomer, and the ring feature constrains its neighboring bonds in one plane, which can be captured by the dihedral potentials between these bonds. We ignore the difference between the molecular weight and the volume of the 3 -[CH_2]- repeat groups and the sugar ring molecules. The coarse-grained D-GlcSE is constructed by 1 core monomer connected to 5 side chains, where each side chain includes 6 monomers. Then, the total monomer number is $1 + 5 \times 6 = 31$. Similarly, the total monomer number of D-GalSE (D-ManSE) is also $1 + 5 \times 6 = 31$, and that for XylSE is $1 + 4 \times 6 = 25$ because of one less binding site.

The bonded interactions between the neighboring monomers along chain contours for the 4-arm star of D-XylSE and 5-arm star of D-GlcSE and D-GalSE (D-ManSE) are modelled by a FENE potential[9]

$$U_b(r) = \begin{cases} -\frac{1}{2} k l_{max}^2 \ln\left[1 - \frac{r^2}{l_{max}^2}\right], & r \le l_{max} \\ \infty, & r > l_{max} \end{cases} \quad (2),$$

where $l_{max} = 1.5\sigma$ and $k = 30.0\varepsilon/\sigma^2$ are chosen to prevent the chain crossings.

The non-bonded interactions between all monomers are treated via a truncated and shifted Lennard-Jones potential:

$$U_{LJ}^{ts}(r) = \begin{cases} 4\varepsilon\left[(\frac{\sigma}{r})^{12} - \left(\frac{\sigma}{r}\right)^6 - E_{cut}\right], & r \le r_{cut} \\ 0, & r > r_{cut} \end{cases} \quad (3),$$

here are the L-J units and $E_{cut} = (\sigma/r_{cut})^{12} - (\sigma/r_{cut})^6$. We choose $r_{cut} = 4.5\sigma$ and $k_B T$ varying between 0.8ε to 1.4ε during the simulation.

To model the crystallization of stearoyl chains, an angle bending potential is introduced[11]

$$U_\theta = a - b(\cos\theta - \cos\theta_0) + c(\cos\theta - \cos\theta_0)^3$$

Here, θ is the angle between the nearest neighbouring bonds among 3 consecutive monomers. θ_0 is selected as 108.78°. The coefficients are chosen as $a = 3.00k_BT$, $\mathrm{b} = 9.27k_BT$, and $\mathrm{c} = 29.79k_BT$, which have proven to be successful in modelling the crystallization behaviors of polyethylene chains[10]. Therefore, this model should be suitable for modelling the crystalline properties of the D-MSSE molecules modified by the aliphatic side chains in our experiments, which possess the same repeating -[CH_2]- units as that of polyethylene chains.

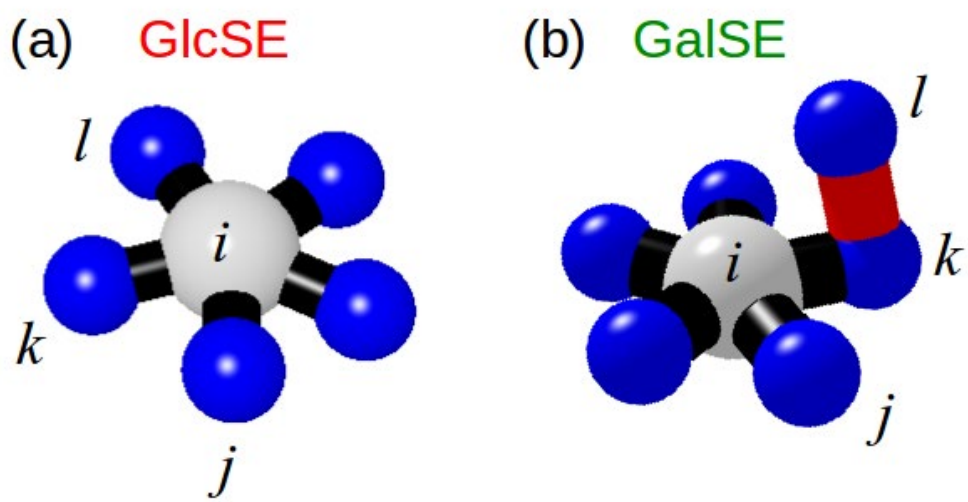

Figure S7. Illustration of bonds (black cylinder) connecting to the core monomer representing sugar rings (gray sphere) from end-monomer of side chains (blue sphere) for (a) D-GlcSE and (b) D-GalSE. The core monomer i and side chain monomers j, k, l in (a) construct the improper dihedral potential, enforcing the co-plane behavior among the bonds connecting to the sugar rings. For D-GalSE in (b), one bond connecting to the core monomer is bending axially to the sugar ring plane, see the red bond between monomers k and l.

To reflect the planar feature of the sugar ring, we introduce the improper dihedral potentials between the bonds connected to the core monomer, see **Figure S7**. Here the vector $\vec{m} =$

$\overrightarrow{r_{ij}} \times \overrightarrow{r_{jk}}$ is the normal vector going through the plane constructed by monomer i, j, and k. Similarly, the $\vec{n} = \overrightarrow{r_{lk}} \times \overrightarrow{r_{jk}}$ is the normal vector going through the plane constructed by monomer j, k, and l. The dihedral angle ϕ_{ijkl} can be obtained

$$\cos \phi_{ijkl} = \frac{\vec{m} \cdot \vec{n}}{|m||n|}$$

The dihedral potential is chosen as a harmonic form

$$U_{ijkl} = k_1 \phi_{ijkl}^2$$

which forces the angle to the minimum of $\phi_{ijkl} = 0$. The coefficient is chosen as $k_1 = 20.0 k_B T$ and the dihedral potentials are calculated by going through all the arm bonds consecutively to constrain these bonds (4 bonds for D-XylSE and 5 bonds for D-GlcSE, D-GalSE, and D-ManSE) in one plane.

The difference between D-GlcSE and D-GalSE (D-ManSE) is that one bond connecting the sugar rings and the side chains is bending axially to the sugar ring plane, see **Figure 1a** in the main text. To reflect this feature, we add another potential between the normal vector $\vec{m} = \overrightarrow{r_{ij}} \times \overrightarrow{r_{jk}}$ on the plane constructed by monomer i, j, and k, and the bond vector $\overrightarrow{r_{kl}}$ between the monomer k and l, see **Figure S6b**. The angle ϕ_2 between the vectors $\vec{m}$ and $\overrightarrow{r_{kl}}$ can be obtained

$$\cos \phi_2 = \frac{\vec{m} \cdot \overrightarrow{r_{kl}}}{|m||r_{kl}|}$$

The potential is also of a harmonic form

$$U_2 = k_2 \phi_2^2$$

with the coefficient of $k_2 = 20.0 k_B T$ to force the vector $\overrightarrow{r_{kl}}$ perpendicular to the sugar ring plane (at the minimum of $\phi_2 = 0$). The potentials U_{ijkl} and U_2 ensure the configurational features of the bonds connecting to the monosaccharide rings from the side chains.

In this simulation model, the length unit is σ, which corresponds to the size of coarse-grained monomers. Here we group 3 -[CH_2]- repeat units into one coarse-grained monomer in our simulation. The size of this monomer is approximate 1 nm, therefore we choose $\sigma = 1nm$ for all the discussions in the main text and the subsequent paragraphs. We also use the reduced temperature $k_B T/\varepsilon$ in the discussions and relabel the reduced temperature by T.

Additional results.

We choose the system size of $30 \times 30 \times 30\ nm^3$ with the monomer density of $0.60nm^{-3}$. We first equilibrate the system at a high temperature of $T = 4.0$, and then quench the system to $T = 0.8$. Subsequently we investigate the crystalline behavior of 3 different D-MSSE molecules under the same conditions. Here the crystallinity of D-MSSE molecules is defined as the ratio between the number of crystalline monomers and total monomers. The crystalline monomers represent the monomers on the crystalline bonds, which are defined as the number of neighboring parallel bonds no less than 3. In the off-lattice model, the neighboring parallel bonds represents the bonds where the distance between their center of mass is shorter than $1.2\ \sigma$ and $\cos\theta > 0.97$, here θ represents the angle between the two bond vectors. Similarly, the crystallinity of core monomer for sugar rings is defined as the ratio between the number of crystalline core monomers and total core monomers in the system.

The time evolution of the crystallinity for the 3 D-MSSE molecules and the core monomers at $T = 0.8$ is shown in **Figure S8**. One can see that the crystallinity increases as time proceeds, and approaches a plateau value after $\mathrm{t} > 300000\ MC\ Steps$. It is clearly to see that crystallinity of the 4-arm D-XylSE is larger than that of the 5-arm D-GlcSE and D-GalSE, whereas the crystallinities of D-GlcSE and D-GalSE are nearly the same as time evolves. We calculate the average crystallinity between $\mathrm{t} = 930000\ \mathrm{MC\ steps}$ and $1130000\ \mathrm{MC\ steps}$, where the crystallinity fluctuates around a stable value, see the magenta box in **Figure S8**. The average crystallinities are shown in the **Figure 4b** in the main text.

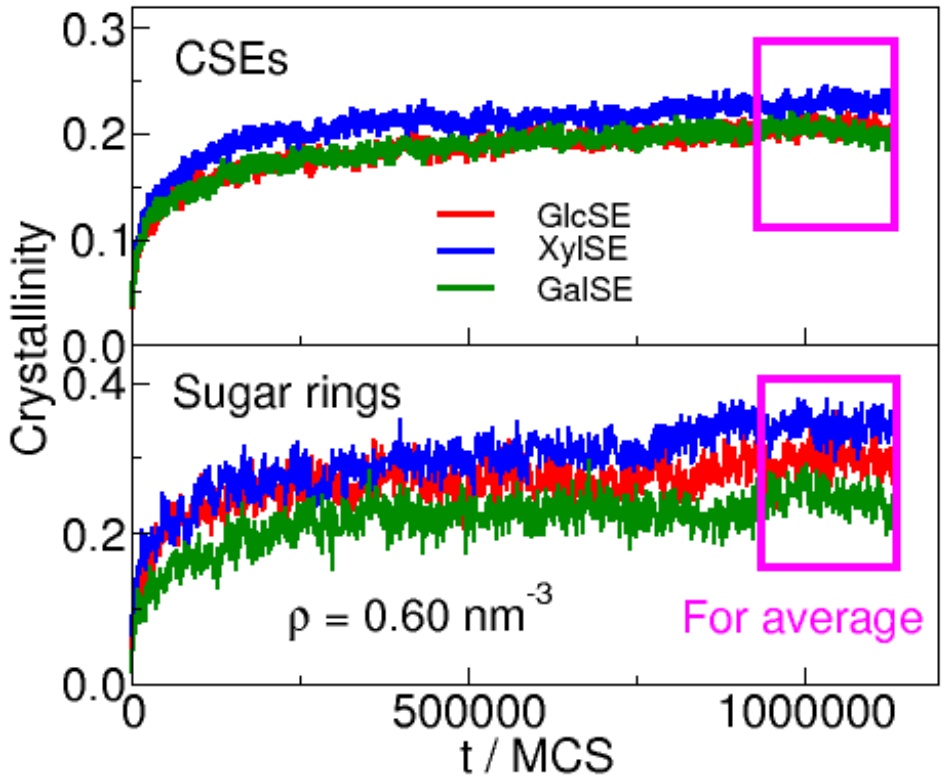

Figure S8. Time evolution of the crystallinity of 3 D-MSSE molecules and the core monomers for sugar rings. The monomer density is 0.6 nm^{-3} and the reduced temperature is $T = 0.8$. The magenta box shows the region to calculate the average crystallinity shown in main text.

We also calculate the average crystallinities of different D-MSSE molecules at a higher density of $0.70nm^{-3}$, and the results are shown in **Figure S9**. The behavior is similar to that on $0.60nm^{-3}$ in the main text. The crystallinity at other temperatures are also explored, and the average crystallinity drops toward 0.1 at $T = 1.2$, and smaller values at higher temperatures. The lower temperature, $T = 0.5$, gives slightly higher average crystallinities, but the relaxation becomes much slower.

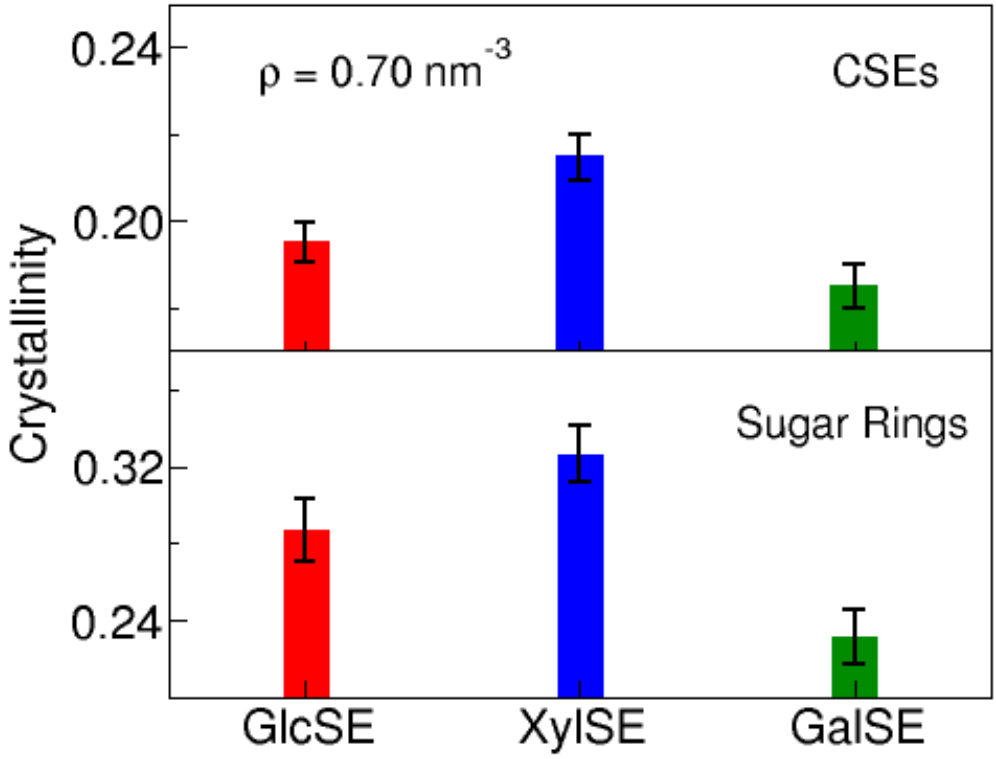

Figure S9. The average crystallinity of 3 different D-MSSE molecules and that of sugar-rings at the density of $0.70nm^{-3}$.

Reference

[1] C. Vaca Garcia, G. Gozzelino, W. Glasser, M. E. Borredon, *J. Polym. Sci. B: Polym. Phys.* **2003**, *41*, 281-288.

[2] K. Zhang, A. Geissler, M. Standhardt, S. Mehlhase, M. Gallei, L. Chen, C. M. Thiele, *Scientific reports* **2015**, *5*, 11011.

[3] T. Heinze, T. F. Liebert, K. S. Pfeiffer, M. A. Hussain, *Cellulose* **2003**, *10*, 283-296.

[4] T. Liebert, J. Wotschadlo, P. Laudeley, T. Heinze, *Biomacromolecules* **2011**, *12*, 3107-3113.

[5] P. Jandura, B. V. Kokta, B. Riedl, *J. Appl. Polym. Sci.* **2000**, *78*, 1354-1365.

[6] C. Freire, A. Silvestre, C. P. Neto, R. Rocha, *Cellulose* **2005**, *12*, 449-458.

[7] Y. Guo, X. Wang, D. Li, H. Du, X. Wang, R. Sun, *Polym. Bull. (Berlin)* **2012**, *69*, 389-403.

[8] aL. Crépy, V. Miri, N. Joly, P. Martin, J.-M. Lefebvre, *Carbohydr. Polym.* **2011**, *83*, 1812-1820; bU. Ratanakamnuan, D. Atong, D. Aht-Ong, *Carbohydr. Polym.* **2012**, *87*, 84-94.

[9] G. S. Grest, K. Kremer, *Phys. Rev. A* **1986**, *33*, 3628.

[10] T. Yamamoto, in *Interphases and Mesophases in Polymer Crystallization III*, Springer, **2005**, pp. 37-85.